論文 / 著書情報
Article / Book Information

題目(和文)	生分解性金属インプラント用Mg-Zn合金の組織制御と表面改質
Title(English)	Microstructure Control and Surface Modification of Mg-Zn Alloys for Biodegradable Metallic Implant Materials
著者(和文)	DINH NGOC PHAM
Author(English)	Dinh Ngoc Pham
出典(和文)	学位:博士（工学）, 学位授与機関:東京工業大学, 報告番号:甲第12098号, 授与年月日:2021年9月24日, 学位の種別:課程博士, 審査員:小林 郁夫,多田 英司,史 蹟,曽根 正人,生駒 俊之
Citation(English)	Degree:Doctor (Engineering), Conferring organization: Tokyo Institute of Technology, Report number:甲第12098号, Conferred date:2021/9/24, Degree Type:Course doctor, Examiner:,,,,
学位種別(和文)	博士論文
Type(English)	Doctoral Thesis

DOCTORAL THESIS

Microstructure Control and Surface Modification of Mg-Zn Alloys for Biodegradable Metallic Implant Materials

PHAM NGOC DINH

Department of Materials Science and Engineering

Tokyo Institute of Technology

2021

Table of Contents

Chapter 1

General introduction

1.1 Metallic biomaterials for orthopedic implants

Metallic biomaterials have been used extensively for orthopedic implants, such as joint replacements and bone fixation plates and screws, owing to their excellent mechanical strength and fracture toughness compared to ceramics and polymeric materials [1–3]. The other advantages of metallic materials are their simple production and processing by using well established technologies like casting, forging, extrusion, rolling, machining and others.

Up to date, the most commonly used metallic biomaterials include stainless steels, cobalt-based alloys and titanium-based alloys. These materials have been optimized for this application and can provide the mechanical support under loading during the whole healing time. However, a limitation of these current metallic biomaterials is possible release of toxic metallic ions and/or particles through corrosion or wear processes that lead to inflammatory cascades which reduce biocompatibility and cause necrosis of soft-tissue around the implant [3]. In addition, the elastic modulus of these materials is significantly higher than that of human bones. A large gap between the elastic moduli of the orthopedic implant and the bone tissue potentially induce the stress-shielding effect which cause to reduced stimulation of new bone growth and bone density. Stress-shielding refers to the reduction in bone density caused by an implant bearing part of the stress load, subjecting bone to reduced stress [4]. Under normal conditions healthy bone remodels in response to its bearing load [4]. Current metallic biomaterials are generally considered as corrosion resistant *in vivo*, so they are very suitable for devices with long or permanent service such as hip and knee joint replacements. However, for temporary implants such as plates, screw and pins used to secure serious bone fracture, this means the devices must be removed by a secondary surgery after the broken bones or wounded parts have sufficiently healed, thereby increasing financial cost, recovery time and health of the patient [5].

In order to avoid the follow-up surgery to remove the implant and reduce the burden of the patient, a new class of biodegradable metallic materials has been introduced. The biodegradable metallic materials are expected to corrode gradually *in vivo*, with an appropriate host response generated by the corrosion products being released, followed by a complete dissolution after fulfilling the mission to support the tissue healing [6]. Therefore, the main component of biodegradable metallic materials should be essential metallic elements that can be absorbed by the human body, and exhibit an appropriate degradation rates and modes in the physiological environment [6].

1.2 Magnesium as biodegradable orthopedic implant materials

Mg is a chemically active metallic element that can degrade naturally in the physiological environments by corrosion and a potential candidate for biodegradable orthopedic implant materials. Mg is the lightest structural metal with a density of 1.74 g/cm3, which is about two thirds and one third the density of aluminum (Al, 2.7 g/cm3) and titanium (Ti, 4.7 g/cm3), respectively [3]. Mg alloys show the highest specific strength of structural alloys. The strength and fracture toughness of Mg is larger than those of ceramic and polymeric biomaterials such as hydroxyapatite (HAp), poly-L-lactic acid (PLLA) etc., while the elastic modulus and yield strength of Mg are closer to those of the human bones than is the case for other commonly used metallic implants as shown in Table 1.1 [3]. Moreover, Mg is an essential to human metabolism with daily intake in the range of 250–500 mg day–1 and is naturally found in bone tissues. Higher Mg intakes have shown a positive effect to bone mineral density in elderly men and women [3].

Mg has been widely studied as biomedical devices that disrupted the paradigm in biomaterials science to develop only highly corrosion resistant metals since the late 19th century and early 20th century [7]. Although these investigations revealed obvious advantages of Mg alloys, they were abandoned at that time due to their considered undesirable degradation in addition to the development of inert stainless steel. As Mg alloy technology advanced, both the mechanical and corrosion properties have been improved and the idea of temporary implant materials is, thus, rediscovered. Therefore, several key issues for biodegradable Mg alloys have been widely investigated over the last decade, including the selection of alloying elements, adjustment of microstructural and mechanical properties, biodegradation mechanisms and their influencing factors, control of degradation rates and ion release; and in vitro and in vivo biocompatibility.

Although Mg and its alloys have been investigated as implant materials for more than a century, not so many commercial implants made of Mg and its alloys are available. The first commercial Mg-based orthopedic implant has emerged since 2010s. The MAGNEZIX® compressive screw (CS) obtained CE marking for medical devices used in medical applications in Europe in 2013, as shown in Figure 1.1 [8]. The MAGNEZIX® CS was developed by Syntellix AG (Hannover, Germany) and is made from Mg-Y-RE-Zr-based alloys (commercially known as WE43 alloy) containing more than 90% Mg fabricated by powder metallurgy technique. MAGNEZIX ® CS is clinically used in a wide range of the regions of the body including metacarpals, clavicular, phalanges, distal femur and humerus fractures, and to date, there have been about 3,000 operations world-wide performed with the MAGNEZIX® CS 3.2 screw. BIOTRONIK (Berlin, Germany) developed the absorbable metal stents (AMS) made of 92.5% Mg and 7.5% Rare-earths based alloys as shown in Figure 1.2 [9]. The clinical surgery of BIOTRONIK AMS in human body were investigated from 2013 to 2015 by 123 patients with 123 coronary target lesions for treatment of obstructive coronary disease. The implantation showed feasibility with favorable safety and performance1 outcomes at 12 months. Consequently, the BIOTRONIK AMS achieved CE marking in 2016.

1.3 Corrosion of magnesium and its alloys

The relatively poor corrosion resistance of Mg and its alloys are mainly attributed to two key factors including: (i) the highly electronegative potential of Mg which allows corrosion to proceed even in the absence of oxygen, and (ii) the poorly corrosion protectiveness of oxide and/or hydroxide surface films formed upon Mg [10–12].

The dissolution of Mg in an aqueous environment usually proceed by an electrochemical reaction with water to produce magnesium hydroxide and hydrogen gas. A schematic illustration of Mg degradation is shown in Figure 1.3 [10]. Immediately after exposure to the environment, the anodic dissolution of Mg occurred as is shown in the equation (1.1). Simultaneously, the reduction of protons occurs at the cathode as is shown in the equation (1.2) [10]. At the corrosion potential, the overall reaction can be expressed as shown in the equation (1.3) [10].

Anodic reaction: $$Mg \rightarrow Mg^{2+} + 2e^{-} \quad (1.1)$$

Cathodic reaction: $$2H_2O + 2e^{-} \rightarrow 2OH^{-} + H_2 \quad (1.2)$$

Overall reaction: $Mg + 2H_2O \rightarrow Mg(OH)_2 + H_2$ (1.3)

The $Mg(OH)_2$ layers are naturally loose and cannot provide sufficient corrosion protection for Mg metal substrate. In the physiological environment with the presence of a high amount of chlorine ions (~140 mmol/L), chlorine ions easily convert the surface $Mg(OH)_2$ layers into more soluble $MgCl_2$. The dissolution of $Mg(OH)_2$ layers exposes the active Mg metal substrate, promoting further dissolution of Mg. The action is shown in the equation (1.4) [10].

$$Mg(OH)_2 + 2Cl^- \rightarrow MgCl_2 + 2OH^- \quad (1.4)$$

In the simulated body fluids (SBFs) or in the human body, it has been proven that the other corrosion product layers can contain other products such as magnesium and/or calcium phosphates and carbonates as shown in Figure 1.4 [13]. The reactions can be described as follows:

$$Mg^{2+}/Ca^{2+} + OH^- + HCO_3^- + (n-1)H_2O \rightarrow MgCO_3./CaCO_3.nH_2O \quad (1.5)$$

$$Mg^{2+}/3Ca^{2+} + 2OH^- + 2HPO_4^{2-} + (n-2)H_2O \rightarrow Mg_3(PO_4)_2./Ca_3(PO_4)_2.nH_2O \quad (1.6)$$

1.3.1 Localized corrosion

Unlike pure Mg metal, Mg alloys always suffer from nonuniform corrosion due to the existence of internal galvanic coupling or electrochemical nonuniformity. The localized corrosion is the biggest concern about corrosion of Mg alloys in practical applications because it decreases the load-bearing capability more intensely than the uniform corrosion.

Pitting corrosion is one of the most commonly observed type of localized corrosion in Mg alloys. The pit formation begins at the top of the surface and proceeds downward in the vertical direction. In the Mg alloys, the pitting corrosion does not propagate deeply but spread laterally due to the alkalization effect at the tips of corroding pits. Filiform corrosion is another common form of localized corrosion that can be observed in Mg alloys. It is caused by an active corrosion cell and usually start from a corrosion pit, then moves across the metal surface. In other metallic materials, e.g. Al alloys, steels, etc., filiform corrosion can be observed on the coated surfaces and the cathodic reaction is driven by the oxygen reduction. In the Mg alloys, the surface film covering the Mg substrate acts as a coating layer, and cathodic reaction is driven by hydrogen evolution [10,14].

1.3.2 Galvanic corrosion

Mg has a lower standard corrosion potential than most other engineering metals, therefore, Mg acts as the anode and corrodes preferentially in galvanic corrosion. The cathodes can be internal as second phases or impurity phases, it can be other metals when they are in close contact with Mg. It has been reported that the galvanic corrosion rate is increased by a number of factors including high potential difference between anode and cathode, high conductivity of medium and large area ratio of cathode to anode, etc. [10,14].

1.4 Strategies to improve corrosion resistance of Mg for orthopedic implants

The susceptibility to corrosion in physiological environments is the main limitation of Mg in biomedical implants. Hence, the control of corrosion rate is crucial for improving the biomechanical performance of biodegradable Mg/Mg-based implants. Extremely intensive research efforts have been carried out for the control of biodegradation of Mg alloys, both in exploration of novel alloys as well as for developing new types of surface modification approaches. The challenge in both strategies is to combine optimization of the corrosion behavior with the tailored and desired biological performance for the specific targeted application [3,6,15–17].

1.4.1 Alloy design

(1) Elemental alloying

Alloying is one of the most effective method to modify the microstructure and properties of Mg-based alloys. An appropriate alloying composition can improve significantly the corrosion resistance, mechanical properties, and productivity of Mg-based materials. Thus, there have been numerous efforts on developing Mg alloys for different applications. Figure 1.5 shows the summary of Mg alloy development [18] and Figure 1.6 shows the summary of mechanical strength and degradation rate of Mg-X binary alloys [6]. Although having suitable mechanical properties and moderate corrosion rate, the commercially available Mg alloys, such as AZ31, AZ91, AM60, WE43, and LAE442 alloys, were originally designed for industrial usage such as automobile and aerospace. These alloys contain low biocompatibility elements, e.g. Al, RE, etc., and are not suitable for biomedical applications [3,6,18]. Therefore, the selection of alloying elements for Mg alloys should be carefully considered when they are designed for biomedical applications.

(2) Zinc addition to Mg

Only a few numbers of elements are suitable to use in Mg alloys for biomedical applications by considering the requirements of mechanical property and biocompatibility. Song et al. investigated *in vitro* corrosion rates of several Mg alloys and reported that Ca, Mn and Zn could be appropriate candidates [19]. The *in vitro* cell biocompatibility indicated that Zn and Ca did not have cytotoxicity [20]. Additionally, the addition of Zn can help to reduce the deleterious effects of metallic impurities, i.e. Fe and Ni [21]. Therefore, Zn-containing Mg alloys have been paid more attention and developed as promising candidates for biomedical applications.

From a biological point of view, Zn is very important for biological functions and one of the most abundant nutritionally essential elements in the human body as it is involved in various aspects of cellular metabolism. Zn is important to the proper function of numerous enzymes and it supports immune functions, protein and DNA synthesis and wound healing [22]. The recommended dietary allowance (RDA) and recommended upper limit for Zn are 15 and 40 mg day^{-1}, respectively [22]. The consumption of zinc in amounts higher than these values is generally considered relatively non-toxic, and amounts approaching 100 mg day^{-1} can be tolerated for some time [22].

Figure 1.7 shows a phase diagram of Mg-Zn binary alloys [23]. It can be seen that the solid solubility of Zn in Mg is about 1.6 wt% at room temperature in the equilibrium state and thus the Zn elements tend to incorporate as solution atoms in Mg matrix of the alloys with Zn content less than 1.6 wt%. With further increasing Zn content, more Mg-Zn intermetallic compounds are formed in the structure, resulting in the grain refinement. When the content of Zn exceeds 6.2 wt% which is the solid solubility limit for Zn in Mg at 341°C, amount of the intermetallic compounds in the structure increases rapidly. For these reasons, the studies on Mg-Zn binary alloys as biodegradable materials often give attention to the content of Zn in the range from 0.5 wt% up to 7 wt% [24].

1.4.2 Solution heat treatment

Heat treatments can be effective methods to modify the grain sizes and the morphology of second phases, resulting to change the mechanical strengths and corrosion rates of magnesium alloys. It has been reported that the effect of heat treatment on the corrosion behavior of Mg alloys is different with the change in alloy composition and heat treatment

condition [25,26]. Therefore, the selection of an appropriate heat treatment for improving the mechanical properties and corrosion resistance for Mg alloys should be carefully considered.

Solution heat treatment process is a technique in which an alloy is heated to a suitable temperature and held at this temperature for a sufficient length of time to allow a desired alloying element to enter into the solid solution. This is followed by rapid quenching or cooling in a suitable liquid to obtain certain material properties. Quenching prevents components that normally form the secondary phase through low temperature processing from occurring by trapping the secondary phase within the parent lattice which produces a supersaturated solid solution single phase [27,28].

Song et al. studied the effect of the T4 (solution) and T6 (aging) treatments on the corrosion behavior of commercial AZ91D alloy. They reported that T4 treatment decreased the barrier effect in AZ91D alloy due to the dissolution of β phase while the T6 treatment increased the barrier effect because the amounts of β phase was increased [29,30]. On the contrary, Liu et al. stated that T4 treatment enhanced the corrosion resistance of Mg-3wt% Zn alloy by decreasing the amounts of MgZn particles while T6 treatment decreased the corrosion resistance of Mg-3wt% Zn alloy [31]. Lin et al. reported that T4 treatment could improve the anticorrosion behavior and increase the in vitro cell viability of ZAX1330 (Mg-Zn-Al-Ca) alloy [32]. Hort et al. applied T4 and T6 treatments to the Mg-Gd-based alloys developed in their study. It was found that most of the eutectic phase Mg_5Gd particles were dissolved after T4 treatment. The subsequent T6 treatment led to the precipitation of very fine metastable phases β' particles, elaborating the galvanic corrosion rate [33]. The above results suggest that T4 treatment can effectively improve the corrosion resistance of Mg alloys.

1.4.3 Surface coating

Surface coatings are of particular interest to Mg alloys as biodegradable implant materials because the corrosion rate is intended to be low in the initial phase due to the protective coating layer and then returns to the normal value when the layer corrodes away. This degradation mode is desirable since the implant is expected to provide sufficient mechanical strength support to the wound parts in the early stage and the implant should exhibit fast degradation rate after the tissue healing [34]. Many surface coating methods have been established for improving corrosion resistance of Mg alloys [35–37]. However, many of them are originally designed for industrial applications and might contain toxic materials. For orthopedic implant applications, the selection of coating material and method are very

important to effectively control the corrosion behavior as well as the biocompatibility of Mg alloys.

(1) Calcium phosphate coatings

Calcium phosphate coatings, such as hydroxyapatite, $Ca_{10}(PO_4)_6(OH)_2$, and its related compounds, have received great attention as it provides a protective coating to protect against corrosion especially in the initial stages after implantation, while also improving the ability of the implant to integrate into the surrounding tissue [34,37].

HAp is currently used as biomedical materials due to the facts that its chemical and structural similarities to bone and tooth minerals and has excellent biocompatibility and bioactivity [34,37]. HAp is practically coated on titanium-based implants to promote bone conduction for bone-implant integration. There are several methods used to form HAp coating on magnesium alloys. Among them, the chemical solution deposition process developed by Hiromoto et al. shows many advantages including its simplicity, low treating temperature, short processing time and formation of highly crystallized HAp coatings [38,39]. The results demonstrated that the HAp coating prepared on pure Mg, Mg-AZ31 and Mg-WE43 alloys by chemical solution method improved significantly the corrosion resistance and the cell biocompatibility of the substrates [38–42].

Although providing high corrosion protectiveness to Mg alloys, the corrosion of Mg substrate still can occur under the HAp coating. Because the degradation of HAp can take up to several years, the remaining of HAp coating may cause the loosening of devices due to the dissolution of Mg substrate. Thus, it is demanded to develop a corrosion protective coating with desirable degradation rate to avoid chronic inflammation [40]. It is worth mentioning that the biological apatite found in the natural bones is not stoichiometric HAp (Ca/P = 1.667) but the Ca-deficient HAp (Ca/P < 1.667) which contains various amounts of anionic (e.g. CO_3^{2-}, F^-, Cl^-) and/or cationic substitutions (e.g. Mg^{2+}, K^+, Sr^{2+}). Moreover, it has been reported that the incorporation of such ions in the HAp structure strongly affects its physical properties and biological behavior and responsiveness [43]. For these reasons, it is expected that the fabrication of calcium phosphate coatings with desirable properties can be achieved by single or multiple ionic substitutions within the HAp structure.

1.5 Objectives of the present thesis

In the present study, the influence of Zn content and solution heat treatment on the microstructure, corrosion behavior as well as the mechanical properties and mechanical integrity of the binary Mg-Zn alloys for orthopedic implant applications mainly investigated. The calcium phosphate coatings for reducing corrosion rate and improving *in vitro* biocompatibility of the Mg-Zn alloys are also developed. Consequently, the main objectives of the present study are described as follows:

(1) To elucidate the optimal Zn content and heat treatment condition for improving corrosion resistance of Mg-Zn binary alloys in a pseudo-physiological environment.

(2) To investigate the relationship between the microstructure and mechanical properties as well as the mechanical integrity of Mg-Zn binary alloys in Hanks' solution

(3) To fabricate a highly crystalline HAp coating on the Mg-Zn alloys by a single-step chemical solution deposition method and to reveal the correlation between the structure of HAp coating and the corrosion behavior of the coated alloys.

(4) To develop a carbonate-substituted apatite (CAp) coating on Mg-Zn alloys by modifying the previously developed HAp coating solution and to examine the enhanced corrosion resistance and *in vitro* biocompatibility of Mg-Zn alloys by CAp coating.

1.6 References

[1] M. Navarro, A. Michiardi, O. Castaño, J.A. Planell, Biomaterials in orthopaedics, J. R. Soc. Interface. 5 (2008) 1137–1158. https://doi.org/10.1098/rsif.2008.0151.

[2] M. Niinomi, Recent research and development in metallic materials for biomedical, dental and healthcare products applications, Mater. Sci. Forum. 539–543 (2007) 193–200. https://doi.org/10.4028/0-87849-428-6.193.

[3] M.P. Staiger, A.M. Pietak, J. Huadmai, G. Dias, Magnesium and its alloys as orthopedic biomaterials: A review, Biomaterials. 27 (2006) 1728–1734. https://doi.org/10.1016/j.biomaterials.2005.10.003.

[4] M. Niinomi, M. Nakai, Titanium-based biomaterials for preventing stress shielding between implant devices and bone, Int. J. Biomater. 2011 (2011). https://doi.org/10.1155/2011/836587.

[5] J.B. Park, J.D. Bronzino, Biomaterials: Principles and Applications, CRC Press, 2002.

[6] Y.F. Zheng, X.N. Gu, F. Witte, Biodegradable metals, Mater. Sci. Eng. R. 77 (2014) 1–34. https://doi.org/10.3390/met8100804.

[7] F. Witte, The history of biodegradable magnesium implants: A review, Acta Biomater. 6 (2010) 1680–1692. https://doi.org/10.1016/j.actbio.2010.02.028.

[8] J.M. Seitz, A. Lucas, M. Kirschner, Magnesium-Based Compression Screws: A Novelty in the Clinical Use of Implants, Jom. 68 (2016) 1177–1182. https://doi.org/10.1007/s11837-015-1773-1.

[9] R. Erbel, C. Di Mario, J. Bartunek, J. Bonnier, B. de Bruyne, F.R. Eberli, P. Erne, M. Haude, B. Heublein, M. Horrigan, C. Ilsley, D. Böse, J. Koolen, T.F. Lüscher, N. Weissman, R. Waksman, Temporary scaffolding of coronary arteries with bioabsorbable magnesium stents: a prospective, non-randomised multicentre trial, Lancet. 369 (2007) 1869–1875. https://doi.org/10.1016/S0140-6736(07)60853-8.

[10] Y. Zheng, Biodegradation Mechanism and Influencing Factors of Mg and Its Alloys, in: Magnes. Alloy. as Degrad. Biomater., 2016: pp. 37–68.

[11] R.-C. Zeng, Z.-Z. Yin, X.-B. Chen, D.-K. Xu, Corrosion Types of Magnesium Alloys, Magnes. Alloy. - Sel. Issue. (2018). https://doi.org/10.5772/intechopen.80083.

[12] G.L. Song, A. Atrens, Corrosion mechanisms of magnesium alloys, Adv. Eng. Mater. 1 (1999) 11–33. https://doi.org/10.1002/(SICI)1527-2648(199909)1:1<11::AID-ADEM11>3.0.CO;2-N.

[13] R. Willumeit, J. Fischer, F. Feyerabend, N. Hort, U. Bismayer, S. Heidrich, B. Mihailova, Chemical surface alteration of biodegradable magnesium exposed to corrosion media, Acta Biomater. 7 (2011) 2704–2715. https://doi.org/10.1016/j.actbio.2011.03.004.

[14] S. Hiromoto, Corrosion of metallic biomaterials, Met. Biomed. Devices. (2010) 99–121. https://doi.org/10.1533/9781845699246.2.99.

[15] X. Li, X. Liu, S. Wu, K.W.K. Yeung, Y. Zheng, P.K. Chu, Design of magnesium alloys with controllable degradation for biomedical implants: From bulk to surface, Acta Biomater. 45 (2016) 2–30. https://doi.org/10.1016/j.actbio.2016.09.005.

[16] S. Agarwal, J. Curtin, B. Duffy, S. Jaiswal, Biodegradable magnesium alloys for orthopaedic applications: A review on corrosion, biocompatibility and surface modifications, Mater. Sci. Eng. C. 68 (2016) 948–963. https://doi.org/10.1016/j.msec.2016.06.020.

[17] G. Eddy Jai Poinern, S. Brundavanam, D. Fawcett, Biomedical Magnesium Alloys: A Review of Material Properties, Surface Modifications and Potential as a Biodegradable Orthopaedic Implant, Am. J. Biomed. Eng. 2 (2013) 218–240. https://doi.org/10.5923/j.ajbe.20120206.02.

[18] M. Esmaily, J.E. Svensson, S. Fajardo, N. Birbilis, G.S. Frankel, S. Virtanen, R. Arrabal, S. Thomas, L.G. Johansson, Fundamentals and advances in magnesium alloy corrosion, Prog. Mater. Sci. 89 (2017) 92–193. https://doi.org/10.1016/j.pmatsci.2017.04.011.

[19] G. Song, Control of biodegradation of biocompatable magnesium alloys, Corros. Sci. 49 (2007) 1696–1701. https://doi.org/10.1016/j.corsci.2007.01.001.

[20] L. Yang, E. Zhang, Biocorrosion behavior of magnesium alloy in different simulated fluids for biomedical application, Mater. Sci. Eng. C. 29 (2009) 1691–1696. https://doi.org/10.1016/j.msec.2009.01.014.

[21] Y. He, C. Peng, Y. Feng, R. Wang, J. Zhong, Effects of alloying elements on the microstructure and corrosion behavior of Mg–Li–Al–Y alloys, J. Alloys Compd. 834

(2020) 154344. https://doi.org/10.1016/j.jallcom.2020.154344.

[22] D. Vojtěch, J. Kubásek, J. Šerák, P. Novák, Mechanical and corrosion properties of newly developed biodegradable Zn-based alloys for bone fixation, Acta Biomater. 7 (2011) 3515–3522. https://doi.org/10.1016/j.actbio.2011.05.008.

[23] T.B. Massalski, H. Okamoto, Binary Alloys Phase Diagrams, 2000. https://doi.org/10.1007/BF02645363.

[24] D. Pham, S. Hiromoto, E. Kobayashi, Influences of Zinc Content and Solution Heat Treatment on Microstructure and Corrosion Behavior of Mg-Zn Binary Alloys, Corrosion. 77 (2020) 323–338. https://doi.org/10.5006/3672.

[25] Y. Yan, H. Cao, Y. Kang, K. Yu, T. Xiao, J. Luo, Y. Deng, H. Fang, H. Xiong, Y. Dai, Effects of Zn concentration and heat treatment on the microstructure, mechanical properties and corrosion behavior of as-extruded Mg-Zn alloys produced by powder metallurgy, J. Alloys Compd. 693 (2017) 1277–1289. https://doi.org/10.1016/j.jallcom.2016.10.017.

[26] R. Zeng, W. Dietzel, F. Witte, N. Hort, C. Blawert, Progress and challenge for magnesium alloys as biomaterials, Adv. Eng. Mater. 10 (2008) 3–14. https://doi.org/10.1002/adem.200800035.

[27] J.. T. Black, R.A. Kohser, Materials & Processes in Manufacturing, Tenth Edit, 2007. https://doi.org/10.1002/9780470277270.

[28] American Society for Testing and Materials, Standard practice for heat treatment of magnesium alloys, Annu. B. ASTM Stand. (2006) ASTM Standard B661-06. https://doi.org/10.1520/G0005-14.2.

[29] G. Song, A.L. Bowles, D.H. StJohn, Corrosion resistance of aged die cast magnesium alloy AZ91D, Mater. Sci. Eng. A. 366 (2004) 74–86. https://doi.org/10.1016/j.msea.2003.08.060.

[30] G. Song, A. Atrens, M. Dargusch, Influence of microstructure on the corrosion of diecast AZ91D, Corros. Sci. 41 (1998) 249–273. https://doi.org/10.1016/S0010-938X(98)00121-8.

[31] X. Bin Liu, D.Y. Shan, Y.W. Song, E.H. Han, Effects of heat treatment on corrosion behaviors of Mg-3Zn magnesium alloy, Trans. Nonferrous Met. Soc. China (English

Ed. 20 (2010) 1345–1350. https://doi.org/10.1016/S1003-6326(09)60302-2.

[32] D.J. Lin, F.Y. Hung, T.S. Lui, M.L. Yeh, Heat treatment mechanism and biodegradable characteristics of ZAX1330 Mg alloy, Mater. Sci. Eng. C. 51 (2015) 300–308. https://doi.org/10.1016/j.msec.2015.03.004.

[33] N. Hort, Y. Huang, D. Fechner, M. Störmer, C. Blawert, F. Witte, C. Vogt, H. Drücker, R. Willumeit, K.U. Kainer, F. Feyerabend, Magnesium alloys as implant materials-Principles of property design for Mg-RE alloys, Acta Biomater. 6 (2010) 1714–1725. https://doi.org/10.1016/j.actbio.2009.09.010.

[34] N. Nassif, I. Ghayad, Corrosion protection and surface treatment of magnesium alloys used for orthopedic applications, Adv. Mater. Sci. Eng. 2013 (2013). https://doi.org/10.1155/2013/532896.

[35] G. Wu, J.M. Ibrahim, P.K. Chu, Surface design of biodegradable magnesium alloys - A review, Surf. Coatings Technol. 233 (2013) 2–12. https://doi.org/10.1016/j.surfcoat.2012.10.009.

[36] J.E. Gray, B. Luan, Protective coatings on magnesium and its alloys - A critical review, J. Alloys Compd. 336 (2002) 88–113. https://doi.org/10.1016/S0925-8388(01)01899-0.

[37] H. Hornberger, S. Virtanen, A.R. Boccaccini, Biomedical coatings on magnesium alloys – A review, Acta Biomater. 8 (2012) 2442–2455. https://doi.org/10.1016/j.actbio.2012.04.012.

[38] S. Hiromoto, M. Tomozawa, Corrosion behavior of magnesium with hydroxyapatite coatings formed by hydrothermal treatment, Mater. Trans. 51 (2010) 2080–2087. https://doi.org/10.2320/matertrans.M2010192.

[39] S. Hiromoto, A. Yamamoto, High corrosion resistance of magnesium coated with hydroxyapatite directly synthesized in an aqueous solution, Electrochim. Acta. 54 (2009) 7085–7093. https://doi.org/10.1016/j.electacta.2009.07.033.

[40] S. Hiromoto, S. Itoh, N. Noda, T. Yamazaki, T. Akashi, Osteoclast and osteoblast responsive carbonate apatite coatings for biodegradable magnesium alloys, Sci. Technol. Adv. Mater. 21 (2020) 346–358. https://doi.org/10.1080/14686996.2020.1761237.

[41] S. Hiromoto, T. Yamazaki, Micromorphological effect of calcium phosphate coating on compatibility of magnesium alloy with osteoblast, Sci. Technol. Adv. Mater. 18 (2017)

96–109. https://doi.org/10.1080/14686996.2016.1266238.

[42] S. Hiromoto, M. Tomozawa, Hydroxyapatite coating of AZ31 magnesium alloy by a solution treatment and its corrosion behavior in NaCl solution, Surf. Coat. Technol. 205 (2011) 4711–4719. https://doi.org/10.1016/j.surfcoat.2011.04.036.

[43] I. Cacciotti, Multisubstituted hydroxyapatite powders and coatings: The influence of the codoping on the hydroxyapatite performances, Int. J. Appl. Ceram. Technol. 16 (2019) 1864–1884. https://doi.org/10.1111/ijac.13229.

Table 1.1 Summary of the physical and mechanical properties of various orthopedic implant materials in comparison to human cortical bone [3].

	Density (g/cm^3)	Elastic modulus (GPa)	Compressive yield strength (MPa)	Fracture toughness ($MPam^{1/2}$)
Cortical bone	1.8-2.1	3-20	130-180	3-6
Mg	1.74-2.0	41-45	65-100	15-40
Ti alloy	4.4-4.5	110-117	758-1117	55-115
Co-Cr alloy	8.3-9.2	230	450-1000	N/A
Stainless steel	7.9-8.1	189-205	170-310	50-200
Synthetic HAp	3.1	73-117	600	0.7

Figure 1.1 MAGNEZIX® compressive screw (CS) in different sizes. From left to right: MAGNEZIX® CS 2.0, MAGNEZIX® CS 2.7, MAGNEZIX® CS 3.2 and MAGNEZIX® CS 4.8 [8].

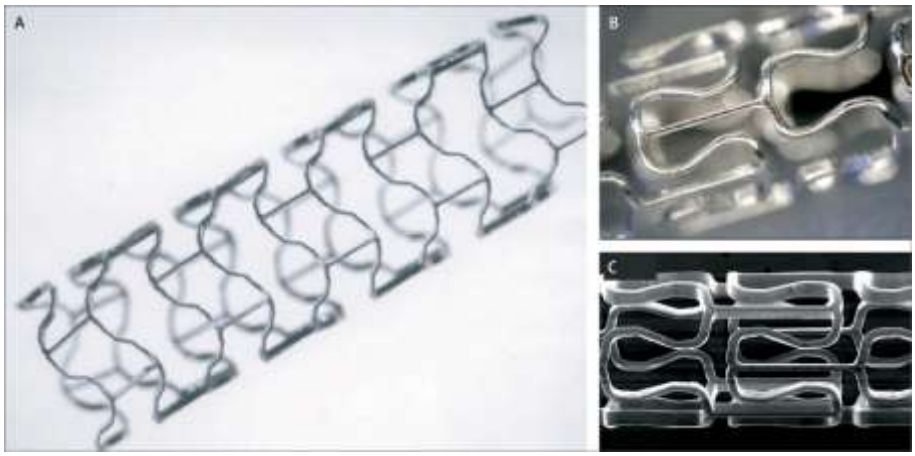

Figure 1.2 Bioabsorbable magnesium stent (BIOTRONIK, Berlin, Germany) (A) after expansion, (B) before expansion, and (C) in an electron microscopy magnification [9].

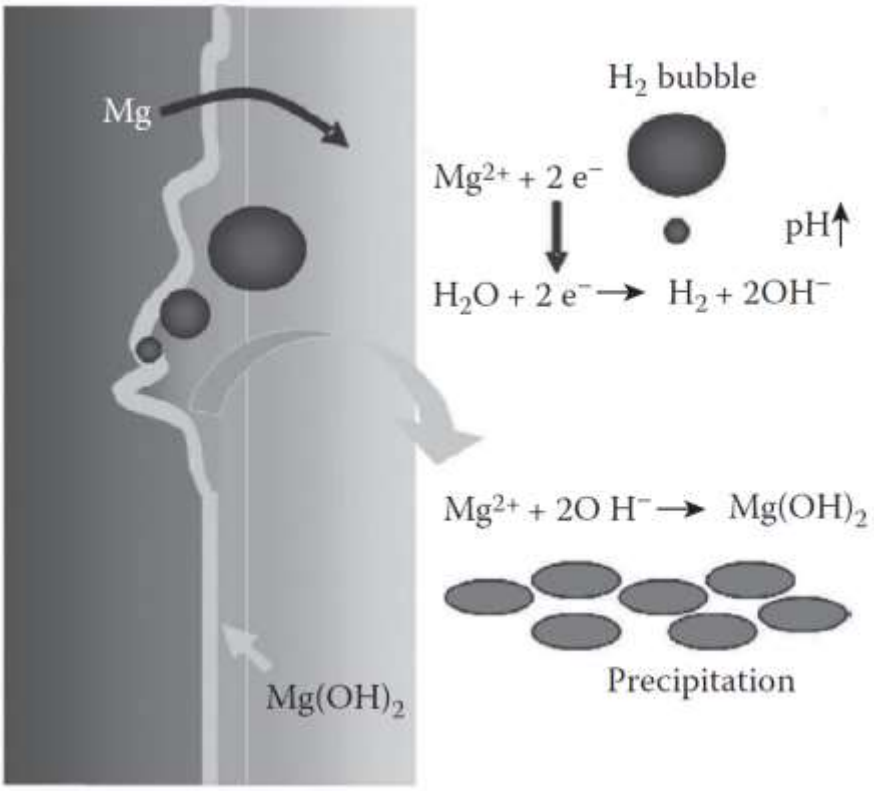

Figure 1.3 Schematic illustration of Mg degradation [10].

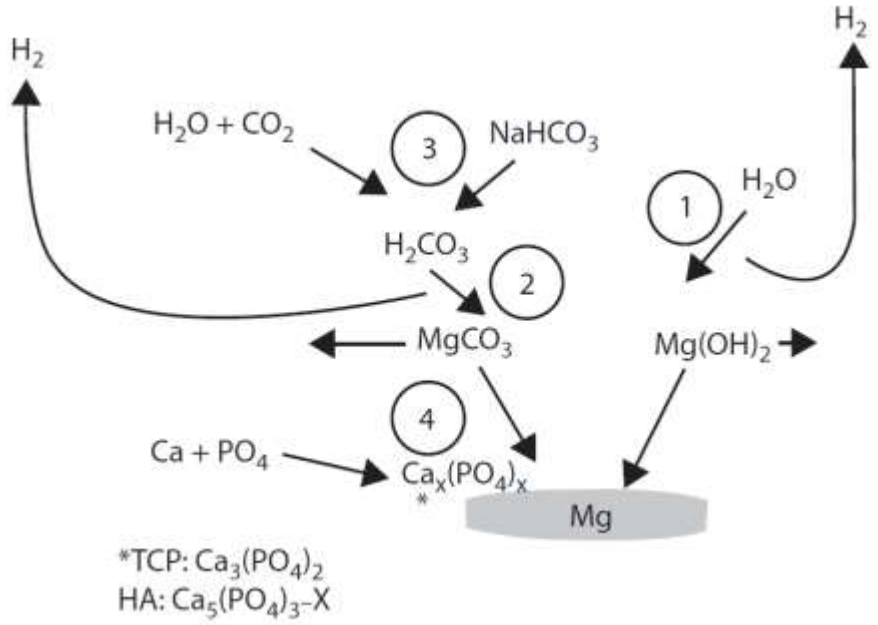

Figure 1.4 Summary of possible corrosion product formation during the initial steps of Mg corrosion in cell culture medium. (1) $Mg(OH)_2$ formation due to contact with water, (2) $MgCO_3$ formation due to the presence of carbon dioxide, (3) increase in the content of hydrogen carbonate due to the buffering system, and (4) biomineralization due to the introduction of calcium. The asterisk denotes possible products (TCP = tricalcium phosphate, HA = hydroxyapatite, X = OH, Cl,...) [13].

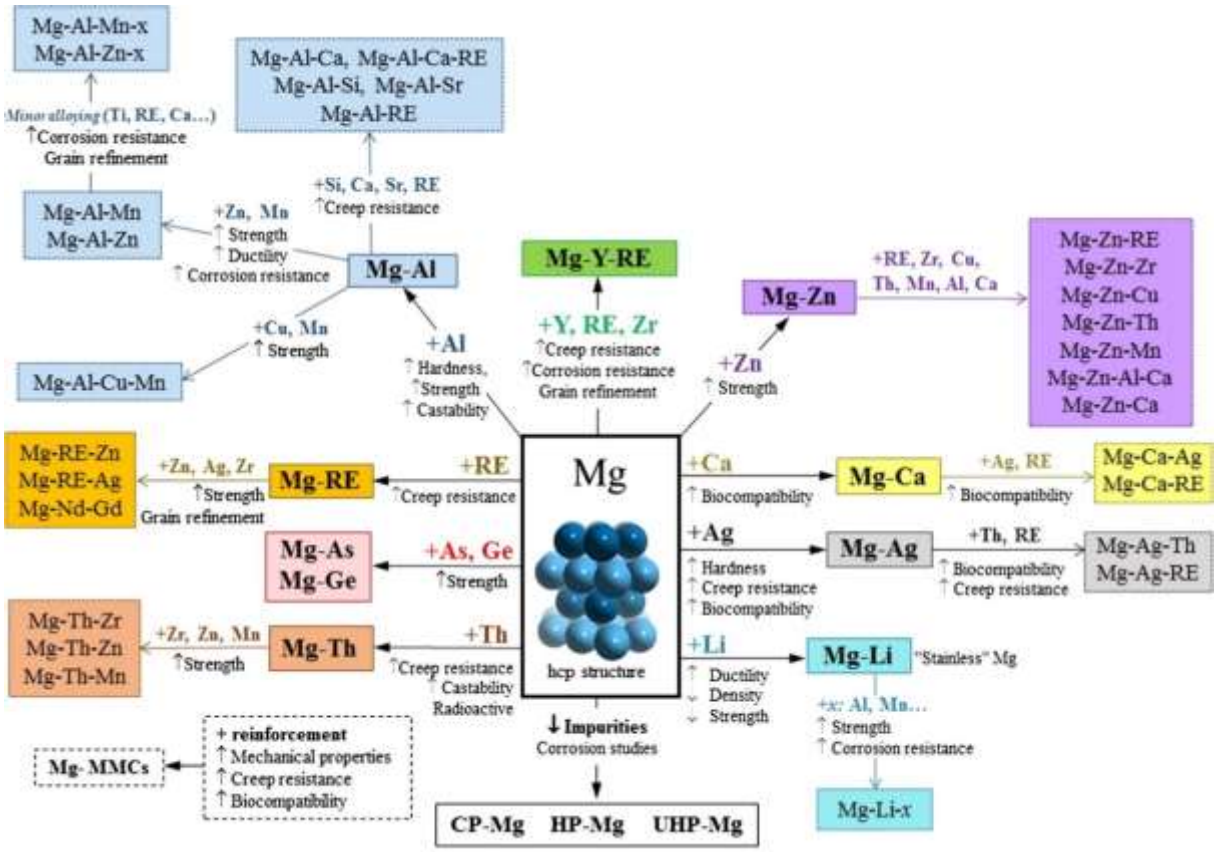

Figure 1.5 Summary of the development of Mg alloys [18].

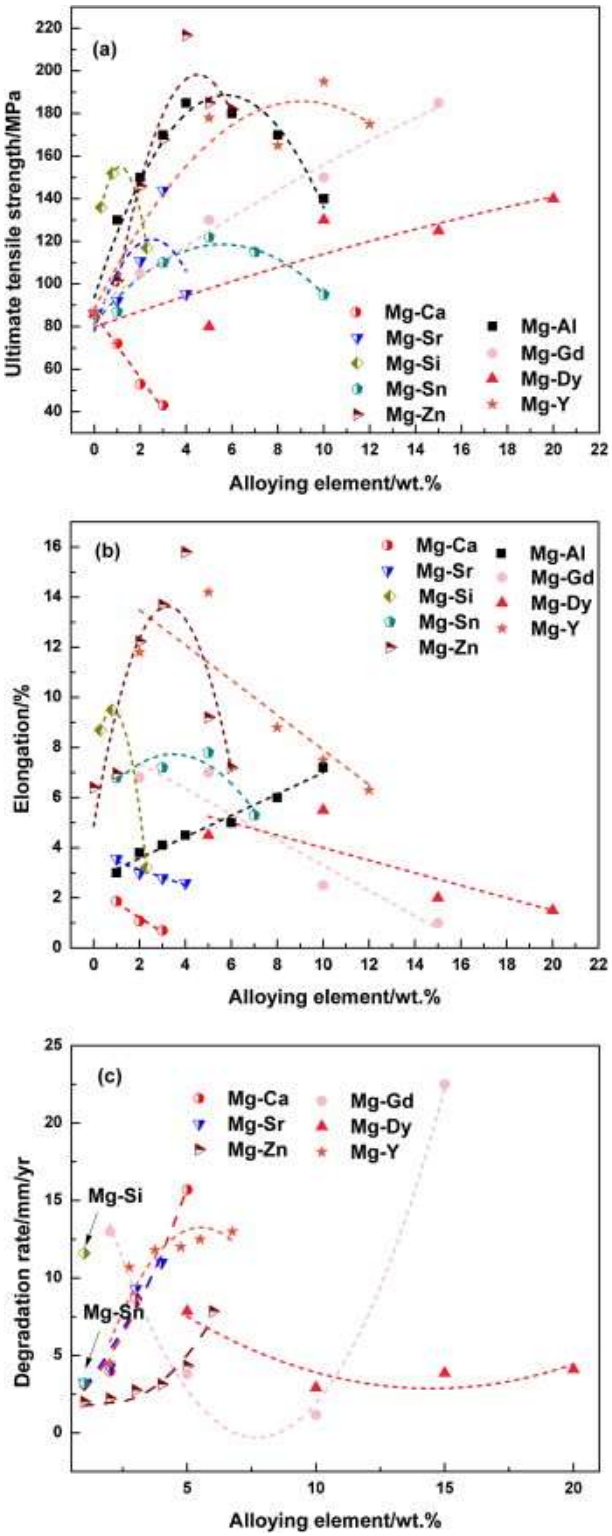

Figure 1.6 Summary of mechanical properties and corrosion rate for binary Mg-X alloys [6].

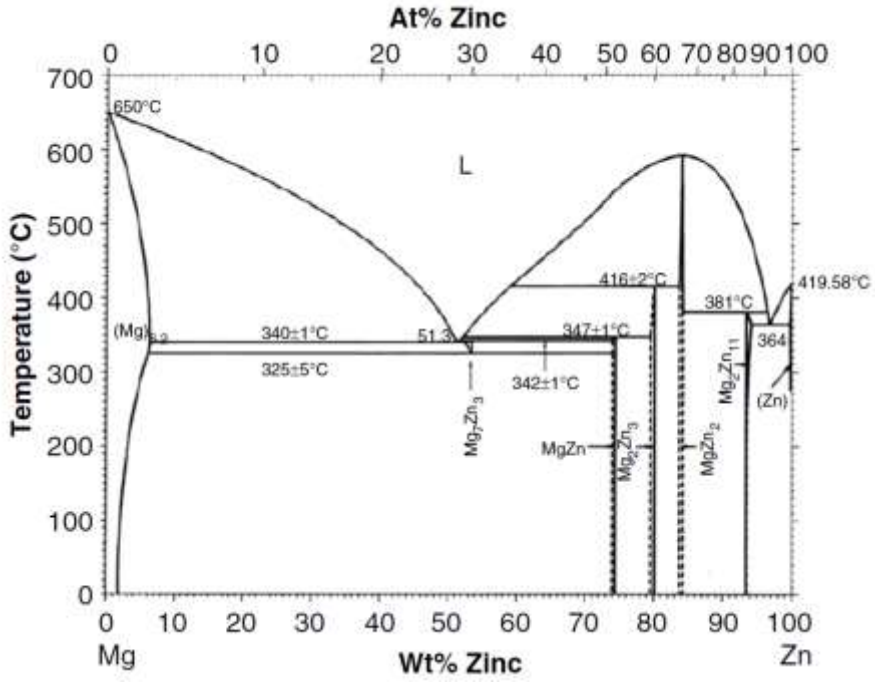

Figure 1.7 Phase diagram of Mg-Zn binary alloy [23].

Chapter 2

Influences of Zinc Content and Solution Heat Treatment on Microstructure and Corrosion Behavior of Mg-Zn Binary Alloys

2.1 Introduction

Magnesium (Mg) and Mg alloys have been extensively investigated as promising candidates for biodegradable implant applications due to their excellent biocompatibility and Young's modulus comparable to human cortical bones [1–3]. Reducing the difference in Young's modulus between implants and human bones can avoid the stress-shielding effect which causes the delay of broken bone healing and the reduction in bone density [4]. However, the practical application of Mg alloys as implant biomaterials is very limited due to their rapid degradation in physiological environments which causes the loss of mechanical integrity [5,6]. There have been many studies on Mg alloys as biomedical materials. Nonetheless, most of the reported Mg alloys such as AZ31, AZ91, AM60, WE43 and LAE442 alloys are originally designed for industrial applications. Although having suitable mechanical properties and moderate corrosion rates, these alloys contain aluminum, rare earth elements or other elements of which the biological compatibility is poor or not precisely understood [7–9]. Therefore, the selection of alloying elements for Mg alloys should be carefully considered when they are designed for biomedical applications. Among several potential candidates, Zn-containing Mg alloys are attracted great interests because Zn is also a biodegradable element and the addition of Zn to magnesium matrix improved both mechanical properties and corrosion resistance of magnesium [10–16]. In addition, Zn is biocompatible element and has a relatively high daily allowance (~15 mg) [17]. Therefore, from both mechanical and biological aspects, Zn is a potential candidate for binary Mg alloys as a biodegradable material.

Figure 2.1 shows a phase diagram of the Mg-Zn binary alloy [18]. It can be seen that the maximum solid solubility of Zn in Mg at room temperature in the equilibrium state is about 1.6 wt% and thus the Zn elements tend to incorporate as solution atoms in Mg matrix of the

alloys with Zn content less than 1.6 wt%. With further increasing Zn content, more Mg-Zn intermetallic compounds are formed in the structure, resulting in the grain refinement. When the content of Zn exceeds 6.2 wt% which is the solid solubility limit for Zn in Mg at 341 ^{o}C, amount of the intermetallic compounds in the structure increases rapidly. For these reasons, the studies on Mg-Zn binary alloys as biodegradable materials often give attention to the content of Zn in the range from 0.5 wt% up to 7 wt%. Cai et al. [10] studied the microstructure and corrosion resistance of as-cast Mg-1, 5, 7 wt% Zn alloys in a simulated body fluid. It was reported that Zn can significantly refined the grain size and the addition of Zn content over 5 wt% resulted in the formation of MgZn second phase. Moreover, the corrosion resistance of Mg-Zn alloys increased until the Zn content reached 5 wt%; exceeding that concentration, the corrosion resistance of the alloy decreased. A study by Koç et al. [11] addressed the enhancement of the general and localized in vitro corrosion resistance of as-cast Mg-0.5, 1, 2, 3 wt% Zn alloys with an increase of Zn content (from 0.5 to 3.0 wt%). It should be noted that although MgZn second phase was observed in the microstructure of Mg-3 wt% Zn alloy, their volume fraction did not appear to be very high. Song et al. [15] examined the corrosion behavior of extruded Mg-2, 3, 4, 5 wt% Zn alloys in a 3.5 wt% NaCl solution. They reported that the Mg-2 wt% Zn alloy exhibited the highest corrosion resistance while the Mg-5 wt% Zn alloy showed the lowest corrosion resistance, which was attributed to the volume fraction of Mg_xZn_y second phases in Mg-Zn alloys rise with increasing Zn content. Kubàsek et al. [16] studied the structural characteristics and corrosion behavior of as-cast Mg alloys containing 1 and 3 wt% Zn in a 0.9 wt% NaCl solution. It was found that the non-equilibrium eutectic mixture of α-Mg and MgZn was formed in both alloys and the amount of MgZn second phase was higher in the Mg-3 wt% alloy. As a result, Mg-1 wt% Zn alloy exhibited the higher corrosion resistance than Mg-3 wt% Zn alloy. This controversy over the optimal Zn content for corrosion resistance of binary Mg-Zn alloys was remained among the low Zn addition (1 wt% or less) and the high Zn addition (5 to 6 wt%). Meanwhile, heat treatment is also an effective method to modify the microstructure, contributing to adjust the corrosion behavior of magnesium alloys. It was reported that the solution treatment (T4 treatment) improved the corrosion resistance while the aging treatment (T6 treatment) reduced the corrosion resistance of some Mg-Zn alloys with the Zn content range from 3 wt% to 6 wt% [19–21]. Therefore, there is a need for a comprehensive study on the effect of Zn content and heat treatment on microstructure and in-vitro corrosion behavior of the binary Mg-Zn alloys.

In the present study, Mg-xZn binary alloys (x=1, 3, 5 and 7 wt%) were prepared by a simple gravity casting into a copper mold, the as-cast samples were subsequently adopted to T4 solution heat treatment. The influence of Zn content and heat treatment on the microstructure and corrosion behavior of the Mg-Zn alloys were studied with immersion test and electrochemical measurements in Hanks' solution.

2.2 Experimental procedures

2.2.1 Materials preparation

Mg-Zn alloys were prepared from high purity Mg ingots (> 99.9 wt%, Osaka Asahi Metal) and high purity Zn shots (> 99.99 wt%, Osaka Asahi Metal) with various Zn contents (1, 3, 5 and 7 wt%). The melting process was conducted using an electrical resistance furnace under protection with a 95 vol% Ar + 5 vol% CH_2FCF_3 mixed gas atmosphere (Kayama Oxygen) at 750 ^oC. The molten metals were kept and gently stirred for 10 min to ensure the homogenization. The molten metals then were casted into a copper mold at room temperature to prepare the cylindrical ingots with the dimensions of 25 mm in diameter and 70 mm in length. The chemical composition analysis of alloys was carried out with an inductively coupled plasma–optical emission spectrometry (ICP–OES). The results were shown in Table 2.1.

T4 solution heat treatment was conducted on the cast ingots in a high vacuum heat induction furnace at 400 ^oC for 12 h and subsequently quenched in water at room temperature. Both as-cast and T4-treated ingots were machined to a cylindrical shape with the dimensions of 15 mm in diameter and 70 mm in length by computer numerical control (CNC) machining. The cylindrical ingots were cut into disk with 2 mm in thickness for further analysis and experiments. The names and preparation conditions of various types of specimens were noted in Table 2.2.

2.2.2 Characterization method

The specimen surface for metallographic observation were ground with SiC papers up to 4000 grit, and successively polished with 3 μm diamond paste, and ultrasonically rinsed in acetone for 60 s. X-ray diffractometry (XRD, Rigaku, RINT–2100) was conducted to analyze phase constitutions. Scanning electron microscopy (SEM, Hitachi, TM-1000), field-emission scanning electron microscopy (FE–SEM, JEOL, JSM-7200F) equipped with energy dispersion

X-ray spectrometry (EDS) were used to characterize the morphology and composition. The volume fraction and average size of the particles were measured from SEM images using ImageJ analysis software.

Electrochemical measurements and static immersion test were performed in Hanks' solution. The chemical composition of Hanks' solution is shown in Table 2.3. Each disk with a total surface area of 4 cm^2 were immersed in 200 mL of Hanks' solution in a plastic container and the container was placed in an incubator at 37 ^oC. On Days 1, 3, 5, 7, 9, 11, 13 and 14 of immersion, 10 µL of solution was sampled for Mg^{2+} quantification. The concentration of Mg^{2+} ions released in Hanks' solution was quantified by a colorimetric method using Xylidyl blue–I (1-azo-2-hydroxy-3-(2,4-dimethylcarboxya-nilido)naphthalene-1-(2-hydroxybenzene-5 sulfonate) [22–24].

Magnesium ions combine with Xylidyl blue-I to form a water soluble chelate which absorbs light with a wave length of 520 nm. Then, the absorbance at 520 nm was measured with a microplate Spectrophotometer (Thermo Scientific, Multiskan GO).

The amount of Mg^{2+} ions released per each day was given by equation (2.1) [24]:

$$A_i = 0.0275C_i - (0.0275 - 0.015)C_{i-1} \quad (2.1)$$

where C_i is the concentration of Mg^{2+} ions (mg/L) in the testing solution at day i and A_i is the total amount of Mg^{2+} ions (mg) at day i. The accumulated Mg^{2+} ions released per unit surface area (mg/cm^2) was calculated by equation (2.2) [24]:

$$R_i = \frac{A_i}{S_0} \quad (2.2)$$

where S_0 is the total surfaces area (cm^2) of the samples before immersion test

Three disks from each alloy sample were used for the immersion test. After 14 days of immersion, the samples were removed from the testing solution, rinsed with distilled water and dried with a N_2 gas flow. A solution of $AgNO_3$ (17 g/L) and CrO_3 (200 g/L) was used to remove the corrosion products. The surface of samples for potentiodynamic polarization and electrochemical impedance measurement was covered by Teflon tape remaining an area of 1-cm^2 exposed as a working electrode in 500 ml of Hanks' solution at 37 ^oC. A saturated Ag/AgCl electrode and a platinum plate were used as the reference and counter electrodes, respectively. In polarization tests, the open-circuit potential (OCP) was monitored for 1.8 ks; subsequently, the potential of the sample was swept from –0.1 V vs. OCP at a scan rate of 1 mV/s.

Electrochemical impedance spectroscopy (EIS) was measured after 0, 0.5, 1, 2, 4 and 6 h of immersion at the open circuit potential (OCP) at each measurement time. The scan frequency ranged from 10^5 Hz to 10^{-2} Hz with a perturbation amplitude of 5 mV. A part of the EIS spectra were analyzed using the ZView software.

2.3 Result and discussions

2.3.1 Microstructure observation

The X-rays diffraction patterns of the as-cast and T4-treated samples are shown in Figure 2.2. As could be seen in Fig. 2.2(b), the sample A1 showed only peaks of α-Mg matrix and no peak of second phase. The peak of (3 2 7) and (0 5 7) planes of MgZn intermetallic phase was identified on the samples A2, A3 and A4 with Zn content over 3 wt%. The intensities of MgZn peaks increased as the Zn content increased. After the T4 treatment, a reduction of MgZn peak intensities was recognized in the diffraction patterns shown in Fig. 2.2(c). While it was not identified on the samples $A2_T$ and $A3_T$; the peak intensity of MgZn intermetallic compound on the sample $A4_T$ was lower than that on the sample A4. The decrease in diffraction peak intensities was explained by the dissolution of MgZn intermetallic phase into α-Mg matrix during the T4 treatment.

The back-scattering electron (BSE) images of the as-cast and T4-treated alloys are shown in Figure 2.3. Due to the large difference in atomic number between Mg and Zn element, the images clearly revealed the microstructure of the as-cast alloys consisted of primary α-Mg matrix (dark-grey region), Zn-segregated region (light-grey region) and Zn-rich cells (white particle). The Zn-rich cells discretely distributed between the dendrite arms of the primary Mg grains. A close-up image of a Zn-rich cell disclosed a typical eutectic lamellar structure as shown in Fig. 2.3(d). Thus, hereafter it is called eutectic cell. The microstructure of the as-cast Mg-Zn alloys was formed due to the non-equilibrium solidification. As the start of the solidification process, the primary α-Mg grains firstly formed and Zn was rejected from the α-Mg into the liquid. Consequently, upon further cooling, the segregation of Zn took place at the grain boundaries and formed a network structure. Once the temperature of molten metal dropped to the eutectic temperature at 341°C, the eutectic reaction occurs as following [18]:

$$L_E \rightarrow Mg_7Zn_3 + MgZn \quad (2.3)$$

where L_E is liquid phase at eutectic composition.

However, in this study, there was no clear evidence on the existence of meta-stable Mg_7Zn_3 intermetallic compound in the microstructure of the as-cast alloys. The absence of Mg_7Zn_3 intermetallic compound was explained by the rapid solidification of the molten metal and the narrow temperature range where Mg_7Zn_3 intermetallic compound is stable, so that the formation of Mg_7Zn_3 phase was easily skipped in this condition. Hence, instead of the equation (2.3), the eutectic reaction was alternatively changed to:

$$L \rightarrow \alpha\text{-Mg} + MgZn \quad (2.4)$$

Consequently, in a correlation with XRD results, the eutectic cells are (α-Mg + MgZn) phases.

It is worth to note that the volume fraction of the (α-Mg + MgZn) eutectic cells increased with increasing Zn content up to 7 wt%. Although the volume fraction of MgZn phase in the alloys was not directly measured, it could be estimated from the volume fraction of (α-Mg + MgZn) eutectic cells in the alloys. The volume fraction and average size of (α-Mg + MgZn) cells was listed in Table 2.4. The (α-Mg + MgZn) eutectic cells were 0.07, 0.99, 2.18 and 2.87 vol% for the as-cast Mg-1Zn, Mg-3Zn, Mg-5Zn and Mg-7Zn alloys, respectively. The results demonstrated that the volume fraction of MgZn phase in the as-cast Mg-Zn alloys increased with Zn addition.

The microstructure of the Mg-Zn alloys significantly changed after the T4 treatment at 400 ^oC for 12 h. As could be seen in Fig. 2.3(e–h), the Zn-segregated region was not formed because Zn atoms had no time to segregate during the water quenching. The (α-Mg + MgZn) cells disappeared in the samples $A1_T$, $A2_T$ and $A3_T$, while the eutectic cells precipitated in the sample $A4_T$. In addition, the eutectic cells precipitated in grain boundaries and within grains in the sample $A4_T$, indicating that the original eutectic cells re-melted and solidified during the T4 treatment. The average (α-Mg + MgZn) cell size in the sample A4 and $A4_T$ was 2.14 and 27.76 μm, respectively. Although the eutectic cell size increased significantly, the total volume fraction of the eutectic cells decreased from 2.87 vol% in the sample A4 to 1.73 vol% in the sample $A4_T$ after the heat treatment. The decrease in volume fraction of (α-Mg + MgZn) cells and the disappearance of Zn-segregated region suggested that there were more Zn atoms

dissolved in the Mg matrix. Consequently, the distribution of Zn element was homogenized after the T4 treatment.

There were also some small precipitation particles randomly observed in the samples $A1_T$, $A2_T$ and $A3_T$. EDS analysis confirmed that the main components of these precipitates were Mg and impurity element Si. The existence of precipitates consisting of Mg and Si was reported in the literature [15]. In the current study, considering that the volume fraction and size of these precipitates are very small compared to the MgZn particles, the effect of these precipitates on corrosion behavior of the Mg-Zn alloys could be negligibly small compared to that of MgZn particles.

The EDS elemental mapping of the samples A4 and $A4_T$ is shown in Figure 2.4. The mapping of Mg and Zn element proved that the (α-Mg + MgZn) eutectic cells and Zn-segregated regions formed a dense network structure in the sample A4, as shown in Fig. 2.4(b, c). After the heat treatment, the segregation of Zn disappeared and the network structure was not formed as shown in Fig. 2.4(e, f). The EDS analysis at points P1, P2 and P3 corresponding to the Mg matrix and Zn-segregated region of the sample A4, and the Mg matrix of the sample $A4_T$, respectively. The measurements were carried out three times at each region and the average results were obtained. The Zn content at points P1, P2 and P3 was 1.24 ± 0.06, 3.39 ± 0.13, 4.25 ± 0.06 wt%, respectively. The results proved that the Zn-segregated region had a higher Zn content than the Mg matrix of the sample A4 and the Zn content of the Mg matrix increased after the T4 treatment.

2.3.2 Surface appearance of Mg-Zn alloys after static immersion test in Hanks' solution

The optical image of the samples after 14 days-immersion tests are shown in Figure 2.5. The surface appearances showed filiform corrosion morphology of worm-like structure (as indicated by black arrows), implying that the filiform corrosion dominantly occurred on all the samples. The filiform corrosion became wider and deeper and the total corroded area increased with an increase of Zn content. As for the as-cast alloys, the sample A1 showed the least corrosion with only a small area near the periphery was covered with filiform corrosion. The sample A2 exhibited a similar appearance to the sample A1. The sample A3 showed a large corroded area, and nearly the whole surface of the sample A4 showed filiform corrosion appearance. There were only a few corrosion pits randomly appeared on the sample A4. The influence of the T4 treatment on the corrosion morphology was significant for Mg-5Zn and

Mg-7Zn alloys. The total corroded areas on the samples $A3_T$ and $A4_T$ were remarkably smaller than those on the samples A3 and A4, respectively. In addition, no pitting corrosion was observed on the sample $A4_T$.

The BSE images of the samples A1, A4 and $A4_T$ after the 14 days-immersion tests with corrosion products on the samples' surface are shown in Figure 2.6(a-c) and those after removing the corrosion products were shown in Figure 2.6(d-f). The observation regions of Fig. 2.6(d-f) were different from those of Fig. 2.6(a-c), respectively. The enlarged views of the corroded area marked by black squares in Fig. 2.6(e) and (f) are shown in Fig. 2.6(g) and (h), respectively. Apparently, after the 14 days of immersion in Hanks' solution, the surface of all the samples was fully covered with the corrosion products. On the sample A1, the corrosion product layer was uniform and showed no apparent defects. The polishing scratches were visible, indicating the deposited layer on this sample was thin. On the sample A4, the severely corroded area appeared as holes filled with large amount of corrosion products, as shown in Fig. 2.6(b). The deposited layer on the non-corroded area on the sample $A4_T$ was as uniform as that on the sample A1. While the layer on the filiform corrosion showed micro-cracks, which may be formed when drying the sample, as shown in Fig. 2.6(c).

To analyze the corrosion morphology of Mg-Zn alloys, the corrosion products were removed with a chromic acid solution. The surface of the sample A1 in Fig. 2.6(d) was well protected after 14 days immersion, while micro pits were formed along the polishing scratches. The surface appearances shown in Fig. 2.6(e, f) proved that the sample A4 were corroded much severe than the sample $A4_T$. The corroded area on the sample A4 showed many deep holes located in the grooves of filiform corrosion, as shown Fig. 2.6(g). The formation of these holes was attributed to the severe dissolution of α-Mg matrix which occurred as a result of the galvanic coupling between the cathodic Zn-rich phases and the anodic α-Mg matrix. These holes were separated by the thin walls which are supposed to be the Zn-segregated network. On the sample $A4_T$, the filiform grooves were shallow comparing to those on the sample A4. The inset figure in Fig. 2.6(f) showed a (α-Mg + MgZn) eutectic cell with a groove around the cell, which was a clear evidence of the dissolution of α-Mg matrix around the (α-Mg + MgZn) eutectic cell. On this sample, the dissolution of α-Mg matrix was moderate to remain the (α-Mg + MgZn) cells in the microstructure. The corrosion morphology of the samples after the removal of corrosion products showed a well correlation to the Zn element distribution pattern in Fig. 2.4.

The BSE cross-sectional images of the samples A1, A4 and $A4_T$ after the immersion tests in Hanks' solution for 14 days are shown in Figure 2.7(a-c) and the EDS results of the corresponding deposit layers are shown in Figure 2.7(d-f). The EDS results revealed that the deposit layers consisted of O, Mg, Ca and P and trace amount of Zn. It should be noted that a part of Mg and Zn could be originated from the substrate alloys because thickness of the deposit layers was relatively small compared to the X-ray generation range. Witte et al. previously reported that calcium phosphate mainly deposited on Mg alloys in simulated body fluid [25]. Kuwahara et al. pointed out that magnesium apatite was formed as a by-product on Mg in Hanks' solution [26]. These facts indicated that calcium phosphate compound was the main deposit and magnesium and zinc phosphate compounds deposited as by products in this case.

It was clearly observed that a uniform layer of calcium phosphate covered the surface of the sample A1 with a thickness of about 0.9-0.95 μm. On the sample A4, corroded region of α-Mg matrix was observed in dark grey around a eutectic cell and a crack was formed in the corrosion layer. The calcium phosphate layer with some cracks was formed on the A4 surface and its thickness varied from 1.5-1.6 μm. Deposition of calcium phosphate particles on the layer was observed preferentially over the corroded α-Mg matrix, and the calcium phosphate layer slightly detached from the corrosion layer, indicating the adhesiveness of the calcium phosphate layer was relatively low. In case of the sample $A4_T$, the calcium phosphate layer uniformly covered α-Mg matrix with a thickness of about 1.2-1.3 μm. Meanwhile, the areas where the large size eutectic cells exposed on the surface showed less amount of the deposited products.

2.3.3 Mg^{2+} ion release behavior in Hanks' solution

The accumulated Mg^{2+} ion release curves of various samples in Hanks' solution up to 14 days are shown in Figure 2.8. The insets of Fig. 2.8(a) and (b) are the magnified curves in the early stage (up to 4 days). As could be seen, the Mg^{2+} ion release from the as-cast samples showed almost linear after Day1. The average Mg^{2+} ion release rate from Day1 to Day14 was 0.028, 0.057, 0.098 and 0.281 $mg \cdot cm^{-2} \cdot d^{-1}$ for Mg-1Zn, Mg-3Zn, Mg-5Zn and Mg-7Zn alloys, respectively. The acceleration of the release rate was thus attributed to the increase of the volume fraction of (α-Mg + MgZn) eutectic cells and the formation of Zn-segregated network. The MgZn intermetallic compound and Zn-segregated phase were expected to show higher corrosion potential than the Mg matrix due to the higher standard potential of Zn than that of Mg. Scanning Kelvin Probe force microscopy characterization revealed that the $MgZn_2$ phase showed ca. 550 mV higher Volta potential than Mg matrix in Mg–6 wt% Zn–1 wt% Mn–5 wt%

Si–0.8 wt% Ca alloy in air [27]. Therefore, the (α-Mg + MgZn) eutectic cells and Zn-segregated network acted as micro-cathodes while Mg matrix acted as a micro-anode, and micro-galvanic corrosion occurred on the as-cast alloys. The increase in the volume fraction of (α-Mg + MgZn) cells and Zn-segregated phase resulted in the enhancement of cathode reaction, leading to the escalation of the corrosion rate.

The Mg^{2+} ion release rate linearly depended on the volume fraction of the eutectic cells in the A1, A2 and A3 samples and the A4 sample showed a significantly higher release rate than that expected from the volume fraction of the eutectic cells as shown in Figure 2.9. The eutectic cells in the sample A4 were in a worm-shape while those in the other samples were in a round shape, indicating that the former specific surface area was larger than the latter area. The Zn content, 7 wt%, was higher than the Zn solubility limit of Mg, 6.2 wt% [18], implying that the volume ratio of Zn-segregated network of the sample A4 was remarkably higher than those of the other samples. These facts presumably caused the significantly high Mg^{2+} ion release rate of the sample A4.

The samples A1, A2 and A3 showed highest Mg^{2+} ion release rate in the first day, and the subsequent Mg^{2+}ion release rate decreased and it was constant for 14 days. On the contrary, the release rate of the sample A4 increased after Day1. The contradictory trends suggested the different corrosion behavior of the sample A4 from the other samples. In the case of the samples A1, A2 and A3, the retardation of Mg^{2+} ion release after Day1 was attributed to the formation of a compact calcium phosphate layer on surface of these samples. However, in the sample A4, severe galvanic corrosion between the large numbers of (α-Mg + MgZn) eutectic cells and Mg matrix caused many defects on the calcium phosphate layer. The defects were unable to be covered by the further deposition of calcium phosphates, resulting in the acceleration of Mg^{2+} ion release after Day1.

The quantities of Mg^{2+} ion release from the T4-treated samples were smaller than those from the as-cast samples, indicating the corrosion resistance of Mg-Zn alloys was improved by the solution heat treatment. The result was attributed to the two factors: the decrease in number of micro-cathodes owing to the dissolution of (α-Mg + MgZn) eutectic cells and the decrease in the potential difference between (α-Mg + MgZn) eutectic cells and α-Mg matrix owing to the increase in Zn concentration of the α-Mg matrix. The Mg^{2+} ion release rate was the highest in the first day and gradually decreased in the later stage of the immersion period. This result was attributed to the corrosion protection ability of the calcium phosphate layer. The corrosion rate of the sample $A4_T$ was slightly higher than that of the other T4-treated samples, indicating

that the presence of the eutectic cells caused the lower corrosion protectiveness of the calcium phosphate layer. The amounts of Mg^{2+} ion release of the Mg-Zn alloys was consistent with the ratios of corroded areas shown in Fig. 2.5.

2.3.4 Potentiodynamic polarization behavior

The potentiodynamic polarization curves of the as-cast and T4-treated samples are shown in Figure 2.10. In the case of Mg alloys, the cathodic reaction is the hydrogen evolution reaction and the anodic reaction is the dissolution of Mg [28]. As could be seen, the cathodic current density of the as-cast Mg-Zn alloys increased with the Zn addition. The elevation in the cathodic current density was associated with the increase in volume fraction of (α-Mg + MgZn) cells and Zn-segregated network which acted as the micro-cathodes in galvanic corrosion. After the T4 treatment, the cathodic current density decreased by nearly 1 order of magnitude, which was attributed to the two factors: (i) the dissolution of (α-Mg + MgZn) cells and Zn-segregated network, and (ii) the increase in Zn concentration of the Mg matrix.

The corrosion potential (E_{corr}) of the as-cast and T4-treated alloys shifted to the noble direction with the increase of Zn content accompanying with an increase of cathodic current density. The T4-treatment caused the negative shift of E_{corr} in average accompanying the decrease of cathodic current density. These facts demonstrated that the E_{corr} was dominated by the magnitude of cathodic reaction.

The corrosion current densities (I_{corr}) at E_{corr} were estimated by the extrapolation of the cathodic polarization curves. Apparently, the I_{corr} of the as-cast alloys increased with an increase in the Zn content and the I_{corr} of the T4-treated alloys were relatively lower than those of the as-cast alloys. The results of the polarization tests suggested that the corrosion resistance of the Mg-1Zn alloy was highest and that of the Mg-7Zn alloy was the lowest between the as-cast alloys. After the T4 treatment, the corrosion resistance of Mg-Zn alloys was improved and did not depend on the Zn content under 5 wt%. These findings are in good agreement with the immersion test results.

The anodic current density curves of all the samples showed a quasi-passive region followed by an abrupt increase in current density. The existence of quasi-passive region indicated the corrosion protection ability of the calcium phosphate layer deposited on the surface of samples during the preliminary immersion for 1.8 ks in Hanks' solution. Meanwhile, the abrupt increase in current density referred to the breakdown of the calcium phosphate layer

and the occurrence of stable localized corrosion. As shown in Fig. 2.10(a), the quasi-passive current density of the as-cast alloys decreased with the Zn addition, implying that the corrosion protectiveness of the calcium phosphate layer increased as the Zn content increased. The breakdown potential of the calcium phosphate layer was detected at -1.41, -1.43, -1.38 and -1.36 V (vs. Ag/AgCl) for the samples A1, A2, A3 and A4, respectively. This result suggested that the breakdown resistance of the calcium phosphate layer was the highest on the sample A4, then, decreased on the samples with reducing Zn content.

Although the corrosion protectiveness and breakdown resistance were the highest, the sample A4 showed the breakdown immediately after the initiation of polarization, while the sample A1 showed the widest quasi-passive region. It was indicated that the stable localized corrosion on the as-cast Mg-7Zn alloy occurred more easily than that on the as-cast Mg-1Zn alloy. These results can be explained by the deposition mechanism of calcium phosphates and the microstructure of the as-cast alloys. The calcium phosphate deposition was initiated by the pH increase due to the Mg corrosion [29–32]. As for the as-cast alloys, the Zn-rich phases of the as-cast alloys showed a uniform network, and the density of the network increased with the increase of Zn content. This microstructure indicated that the corrosion initiated almost uniformly on the as-cast alloys and allowed a relatively uniform calcium phosphate deposition. The cathodic current density of the as-cast alloys increased with an increase of Zn content, which indicated the enhancement of calcium phosphate deposition to form a thick deposition layer. Thus, the corrosion protectiveness and breakdown potential of the as-cast alloy increased with an increase of Zn content. In the case of the as-cast Mg-7Zn alloy, the subsequent corrosion progress was severer than the other as-cast alloys due to the larger eutectic cells, which caused many defects of the calcium phosphate layer around the eutectic cells. On the T4-treated alloys, the breakdown potential did not depend on the Zn content significantly, whereas that of the T4-treated Mg-7Zn alloy was slightly lower than those of the other alloys. The breakdown of the calcium phosphate layer on the sample $A4_T$ occurred at the boundary between eutectic cell and Mg matrix.

2.3.5 Impedance behavior

The Bode plots of the samples after 0, 0.5, 1, 2, 4 and 6 h of exposure in Hanks' solution are shown in Figure 2.11. The phase shift curves at 0 h showed a peak around 200 Hz and the curves at 0.5-6 h showed two peaks around 5000 Hz and 200 Hz, indicating that there was a time constant at 0 h and the second time constant appeared after 0.5 h. The appearance of the

peak around 5000 Hz after 0.5 h of immersion corresponded to the deposition of a calcium phosphate layer in Hanks' solution. The impedance and phase shift spectra of the as-cast alloys exhibited plenty of fluctuations in the low frequency range (10^0 Hz to 10^{-2} Hz) which were caused by the filiform corrosion as observed on the surfaces after the static immersion (Fig. 2.5). The magnitude and number of the fluctuations increased with the increase in Zn content. This result was associated with the increase of (α-Mg + MgZn) eutectic cells which caused the localized corrosion of the as-cast alloys. After the T4 treatment, both magnitude and number of the fluctuations significantly reduced, which was resulted from the dissolution of (α-Mg + MgZn) eutectic cells.

The polarization resistance which corresponds to the corrosion resistance is generally obtained as a difference in impedance values between 10^{-2} Hz and 10^5 Hz. Because the impedance value at 10^5 Hz did not depend on the difference of the alloys, the impedance value at 10^{-2} Hz (Z_{low}) was used to evaluate the corrosion resistance of the alloys with time. The Z_{low} is plotted as a function of immersion time in Figure 2.12. In case of the as-cast alloys, the Z_{low} of all the samples increased in the initial stage, and then decreased or fluctuated. The initial increase of the Z_{low} was attributed to the deposition of calcium phosphate on the surface of the samples in Hanks' solution and the decrease of the Z_{low} was explained by the initiation and growth of the filiform corrosion.

The Z_{low} of the sample A1 increased in the initial 2 h then became almost constant around 7×10^4 Ωcm^2 at 4 h. The Z_{low} of the samples A2 and A3 increased in the initial 1 h, and subsequently decreased in the next 1 h and remained unchanged around 3×10^4 and 4×10^3 Ωcm^2, respectively. The sample A4 showed a slight increase of the Z_{low} in the initial 0.5 h followed by a deterioration and restoration tendency. The highest and stabilized Z_{low} value (7×10^4 Ωcm^2) demonstrated the highest corrosion resistance of the sample A1 between the as-cast samples. The stabilized Z_{low} values of the samples A2 and A3 were 3×10^4 and 4×10^3 Ωcm^2, respectively. The deterioration and restoration tendency of the sample A4 demonstrated the unstable corrosion resistance due to the severe filiform corrosion. The time to the Z_{low} decrease depended on the Zn content and the decrease of Z_{low} occurred earlier with the increase of Zn content. It was demonstrated that the corrosion resistance of the as-cast Mg-Zn alloys decreased noticeably with increasing Zn content from 1 wt% to 7 wt%.

As for the T4-treated alloys, the impedance spectra showed less fluctuation than those of the as-cast alloys. The Z_{low} values of the T4-treated alloys at 0 h were higher than those of the as-cast alloys on average, demonstrating the effect of the disappearance of the eutectic cells.

The Z_{low} of the samples $A1_T$ and $A2_T$ increased in the initial 0.5 h and 1 h and became almost constant around 8×10^4 Ωcm^2 and 9×10^4 Ωcm^2, respectively. These results proved that the calcium phosphate layers on the samples $A1_T$ and $A2_T$ were stable and had high corrosion protectiveness. The Z_{low} of the sample $A3_T$ increased to 3×10^4 Ωcm^2 from 0 h to 0.5 h, decreased to 3×10^2 Ωcm^2 at 1 h, and then restored to around 4×10^4 Ωcm^2. The sample $A4_T$ showed a considerable drop of the Z_{low} value to 7×10^1 Ωcm^2 in the initial 0.5 h, followed by a recovery trend to around 10^4 Ωcm^2 until 6 h. This phenomenon could be explained by the rapid initiation of micro-galvanic corrosion between eutectic cells and α-Mg matrix and the slow deposition of calcium phosphate to cover the large-size (α-Mg + MgZn) eutectic cells in the sample $A4_T$. After the calcium phosphate could cover the whole surface, the Z_{low} value increased. The Z_{low} values of the T4-treated samples were higher than those of as-cast samples, which demonstrated the corrosion resistance of Mg-Zn alloys with up to 7 wt% Zn was improved by the T4 heat treatment.

For a more quantitative analysis using an equivalent electric circuit, the EIS results at 0.5 h of immersion in Hanks' solution were used. The result at 1 h was used for the A4T sample because the EIS plots at 0.5 h had a magnitude of fluctuation probably due to ongoing localized corrosion. The Nyquist and Bode plots of the samples are shown in Figure 2.13(a) and (b), respectively. The Nyquist plots showed a deformed semicircle that looked like two semicircles overlapping and an induction loop, and the Bode plots suggested the existence of two time constants in Fig. 2.11. The immersion test in Hanks' solution revealed the formation of the calcium phosphate layer in Fig. 2.7. Based on these facts and the previous works [15,33], the equivalent electric circuit shown in Fig. 2.13(c) was assumed.

In this study, R_s represents the solution resistance, and R_{ct} and CPE_{dl} represents the charge transfer resistance and the constant phase element of electric double layer, respectively. The constant phase element was used instead of the capacitance due to the non-homogeneity of the system. R_f and C_f represent the resistance and capacity of the calcium phosphate layer, respectively. R_L and L represent the resistance and inductance of the inductive loop. Then, the polarization resistance R_p was estimated using equation (2.5) by [33]:

$$\frac{1}{R_p} = \frac{1}{R_{ct}+R_f} + \frac{1}{R_L} \tag{2.5}$$

Using the equivalent circuit shown in Fig. 2.13(c), curve fitting was performed and the fitted curves are shown in Fig. 2.13(a) and (b). The calculated values of the parameters are listed in Table 2.5. One can be seen that, the R_{ct} values decreased with increasing Zn content, indicating the acceleration of corrosion of the substrate alloys. The R_f values characterized the corrosion protectiveness of deposited calcium phosphate layer. The decrease in R_f values with Zn content was attributed to the increase of defects of the calcium phosphate layer, which presumably occurred due to the localized corrosion around the eutectic cells. It should be noted that the R_f value of the samples A3, A4 and $A4_T$ was significantly low compared to the other samples, being attributed to the relatively high volume of eutectic cells in these samples.

The relation of R_p with Zn content and volume fraction of eutectic cell is shown in Figure 2.14. The R_p of the as-cast alloys decreased with an increase of Zn content, i.e. volume fraction of eutectic cell, linearly. This tendency is consistent to that of Mg ion release in Hanks' solution shown in Fig. 2.9. The R_p of the T4-treated alloys was 2-10 times higher that of the as-cast alloys in the Zn content range up to 5 wt%, demonstrating that the dissolution of Zn in matrix by T4 treatment improved the corrosion resistance. The R_p of the T4-treated alloys decreased linearly with an increase of Zn content up to 5 wt%. However, the decrease in R_p between 5 wt% and 7 wt% was discontinuous, which was attributed to the precipitation of Zn-rich phases in the $A4_T$ alloy. The R_p of the $A4_T$ alloy was equivalent to that of the A2 and A3 alloys, and the volume fraction of eutectic cell of the $A4_T$ alloy was 1.73 vol% which was equivalent to 0.99 and 2.18 vol% of the A2 and A3 alloys (Table 2.4). The Zn solubility limit of Mg is 6.2 wt% [18], that was between 5 wt% and 7 wt%. Therefore, it is suggested that the optimal Zn content for the corrosion resistance of binary Mg-Zn alloy is below the Zn solubility limit, because the precipitation of Zn-rich phase can be prevented below the solubility limit. So far, various optimal Zn contents were suggested, that was because the precipitation volume and size of Zn-rich phase varied depending on the casting and subsequent heat treatment conditions.

2.3.6 Corrosion mechanism of Mg-Zn alloys in Hanks' solution

According to the results, the corrosion resistance of the as-cast Mg-Zn alloys in Hanks' solution decreased when the Zn content increased from 1 wt% to 7 wt%, and the corrosion resistance was improved by the T4 heat treatment. In both the as-cast and T4-treated alloys, the addition of 7 wt% Zn excessed the maximum solubility of 6.2 wt% Zn in α-Mg, led to the formation of a high-volume fraction of (α-Mg + MgZn) eutectic cells and Zn-segregated regions, causing severe corrosion in these samples. On the contrary, the relatively high corrosion

resistance of the low Zn-content (Mg-1Zn) alloy is attributed to the following two aspects: (i) the low volume fraction of Zn-rich phases and (ii) the uniform deposition of calcium phosphate. The highest corrosion resistance of Mg-1Zn alloy in the current study agrees to Song et al. and Kubasek et al. [15,16] but it is in contradictory to Cai et al. and Koç et al. [10,11].

The disagreement in the optimal Zn content of Mg-Zn alloys among these studies could be due to the differences in the testing solution. The difference in impurity content of the alloys between these studies could cause the difference in corrosion rate because a trace amount of Fe and Ni drastically increase the corrosion rate of Mg [34]. Further investigation is necessary to understand the effect of impurity content on the optimal Zn content for the corrosion resistance of Mg-Zn binary alloys. Cai et al. and Koç et al reported the highest corrosion resistance of 5 wt% Zn and 3 wt% Zn alloys in a simulated body fluid (SBF), respectively. The Ca ion concentration of SBF is higher than that of Hanks' solution; therefore, the calcium phosphate deposition rate in SBF is expected to be higher than that in Hanks' solution. In addition, the initial corrosion of relatively high Zn content alloys was more rapid than that of low Zn content alloys, leading to the more rapid and larger amount of calcium phosphate deposition. Thus, the high amount and uniform deposition of calcium phosphate presumably dominates and contributes to the high corrosion resistance of the relatively high Zn-content alloy in SBF solution. It should be also noted that Cai et al. and Koç et al. reported the excessive addition of Zn content over 5 wt% and 3 wt%, respectively, would decrease the corrosion resistance of Mg-Zn alloys due to the acceleration of micro-galvanic corrosion.

Song et al. and Kubasek et al. reported the highest corrosion resistance of 2 wt% Zn and 1 wt% Zn alloys in NaCl solution, respectively. In NaCl solution, corrosion product which can show corrosion protectiveness like calcium phosphate does not deposit on the alloy surface. Then, the micro-galvanic corrosion between Zn-rich phases and Mg matrix presumably dominates the corrosion resistance of Mg-Zn alloys. Thus, the relatively low Zn-content alloy can show high corrosion resistance.

Based on the aforementioned discussion, the corrosion mechanisms of the as-cast Mg-1Zn, as-cast Mg-7Zn and T4-treated Mg-7Zn alloys in Hanks' solution are proposed to clarify the effect of volume fraction and distribution of Zn-rich phases to corrosion resistance of the alloys in Hanks' solution. The schematic illustrations are shown in Figure 2.15.

Generally, when a Mg-Zn alloy is exposed to Hanks' solution, the galvanic corrosion occurred with the following reactions:

Anodic reaction: $Mg \rightarrow Mg^{2+} + 2e^{-}$ (2.6)

Cathodic reaction: $H_2O + 2e^{-} \rightarrow H_2 + 2OH^{-}$ (2.7)

The Zn-rich phases including (α-Mg + MgZn) eutectic cells and Zn-segregated regions, acted as the micro-cathodes and the Mg matrix acted as the micro-anodes due to the difference in the standard corrosion potential. In the previous studies, Hiromoto et. al indicated that an increase in the surface pH initiates the deposition of calcium phosphate simultaneously with magnesium hydroxide. It was also suggested that the initial corrosion rate dominated the deposition mechanism of calcium phosphates [31,32]. The insoluble calcium phosphate layer acted as a barrier between the Hanks' solution and the alloy, then contributed to the corrosion behavior of Mg-Zn alloys.

In the as-cast Mg-Zn alloy, (α-Mg + MgZn) eutectic cells and Zn-segregated regions form a uniform network structure and the density of the network increases with increasing Zn addition. At the initial stage, the calcium phosphate uniformly deposits on the alloy surface and the deposition amount increases as increasing the density of the network structure. Consequently, the calcium phosphate layer on the Mg-1Zn alloy is relatively thinner than that on the Mg-7Zn alloy as shown in Fig. 2.15(a) and (c), respectively.

Because Hanks' solution can permeate through the hydrophilic calcium phosphate layer, the corrosion of Mg-Zn alloy gradually continues. The continuing corrosion of magnesium results in the growth of the initially deposited calcium phosphate. On the Mg-1Zn alloy, the calcium phosphate layer matures with few defects, thus, showing a relatively high corrosion protectiveness. However, the filiform corrosion slowly grows under the calcium phosphate layer (Fig. 2.15(b)). On the Mg-7Zn alloy, as a result of the galvanic reactions, the hydrogen (H_2) bubbles emit from the areas around the eutectic cells and cause the many defects on the calcium phosphate layer [32,35]. The further deposition of calcium phosphates is unable to seal the defects. Then, the filiform corrosion initiates and grows under the calcium phosphate layer. In addition, the micro-galvanic corrosion also propagates along the network structure into the interior of the alloy (Fig. 2.15(d)), which finally led to the corrosion morphology shown in Fig. 2.6(e).

On the T4-treated alloys, the initial corrosion rate was small due to the decrease of volume fraction of Zn-rich phases and the increase of Zn concentration in Mg matrix. So, the initial deposition rate of calcium phosphate on the T4-treated alloys was less than that on the

as-cast alloys. In case of the Mg-7Zn alloy, the (α-Mg + MgZn) eutectic cells are relatively large and the initial deposition of calcium phosphate is unable to cover the cells (Fig. 215(e)). As a result, the micro-galvanic corrosion takes place at the boundaries of the cells and the matrix. As the immersion time increases, the further deposition of calcium phosphate gradually covers the eutectic cells and simultaneously matures the initial deposition layer. In this alloy, the eutectic cells are discretely distributed and the network structure does not appear. Thus, the filiform corrosion spreading from the micro-galvanic corroded area only propagates on the surface (Fig. 2.15(f)).

This study suggests that the as-cast Mg-1Zn alloy and the T4-treated Mg-1, 3, 5Zn alloys are potential candidates for the use of biodegradable implant material due to their high corrosion resistance. The selection of suitable materials should be considered along with the mechanical properties.

2.4 Conclusions

The as-cast and T4-treated Mg-xZn alloys were prepared with different Zn content (x=1, 3, 5, 7 wt%). The effects of Zn content and T4 heat treatment on the microstructure and corrosion behavior of Mg-Zn alloys were studied.

(1) The addition of Zn (1 wt% to 7 wt%) resulted in the formation of the (α-Mg + MgZn) eutectic cells and Zn-segregated regions in the as-cast alloys. The Zn-rich phases formed a uniform network structure and the density of the network structure increased with Zn content. The T4 heat treatment decreased the volume fraction of the Zn-rich phases and these phases did not appear in the alloys with Zn content under 5 wt%. The (α-Mg + MgZn) eutectic cells were melted and re-solidified in the Mg-7Zn alloy, and its volume fraction decreased to 1.73 vol% from 2.87 vol% in the as-cast alloy.

(2) The corrosion resistance of the as-cast Mg-Zn alloys decreased with increasing Zn content from 1 wt% to 7 wt%. The as-cast Mg-1Zn alloy showed 2-, 4- and 10-times lower corrosion rate than the as-cast Mg-3Zn, Mg-5Zn and Mg-7Zn alloy in Hanks' solution, respectively. This result was attributed to the increase of the volume fraction of the Zn-rich phases acted as the micro-cathodes in the galvanic corrosion. The T4-treated alloys without and with lower volume fraction of Zn-rich phases showed the higher corrosion resistance than the as-cast alloys. As the result, the Zn content range which can provide relatively high corrosion resistance was widened to 1-5 wt% after

the T4 treatment. Consequently, the volume fraction of Zn-rich phases governed the corrosion resistance of Mg-Zn alloys more dominantly than the Zn content.

(3) The corrosion products of Mg-Zn alloys in Hanks' solution were mainly magnesium hydroxide and calcium phosphate. It was suggested that the deposition amount and uniformity of calcium phosphate layers played an important role in the corrosion resistance of the Mg-Zn alloys.

2.5 References

[1] M.P. Staiger, A.M. Pietak, J. Huadmai, G. Dias, Magnesium and its alloys as orthopedic biomaterials: A review, Biomaterials. 27 (2006) 1728–1734. https://doi.org/10.1016/j.biomaterials.2005.10.003.

[2] S. Agarwal, J. Curtin, B. Duffy, S. Jaiswal, Biodegradable magnesium alloys for orthopaedic applications: A review on corrosion, biocompatibility and surface modifications, Mater. Sci. Eng. C. 68 (2016) 948–963. https://doi.org/10.1016/j.msec.2016.06.020.

[3] G. Eddy Jai Poinern, S. Brundavanam, D. Fawcett, Biomedical Magnesium Alloys: A Review of Material Properties, Surface Modifications and Potential as a Biodegradable Orthopaedic Implant, Am. J. Biomed. Eng. 2 (2013) 218–240. https://doi.org/10.5923/j.ajbe.20120206.02.

[4] G. Song, S. Song, A possible biodegradable magnesium implant material, Adv. Eng. Mater. 9 (2007) 298–302. https://doi.org/10.1002/adem.200600252.

[5] G. Song, A. Atrens, Understanding magnesium corrosion. A framework for improved alloy performance, Adv. Eng. Mater. 5 (2003) 837–858. https://doi.org/10.1002/adem.200310405.

[6] L. Tan, X. Yu, P. Wan, K. Yang, Biodegradable Materials for Bone Repairs: A Review, J. Mater. Sci. Technol. 29 (2013) 503–513. https://doi.org/10.1016/j.jmst.2013.03.002.

[7] F. Feyerabend, J. Fischer, J. Holtz, F. Witte, R. Willumeit, H. Drücker, C. Vogt, N. Hort, Evaluation of short-term effects of rare earth and other elements used in magnesium alloys on primary cells and cell lines, Acta Biomater. 6 (2010) 1834–1842. https://doi.org/10.1016/j.actbio.2009.09.024.

[8] S.S. Abd El-Rahman, Neuropathology of aluminum toxicity in rats (glutamate and GABA impairment), Pharmacol. Res. 47 (2003) 189–194. https://doi.org/10.1016/S1043-6618(02)00336-5.

[9] C.H. Ku, D.P. Pioletti, M. Browne, P.J. Gregson, Effect of different Ti-6Al-4V surface treatments on osteoblasts behaviour, Biomaterials. 23 (2002) 1447–1454. https://doi.org/10.1016/S0142-9612(01)00266-6.

[10] S. Cai, T. Lei, N. Li, F. Feng, Effects of Zn on microstructure, mechanical properties

and corrosion behavior of Mg-Zn alloys, Mater. Sci. Eng. C. 32 (2012) 2570–2577. https://doi.org/10.1016/j.msec.2012.07.042.

[11] E. Koç, M.B. Kannan, M. Ünal, E. Candan, Influence of zinc on the microstructure, mechanical properties and in vitro corrosion behavior of magnesium-zinc binary alloys, J. Alloys Compd. 648 (2015) 291–296. https://doi.org/10.1016/j.jallcom.2015.06.227.

[12] Y. Yan, H. Cao, Y. Kang, K. Yu, T. Xiao, J. Luo, Y. Deng, H. Fang, H. Xiong, Y. Dai, Effects of Zn concentration and heat treatment on the microstructure, mechanical properties and corrosion behavior of as-extruded Mg-Zn alloys produced by powder metallurgy, J. Alloys Compd. 693 (2017) 1277–1289. https://doi.org/10.1016/j.jallcom.2016.10.017.

[13] N.Q. Cao, D.N. Pham, N. Kai, H. V. Dinh, S. Hiromoto, E. Kobayashi, In vitro corrosion properties of mg matrix in situ composites fabricated by spark plasma sintering, Metals (Basel). 7 (2017). https://doi.org/10.3390/met7090358.

[14] N.Q. Cao, H.M. Le, K.M. Pham, N. V Nguyen, S. Hiromoto, In Vitro Corrosion and Cell Response of Hydroxyapatite Coated Mg Matrix in Situ Composites, Materials (Basel). 12 (2019) 3474.

[15] Y. Song, E.H. Han, D. Shan, C.D. Yim, B.S. You, The effect of Zn concentration on the corrosion behavior of Mg-xZn alloys, Corros. Sci. 65 (2012) 322–330. https://doi.org/10.1016/j.corsci.2012.08.037.

[16] J. Kubásek, D. Vojtěch, Structural characteristics and corrosion behavior of biodegradable Mg-Zn, Mg-Zn-Gd alloys, J. Mater. Sci. Mater. Med. 24 (2013) 1615–1626. https://doi.org/10.1007/s10856-013-4916-3.

[17] Y.F. Zheng, X.N. Gu, F. Witte, Biodegradable metals, Mater. Sci. Eng. R Reports. 77 (2014) 1–34. https://doi.org/10.1016/j.mser.2014.01.001.

[18] H. Okamoto, Comment on Mg-Zn (Magnesium-Zinc), J. Phase Equilibria. 16 (1995) 474–475. https://doi.org/10.1007/BF02645363.

[19] X. Bin Liu, D.Y. Shan, Y.W. Song, E.H. Han, Effects of heat treatment on corrosion behaviors of Mg-3Zn magnesium alloy, Trans. Nonferrous Met. Soc. China (English Ed. 20 (2010) 1345–1350. https://doi.org/10.1016/S1003-6326(09)60302-2.

[20] Y. Song, E.H. Han, D. Shan, C.D. Yim, B.S. You, The role of second phases in the

corrosion behavior of Mg-5Zn alloy, Corros. Sci. 60 (2012) 238–245. https://doi.org/10.1016/j.corsci.2012.03.030.

[21] H.R. Bakhsheshi-Rad, E. Hamzah, M. Medraj, M.H. Idris, A.F. Lotfabadi, M. Daroonparvar, M.A.M. Yajid, Effect of heat treatment on the microstructure and corrosion behaviour of Mg-Zn alloys, Mater. Corros. 65 (2014) 999–1006. https://doi.org/10.1002/maco.201307492.

[22] H. Watanabe, H. Tanaka, Dual-wavelength spectrophotometric determination of magnesium (ii) with xylidyl blue I and nonionic surfactant, Bunseki Kagaku. 26 (1977) 635–639. https://doi.org/10.2116/bunsekikagaku.26.9_635.

[23] C.K. Mann, J.H. Yoe, Spectrophotometric determination of magnesium with sodium 1-azo-2-hydroxy-3-(2,4-dimethylcarboxanilido)-naphthalene-1′-(2-hydroxybenzene-5-sulfonate), Anal. Chem. 28 (1956) 202–205. https://doi.org/10.1021/ac60110a016.

[24] S. Hiromoto, A. Yamamoto, Control of degradation rate of bioabsorbable magnesium by anodization and steam treatment, Mater. Sci. Eng. C. 30 (2010) 1085–1093. https://doi.org/10.1016/j.msec.2010.06.001.

[25] F. Witte, F. Feyerabend, P. Maier, J. Fischer, M. Störmer, C. Blawert, W. Dietzel, N. Hort, Biodegradable magnesium-hydroxyapatite metal matrix composites, Biomaterials. 28 (2007) 2163–2174. https://doi.org/10.1016/j.biomaterials.2006.12.027.

[26] H. Kuwahara, Y. Al-Abdullat, N. Mazaki, S. Tsutsumi, T. Aizawa, Preparation of Magnesium Apatite on Pure Magnesium Surface during Immersing in Hank, Mater. Trans. 42 (2001) 1317 to 1321.

[27] G. Ben-Hamu, D. Eliezer, K.S. Shin, The role of Si and Ca on new wrought Mg-Zn-Mn based alloy, Mater. Sci. Eng. A. 447 (2007) 35–43. https://doi.org/10.1016/j.msea.2006.10.059.

[28] G. Song, A. Atrens, D. Stjohn, J. Nairn, Y. Li, The electrochemical corrosion of pure magnesium in 1N Nacl, Corros. Sci. 39 (1997) 855–875.

[29] M. Tomozawa, S. Hiromoto, Microstructure of hydroxyapatite- and octacalcium phosphate-coatings formed on magnesium by a hydrothermal treatment at various pH values, Acta Mater. 59 (2011) 355–363. https://doi.org/10.1016/j.actamat.2010.09.041.

[30] S. Hiromoto, M. Tomozawa, Corrosion behavior of magnesium with hydroxyapatite

coatings formed by hydrothermal treatment, Mater. Trans. 51 (2010) 2080–2087. https://doi.org/10.2320/matertrans.M2010192.

[31] M. Tomozawa, S. Hiromoto, Growth mechanism of hydroxyapatite-coatings formed on pure magnesium and corrosion behavior of the coated magnesium, Appl. Surf. Sci. 257 (2011) 8253–8257. https://doi.org/10.1016/j.apsusc.2011.04.087.

[32] S. Hiromoto, A. Yamamoto, High corrosion resistance of magnesium coated with hydroxyapatite directly synthesized in an aqueous solution, Electrochim. Acta. 54 (2009) 7085–7093. https://doi.org/10.1016/j.electacta.2009.07.033.

[33] A.D. King, N. Birbilis, J.R. Scully, Accurate Electrochemical Measurement of Magnesium Corrosion Rates; a Combined Impedance, Mass-Loss and Hydrogen Collection Study, Electrochim. Acta. 121 (2014) 394–406. https://doi.org/10.1016/j.electacta.2013.12.124.

[34] G.L. Song, A. Atrens, Corrosion mechanisms of magnesium alloys, Adv. Eng. Mater. 1 (1999) 11–33. https://doi.org/10.1002/(SICI)1527-2648(199909)1:1<11::AID-ADEM11>3.0.CO;2-N.

[35] G. Williams, H. Neil McMurray, Localized Corrosion of Magnesium in Chloride-Containing Electrolyte Studied by a Scanning Vibrating Electrode Technique, J. Electrochem. Soc. 155 (2008) C340. https://doi.org/10.1149/1.2918900.

Table 2.1 Chemical composition (wt%) of pure Mg and as-cast Mg-Zn alloys

Alloys name	Zn	Al	Cu	Ni	Fe	Ca	Si	Mn	Mg
Pure Mg	0.004	< 0.008	< 0.002	< 0.0009	< 0.003	< 0.004	< 0.022	< 0.024	≥ 99.93
Mg-1Zn	1.02								Bal.
Mg-3Zn	3.18								Bal.
Mg-5Zn	5.06								Bal.
Mg-7Zn	7.02								Bal.

Table 2.2 Composition and heat treatment condition of the samples

Sample name	Composition (wt%)	Preparation condition
A1	Mg-1%Zn	As-cast
A2	Mg-3%Zn	As-cast
A3	Mg-5%Zn	As-cast
A4	Mg-7%Zn	As-cast
$A1_T$	Mg-1%Zn	A1 + T4 heat treatment at 400 ^oC for 12 hours
$A2_T$	Mg-3%Zn	A2 + T4 heat treatment at 400 ^oC for 12 hours
$A3_T$	Mg-5%Zn	A3 + T4 heat treatment at 400 ^oC for 12 hours
$A4_T$	Mg-7%Zn	A4 + T4 heat treatment at 400 ^oC for 12 hours

Table 2.3 Components of Hanks' solution

Reagent	NaCl	KCl	$Na_2HPO_4.H_2O$	KH_2PO_4	$MgSO_4.7H_2O$	$NaHCO_3$	$CaCl_2$
Concentration (g/L)	8.00	0.40	0.06	0.06	0.20	0.35	0.14

Table 2.4 Volume fraction and average size of (α-Mg + MgZn) eutectic cell in the alloys

Sample name	Vol. fraction (%)	Average size (μm)
A1	0.07	0.52
A2	0.99	1.78
A3	2.18	1.81
A4	2.87	2.18
$A1_T$	-	-
$A2_T$	-	-
$A3_T$	-	-
$A4_T$	1.73	27.76

Table 2.5 Fitting results of the EIS spectra

	R_s ($\Omega \cdot cm^2$)	CPE_{dl}-T ($\mu F \cdot cm^{-2}$)	n	R_{ct} ($\Omega \cdot cm^2$)	C_f ($\mu F \cdot cm^{-2}$)	R_f ($\Omega \cdot cm^2$)	L ($\Omega \cdot s \cdot cm^2$)	R_L ($\Omega \cdot cm^2$)	R_P ($\Omega \cdot cm^2$)
A1	40.15	13.33	0.715	558.4	2.066	31666	1.059E6	1.065E5	2.47E4
A2	41.39	11.07	0.745	310.5	1.960	17242	8.039E5	23464	1.00E4
A3	31.79	14.10	0.670	284.9	2.817	3687	2916	4577	2.13E3
A4	58.79	13.51	0.675	249.8	1.735	2749	2205	1576	1.03E3
$A1_T$	38.83	12.46	0.729	423.1	2.084	53933	1.005E6	2.290E5	4.39E4
$A2_T$	51.91	11.00	0.714	407.8	2.445	35577	6.758E5	1.134E5	2.73E4
$A3_T$	51.54	13.71	0.672	347.3	2.538	35464	2.798E5	78028	2.45E4
$A4_T$	53.98	38.26	0.708	485.4	1.324	3062	815.5	19672	3.01E3

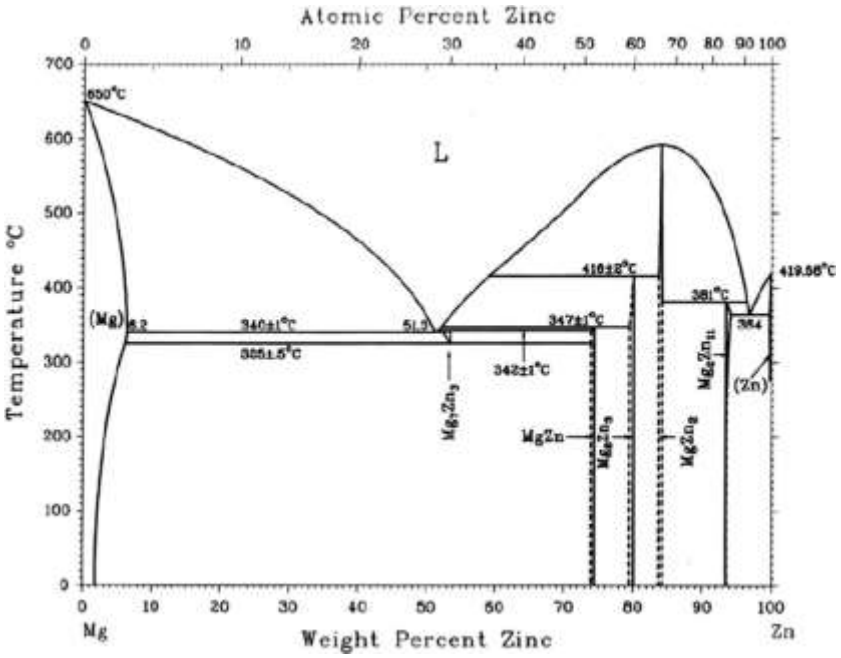

Figure 2.1 Phase diagram of Mg-Zn binary alloys

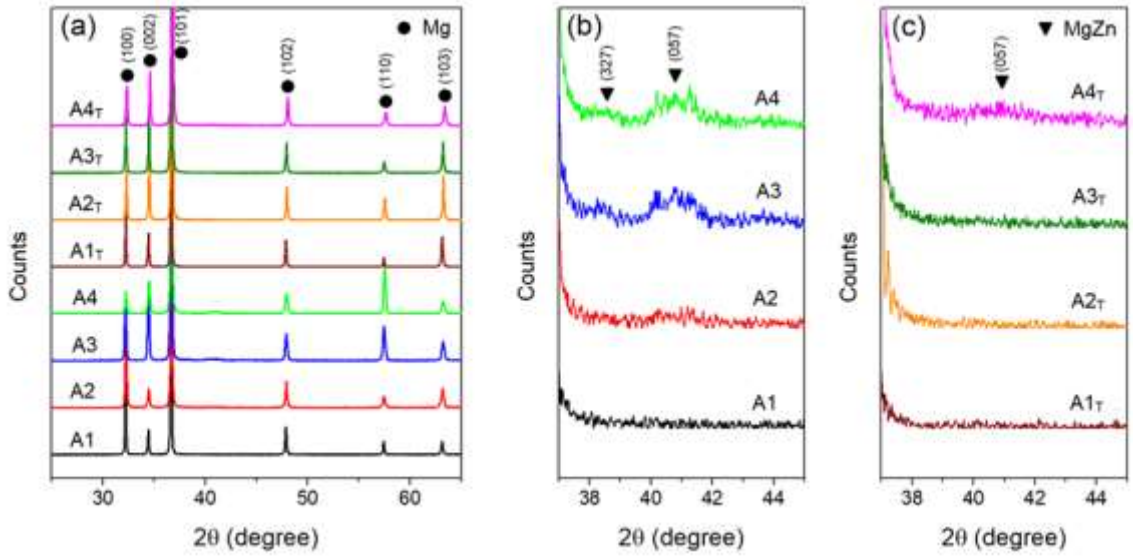

Figure 2.2 X-rays diffraction patterns of (a) all samples, scan range 25º – 65º; (b) as-cast samples and (c) T4-treated samples, scan range 37º – 45º

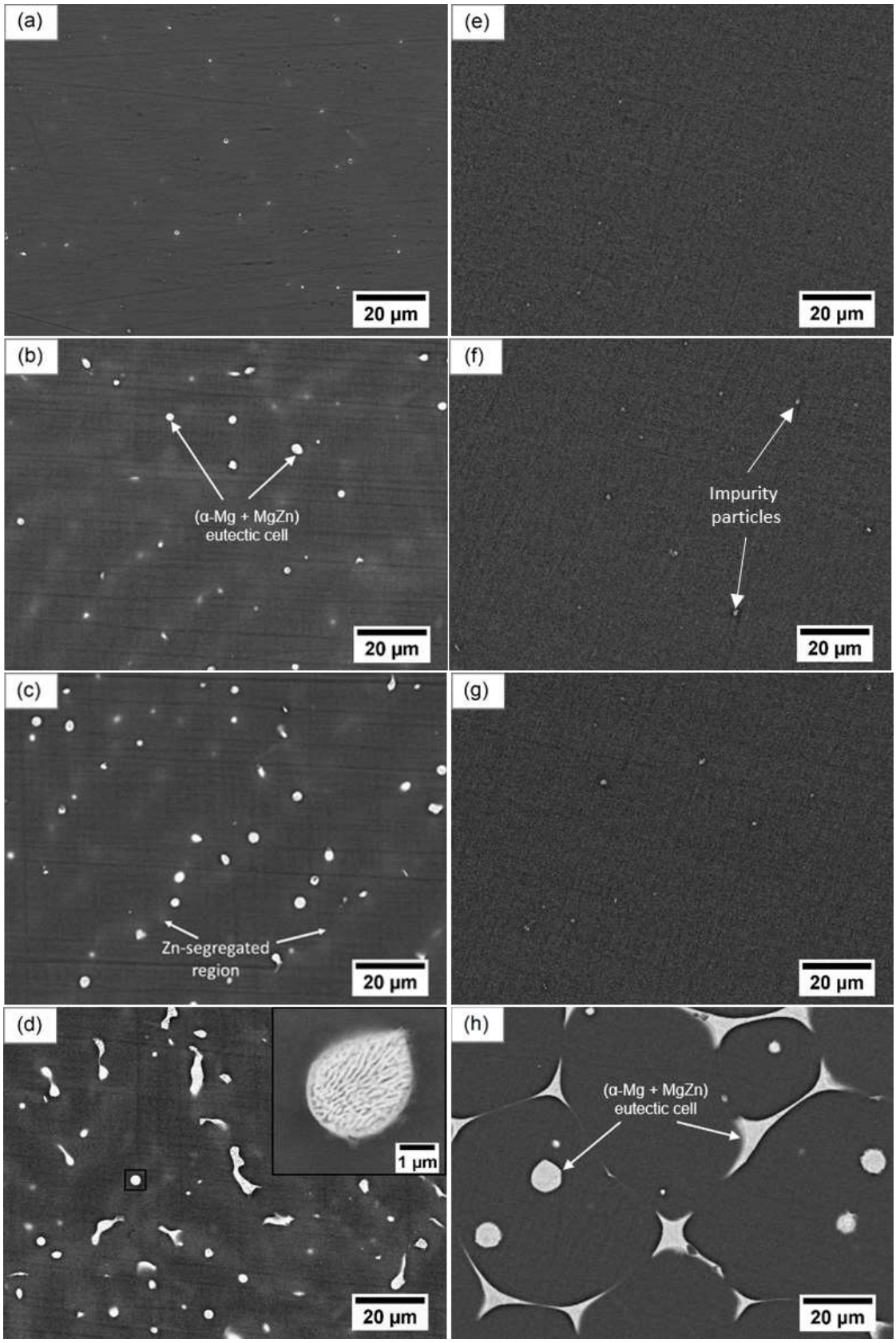

Figure 2.3 BSE images of the microstructure of various samples: (a) A1, (b) A2, (c) A3, (d) A4, (e) $A1_T$, (f) $A2_T$, (g) $A3_T$, and (h) $A4_T$. The inset in Fig. 3(d) is a magnified view of the area highlighted in the black square showing a (α-Mg + MgZn) eutectic cell

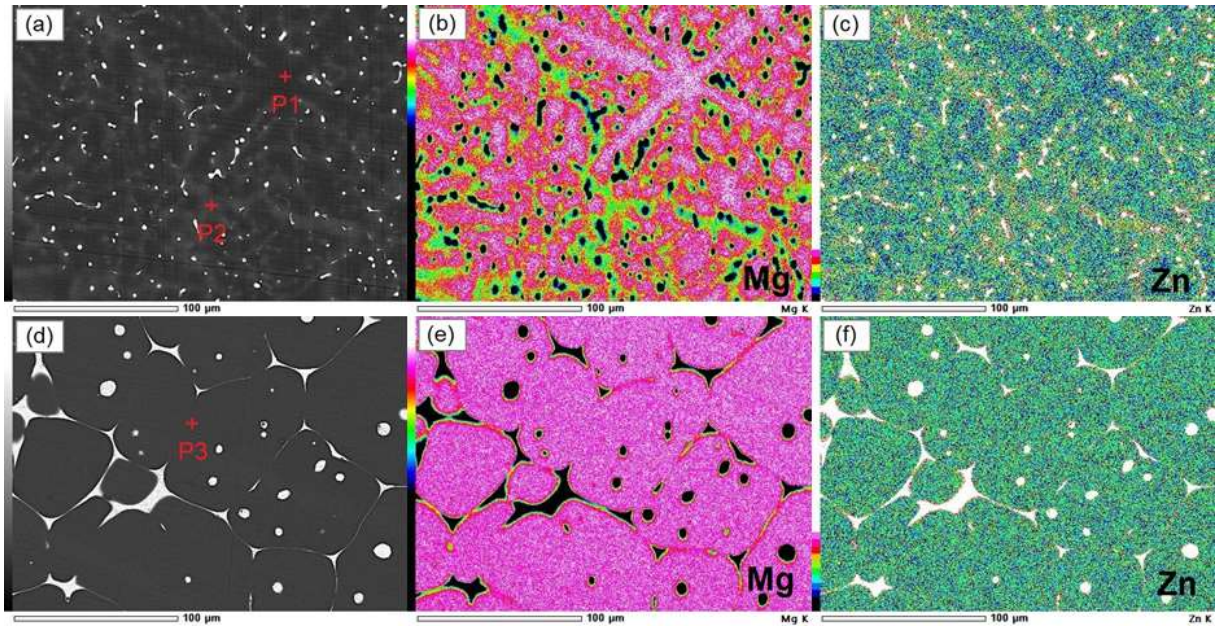

Figure 2.4 BSE image, EDS map of Mg element and Zn element, of (a-c) as-cast Mg-7Zn and (d-f) T4-treated Mg-7Zn alloys, respectively

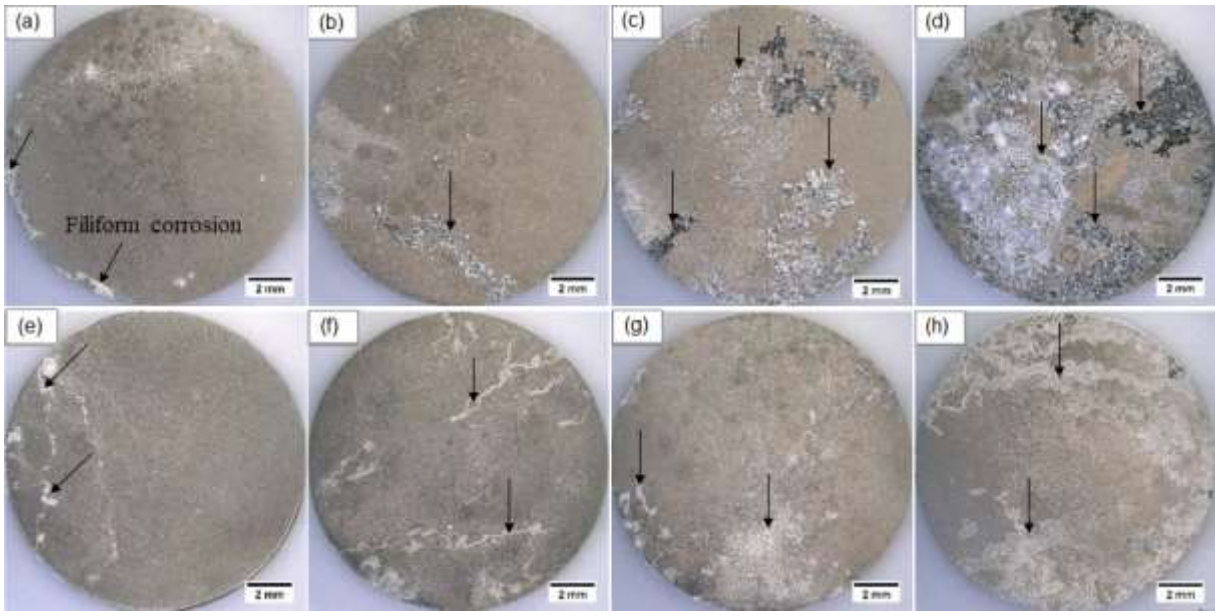

Figure 2.5 Optical surface images of samples after 14 days of immersion in Hank's solution. (a) A1, (b) A2, (c) A3, (d) A4, (e) $A1_T$, (f) $A2_T$, (g) $A3_T$, and (h) $A4_T$

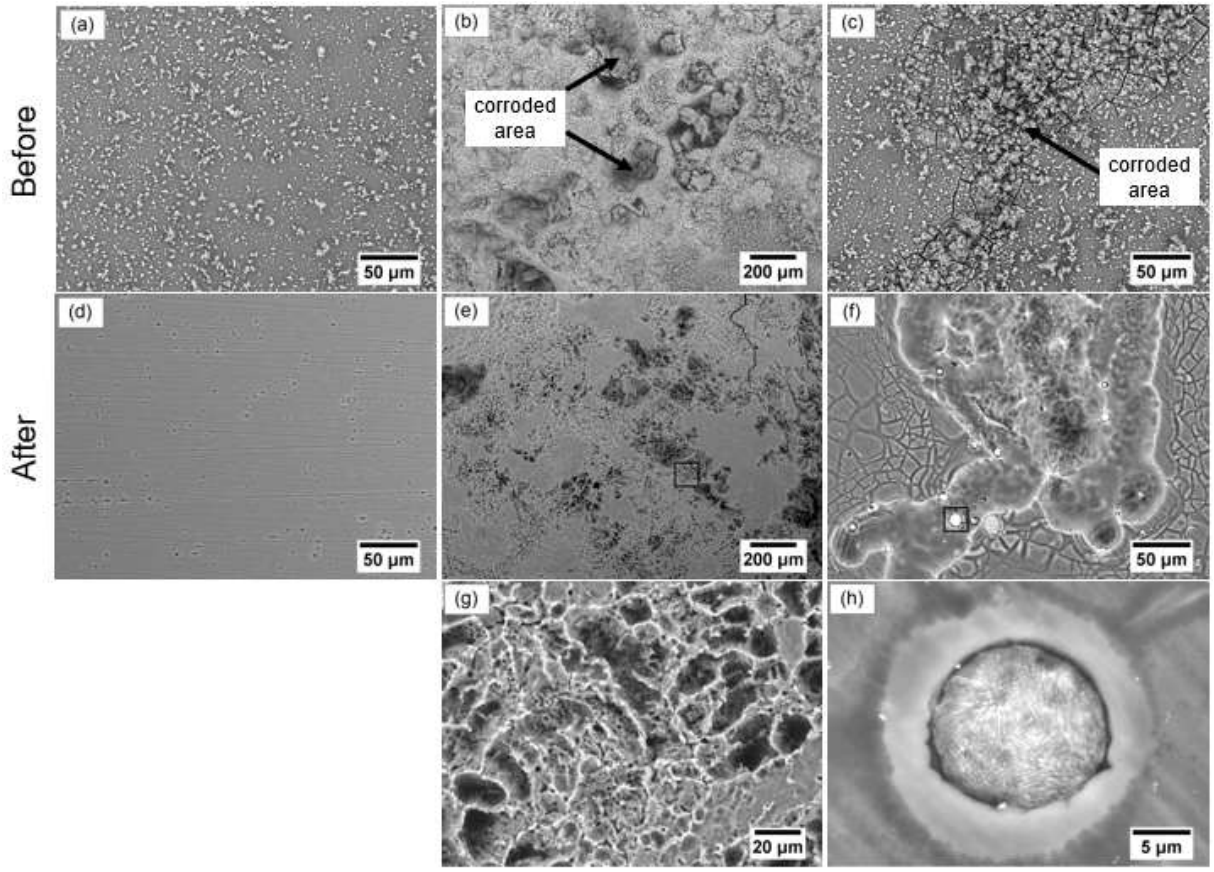

Figure 2.6 BSE images of the surface of samples before and after removing corrosion products. (a, d) A1, (b, e) A4 and (c, f) $A4_T$; (g) and (h) is magnified image of the area marked by black square in figure (e) and (f) respectively

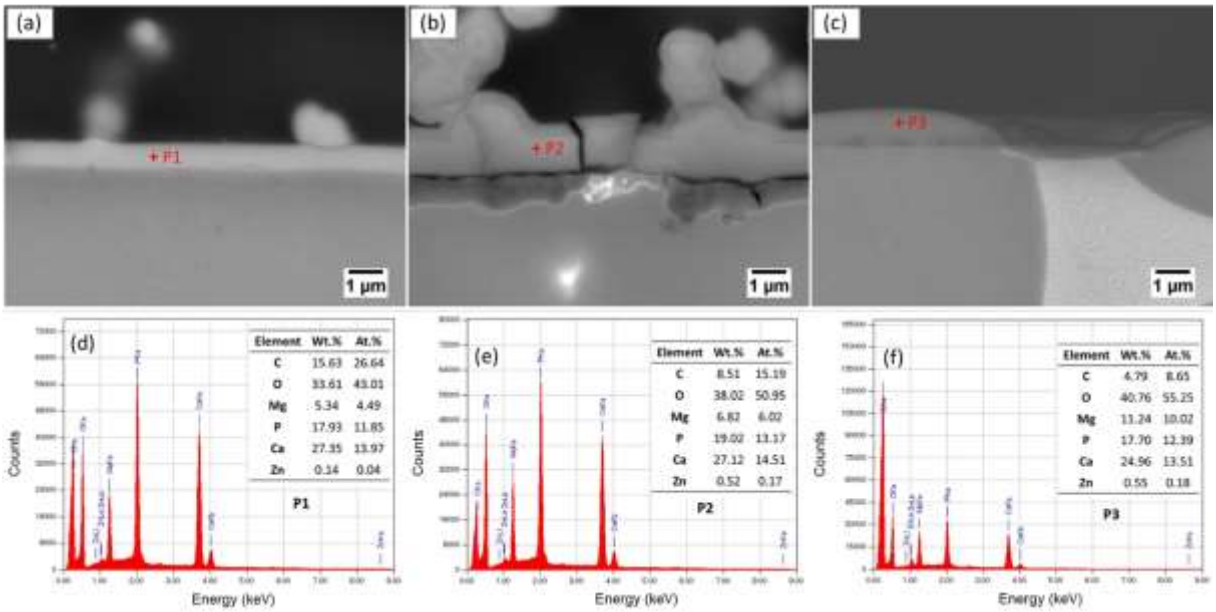

Figure 2.7 BSE cross-sectional images of the samples A1, A4 and $A4_T$ after immersion tests in Hanks' solution for 14 days (a) A1, (b) A4 and (c) $A4_T$. EDS results of the corrosion product layers at (d) point P1, (e) point P2 and (f) point P3

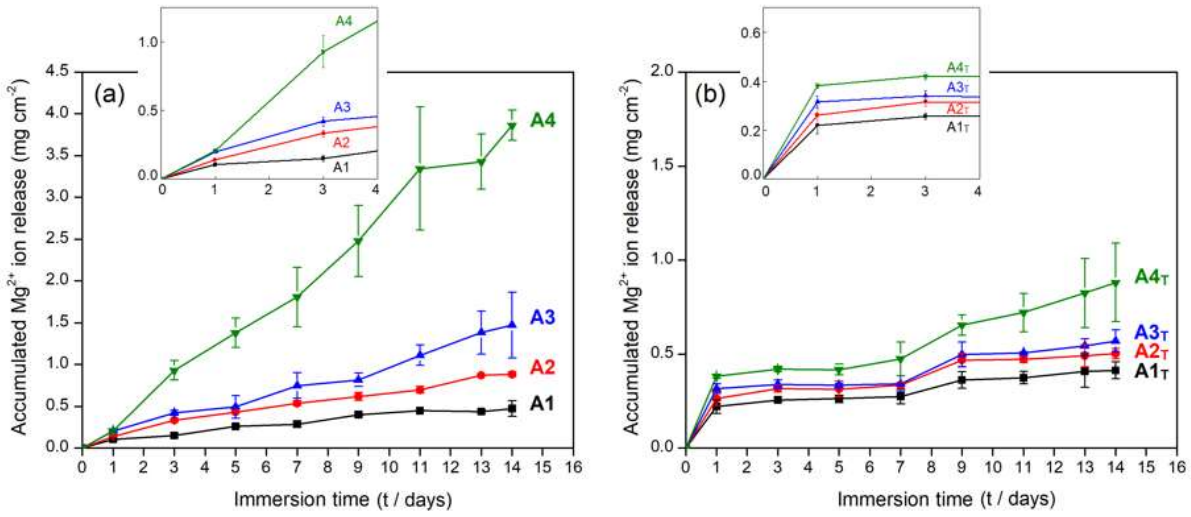

Figure 2.8 Mg^{2+} ions released of (a) as-cast samples and (b) T4-treated samples as a function of the immersion time in Hanks' solution

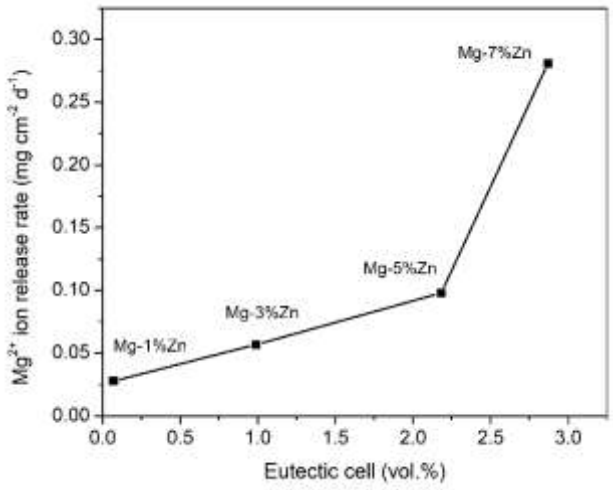

Figure 2.9 Average Mg^{2+} ion release rate of as-cast Mg-Zn alloys in Hanks' solution for 14 days

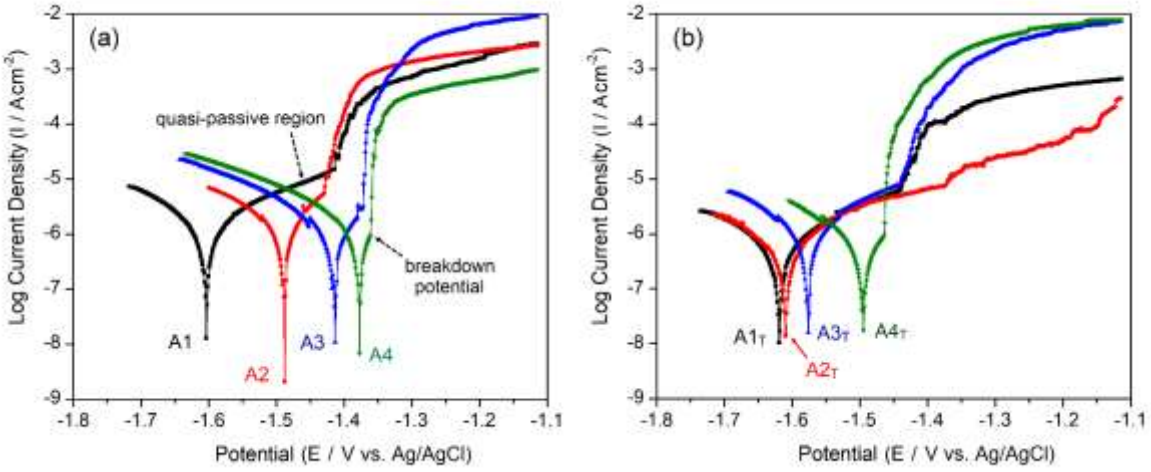

Figure 2.10 Anodic polarization curves of (a) as-cast samples and (b) T4-treated samples. All measurements were done in Hanks' solution

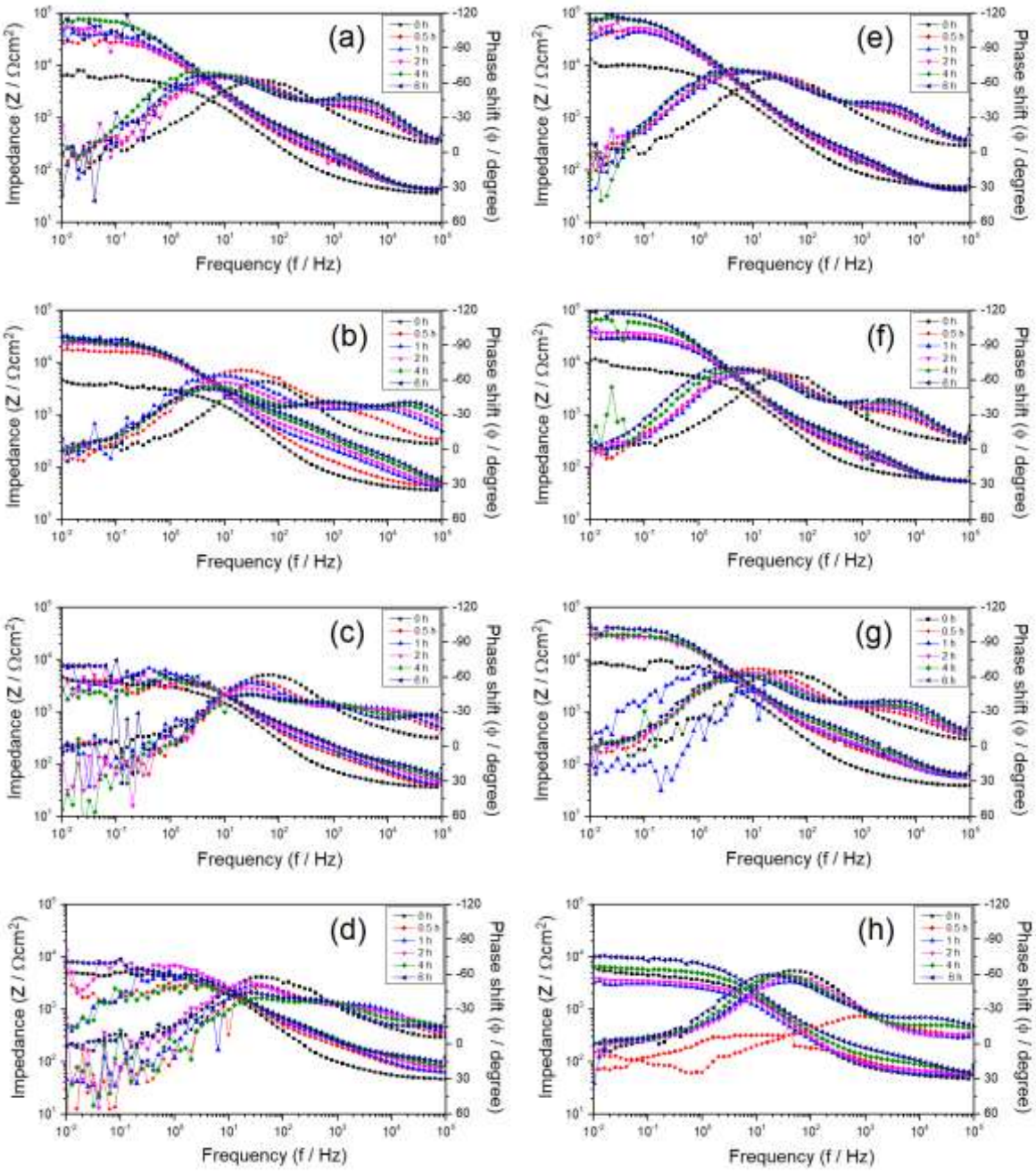

Figure 2.11 Bode plots of various samples. (a) A1, (b) A2, (c) A3, (d) A4, (e) $A1_T$, (f) $A2_T$, (g) $A3_T$, and (h) $A4_T$. All measurements were carried out in Hank's solution

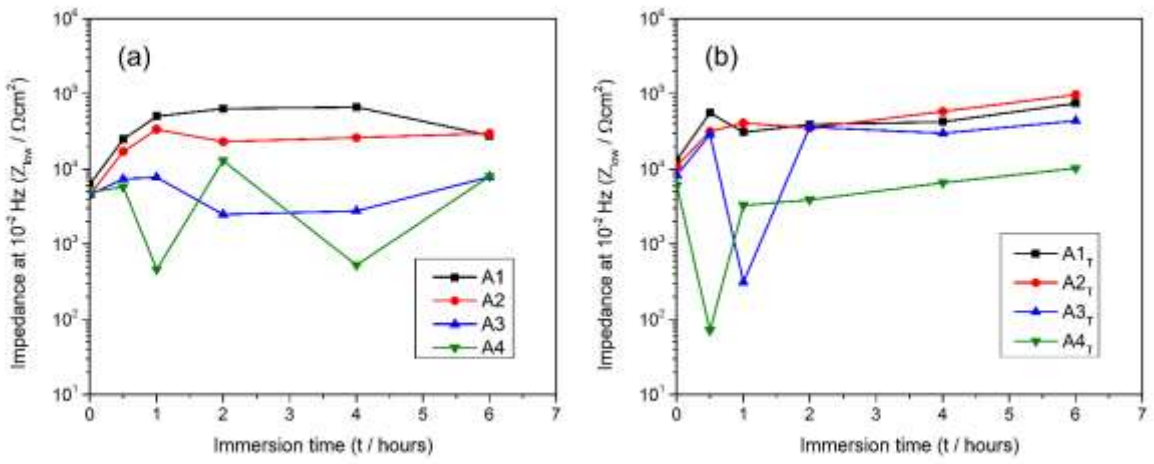

Figure 2.12 Time dependence of impedance at 10^{-2} Hz of (a) as-cast and (b) T4-treated alloys

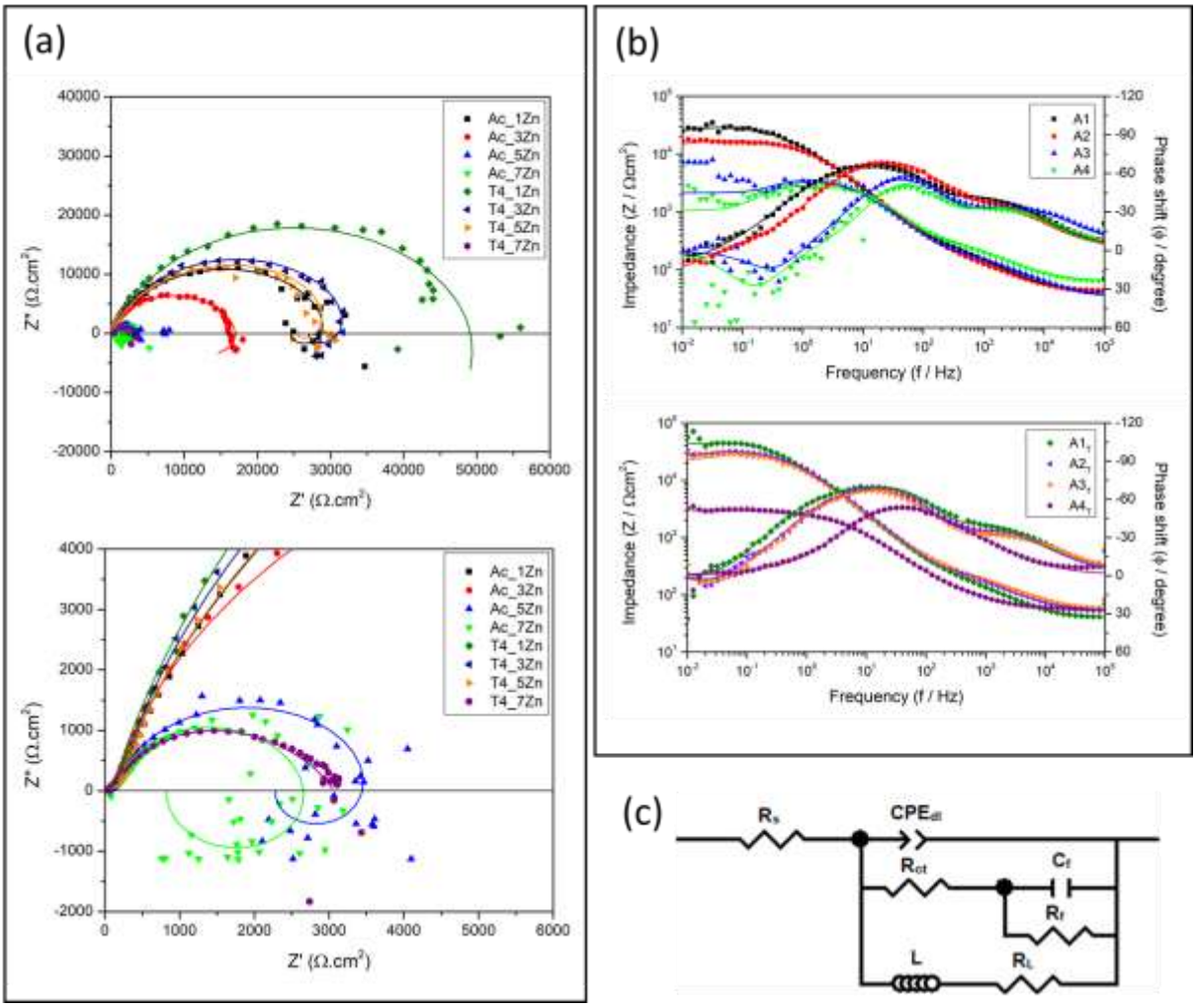

Figure 2.13 EIS measurement (scatter symbols) and model fit (solid lines) of the samples measured at 0.5 h after immersion, except for sample $A4_T$ measured at 1 h after immersion. (a) Nyquist plot, (b) Bode Z-plot and (c) equivalent circuit of EIS spectra

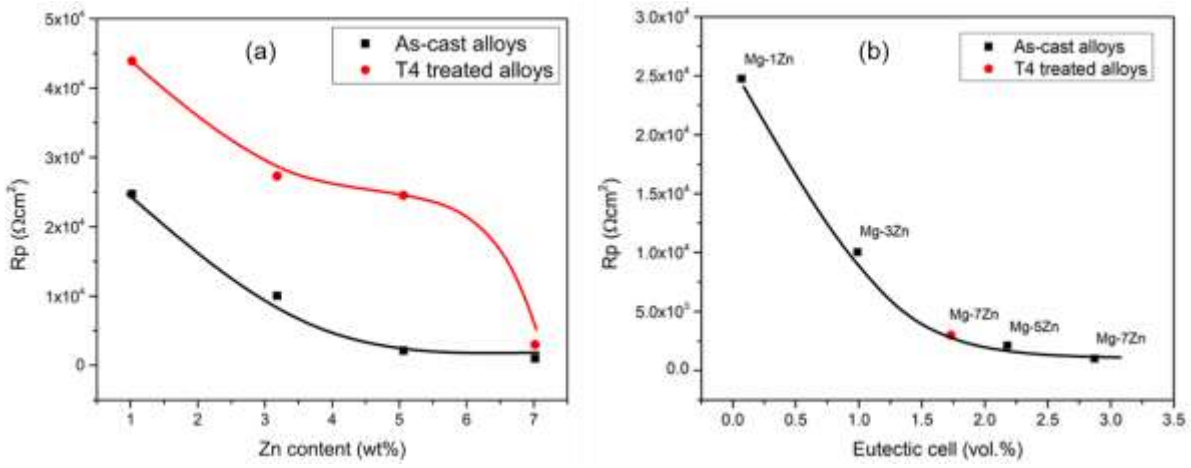

Figure 2.14 Relation of polarization resistance (R_p) with (a) Zn content and (b) volume fraction of eutectic cell of the alloys

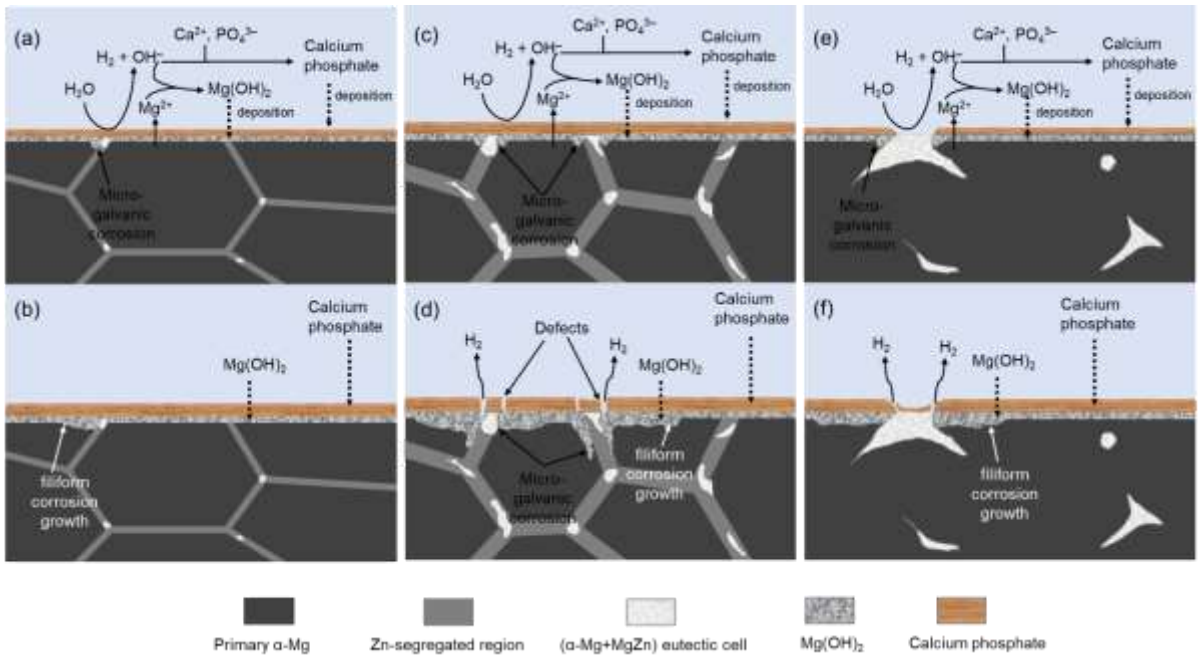

Figure 2.15 Schematic illustration of the corrosion mechanism of (a, b) as-cast Mg-1Zn, (c, d) as-cast Mg-7Zn and (e, f) T4-treated Mg-7Zn alloys in Hanks' solution

Chapter 3

Influences of Zn content and solution heat treatment on mechanical properties and mechanical integrity of Mg-Zn alloys in Hanks' solution

3.1 Introduction

Magnesium (Mg) and magnesium alloys possess great potentials as the biodegradable materials in the orthopedic implant applications. The main advantages of Mg over the conventional biomaterials are the biodegradability in the physiological environment and Young's modulus comparable to that of human bones [1–5]. Unlike the traditional implant materials, the biodegradability of Mg eliminates the need for a secondary surgical to remove the implant after the tissue healing. In another aspect, the similarity in Young's modulus between Mg and human bones relief the stress shielding effect which benefits the bone formation and increase the bone density [2,3].

Although the biodegradability is one of the main advantages of Mg, the very high degradation/corrosion rate in the physiological environment limits its practical applications [5–7]. The rapid corrosion of Mg deteriorates the mechanical integrity of implant before the tissue has sufficiently healed and releases large amount of hydrogen gas which forms a gas cavity and delays the tissue healing [8–11]. In the previous study, Zn was employed as alloying element for Mg binary alloys. The results demonstrated that the addition of 1 wt% Zn significantly enhanced the corrosion resistance of Mg. The increase of Zn content up to 7 wt% decreased the corrosion resistance of the binary alloys due to the formation of Zn-rich phases which promoted the micro-galvanic corrosion [12].

With consideration for the future applications, the biomedical implants require a sufficient mechanical strength to support the bone healing process for a certain period of time [3,13]. Generally, the degradation of materials substrate causes a loss of mechanical properties during the implantation. Therefore, in addition to considering the initial mechanical properties

of the biomedical implant materials, their mechanical integrity during service should also be carefully evaluated.

In the current work, the influence of Zn content and solution heat treatment on the mechanical properties of Mg-Zn binary alloys were investigated. The deterioration of mechanical integrity of Mg-Zn alloys during immersion in a physiological environment was studied.

3.2 Experimental procedure

3.2.1 Materials preparation

As-cast and solution heat treated (T4-treated) Mg-xZn (x = 1 wt%, 5 wt%, and 7 wt%) binary alloys were fabricated from high purity Mg ingots (> 99.9 wt%, Osaka Asahi Metal) and high purity Zn shots (> 99.99 wt%, Osaka Asahi Metal). The fabrication methods and heat treatment conditions for Mg-xZn alloys were described in details in the Chapter 2. The names and preparation conditions of the alloys were summarized in Table 3.1.

3.2.2 Microstructure observation

The samples for the microstructure observation were ground to 4000 grit SiC paper, then successively polished with 1 μm alumina paste and then etched by a Picral solution and by a Glycol acetic solution to reveal different microstructure characteristics. The Picral solution contained 4.2 g picric acid, 10 ml acetic acid, 10 ml distilled water and 70 ml ethanol, and the Glycol acetic solution contained 60 ml ethylene glycol, 20 ml acetic acid, 1 ml nitric acid and 20 ml distilled water. The etching time for Picral and Glycol acetic etching was 7-8 seconds and 12-15 seconds, respectively. The optical metallographic images were taken using optical microscope (OM, Olympus BX510). The equivalent diameter of the as-cast grains is calculated by the following equation:

$$N\pi(\frac{d}{2})^2 = S \tag{3.1}$$

where N is the number of grains and d is the equivalent diameter of the grain and S is the total area of the image.

3.2.3 Mechanical tests

Micro Vickers hardness of the Mg-Zn alloys was measured using a micro Vickers hardness tester (MMT-X3A, Matsuzawa). 7 measurements were conducted for each sample. The average value was calculated from 5 measurements by excluding maximum and minimum. The dwell time was 15 seconds. The test load was 0.245 N for the measurements at eutectic cell area in the T4-7Zn alloy and 0.49 N for the other measurements.

The samples for compression tests were machined from as-cast and T4-treated ingots by computer numerical control (CNC) machining to obtain cylindrical-shape with the dimensions of 7 mm in diameter and 12 mm in length. The compression tests were conducted using an autograph (AG-1 1000KN, Shimadzu). The cross-head speed was 0.2 mm/min. The 0.2% proof stress was calculated from the stress-strain curve of the samples.

3.2.4 Mechanical integrity tests

The cylindrical-shape samples tests were immersed in 120 ml Hanks' solution at 37 ºC. The chemical compositions of Hanks' solution are summarized in Table 3.2. The ratio of the total surface area of the sample to solution volume was about 40 ml/1 cm^2. Two to three samples of each alloys were used for each 1, 3, 7, 14 and 28 days of immersion period. After the prescribed immersion period, the samples were removed from testing solution and dried in air. The post-immersion compression tests were conducted to investigate the mechanical integrity of Mg-Zn alloys.

3.3 Results

3.3.1 Microstructure observation

Figure 3.1 shows the optical micrographs of the as-cast and T4-treated Mg-Zn alloys treated with Picral etching solution and Figure 3.2 shows the optical micrograph of the as-cast alloys treated with Glycerol acetic etching solution. The Picral etching solution and Glycol acetic etching solution were used simultaneously to reveal different characteristics of the microstructure.

Microstructural observation with Picral etching solution indicated that the addition of Zn as an alloying element significantly refined the grain size of the as-cast Mg-Zn alloys as shown in Fig. 3.1(a-c). The average grain size of the Ac-1Zn, Ac-5Zn and Ac-7Zn alloys was ca. 199 ± 29 μm, 89 ± 8 μm, 70 ± 6 μm, respectively.

Optical images obtained with Glycerol acetic etching solution showed that of the as-cast Mg-Zn alloys consisted of α-Mg matrix (bright contrast) and Zn-rich phases (dark contrast). The Zn-rich phases included (α-Mg + MgZn) eutectic cells and Zn-segregated as demonstrated in Chapter 2 [12]. The (α-Mg + MgZn) eutectic cells and Zn-segregated phase mainly precipitated along the grain boundaries and dendrite arms, forming a network-like structure as shown in Fig. 3.2(a-c).

The microstructure of the Mg-Zn alloys greatly changed after the T4 treatment. The average grain size of the alloys increased with the average grain size of the T4-1Zn, T4-5Zn and T4-7Zn alloys was 280 ± 16 μm, 236 ± 20 μm and 107 ± 7 μm as shown in Fig. 3.1(d-f), respectively. The Zn-rich phases were dissolved and not observed in the T4-1Zn and T4-5Zn alloys, while the T4-7Zn alloy showed large-size (α-Mg + MgZn) eutectic cells at the boundaries and within the grains. The optical images of the T4-treated alloys obtained with Glycol acetic were similar to those obtained with and Picral and were not shown here.

3.3.2 Mechanical properties of Mg-Zn alloys

Figure 3.3 shows the Micro-Vickers hardness of the as-cast and T4-treated alloys. Because the T4-treated alloy showed large-size (α-Mg + MgZn) eutectic cells in the microstructure, the micro-Vickers hardness test of the T4-7Zn alloy was conducted at both α-Mg grain and (α-Mg + MgZn) eutectic cell. The results indicated that the hardness of the as-cast alloys increased with increasing content of Zn and the T4-treated alloys showed higher hardness than the as-cast alloys. In the case of the T4-7Zn alloy, the (α-Mg + MgZn) eutectic cell showed much higher hardness than the α-Mg grain.

Figure 3.4 shows the stress-strain curves of the as-cast and T4-treated Mg-Zn alloys obtained by the compression tests. The mechanical properties of the Mg-Zn alloys are summarized in Table 3.3.

In the case of the as-cast alloys, the ultimate compressive strength (UCS) and 0.2% proof stress (PS) increased while the strain at failure (SF) decreased with Zn addition. The Ac-

7Zn alloy showed the highest UCS and PS of 404 MPa and 109 MPa, and the Ac-1Zn alloy exhibited the largest SF of 41.0% among the as-cast alloys, respectively. Both mechanical strength and strain at failure of the Mg-Zn alloys decreased after the T4 treatment. The UCS and PS of the T4-7Zn alloy were 388 MPa and 65 MPa, and the SF of the T4-1Zn alloy was to 32.4%, respectively.

3.3.3 Mechanical integrity of Mg-Zn alloys after immersion tests in Hanks' solution

Figure 3.5 shows the photographic images of the samples after immersion tests. In the current study, the Mg-Zn alloys were immersed in Hanks' solution for up to 28 days to examine the effect of corrosion to mechanical integrity. The materials and experimental setup of the immersion test were similar to those in the previous study in Chapter 2. The corrosion rate of Mg-Zn alloys in Hanks' solution was not directly measured but it was referenced from the immersion test in the previous study.

The surface appearance after immersion test indicated that the filiform corrosion dominantly occurred on the Mg-Zn alloys. The filiform corrosion was characterized by the appearance of worm-like filaments as can be seen in Figure 3.5. Filiform corrosion is a kind of superficial localized corrosion which develops rapidly to surrounding areas but slowly to the interior of substrate.

It can be seen that the filiform corrosion appeared in the as-cast and T4-treated Mg-5 and 7Zn alloys from Day 1 of immersion while the Ac-1Zn and T4-1Zn alloys only showed filiform corrosion morphology after 14 days of immersion. In all samples, the total areas of filiform corrosion damage increased with the immersion time. After 14 days, the surfaces of the Ac-5Zn and Ac-7Zn alloys were fully covered with filiform corrosion. The Ac-5Zn alloy after 28 days showed severe corrosion appearance as the Ac-7Zn alloy after 14 days. On the other hand, the surface of the T4-5Zn and T4-7Zn alloys were partly corroded after 28 days. Among all samples, the Ac-1Zn and T4-1Zn alloys exhibited the least corrosion damage. The results indicated that the Ac-1Zn and T4-1Zn alloys showed the high corrosion resistance while the Ac-5Zn and Ac-7Zn alloys showed the low corrosion resistance among the samples. This result was in good agreement with the results obtained from immersion tests in Chapter 2 [12].

Figure 3.6 shows the changes in the UCS and PF of the Mg-Zn alloys with immersion time in Hanks' solution. It can be seen that the UCS and PF of the Mg-Zn alloys decreased with the extension of immersion time excepts the Mg-1Zn alloys. In the case of the Ac-1Zn, T4-1Zn,

T4-5Zn and T4-7Zn alloys, the UCS and PF did not show an apparent decrease after 3 days of immersion, after which the UCS and PF declined slightly to Day 28. In the case of the Ac-5Zn and Ac-7Zn alloys, the UCS and PF dropped rapidly and immediately after immersion in Hanks' solution. The UCS and PF of the Ac-5Zn alloy slightly slowed down from Day 3, while those of the Ac-7Zn alloy exhibited a sharp and linear decrease from Day 0 to Day 28.

3.4 Discussion

3.4.1 Relationship between microstructures and mechanical properties of Mg-xZn binary alloys

As discussed previously in the Chapter 2, the addition of Zn in the Mg-Zn binary alloys resulted in the formation of Zn-rich phases including the (α-Mg + MgZn) eutectic cell and the Zn-segregated phase. The Zn-rich phases mainly precipitated along the grain boundaries and dendrite arms to form a network-like structure as shown in Fig. 3.2(a-c). During the T4 treatment, the Zn-rich phases in the Mg-1Zn and Mg-5Zn alloys were completely dissolved into the Mg matrix because the solubility of Zn in Mg was ca. 6 wt% at 400 ^{o}C [15]. In the case of the Mg-7Zn alloy after T4 treatment, the entire Zn-segregation phase and a part of the (α-Mg + MgZn) eutectic cell were dissolved in the matrix. Consequently, the volume fraction of (α-Mg + MgZn) eutectic cell of the Ac-1Zn, Ac-5Zn, Ac-7Zn and T4-7Zn alloys were ca. 0.07, 2.18, 2.99 and 1.87 vol%, respectively.

The grain refinement effect of Zn as an alloying element in Mg alloys has been widely reported [16,17]. In the as-cast Mg-Zn alloys, the addition of Zn from 1 wt% to 7 wt% reduced the crystal grain size from 199 μm to 70 μm. The increase in the UCS and PS for as-cast Mg-Zn alloys with increasing Zn content up to 7 wt% was thus attributed to the grain boundary strengthening according to the Hall-Petch relationship [18]. On the other hand, according to the Mg–Zn binary phase diagram [15], the maximum solubility of Zn in Mg at room temperature in the equilibrium state is ca. 1.6 wt%. In this study, although the equilibrium state was not reached due to the rapid solidification of Mg-Zn alloys by copper mold casting, Zn alloying element still dissolved into Mg matrix to some extent. The incorporation of Zn as soluble atoms in the Mg matrix produced a solid solution strengthening effect, which contributed to the high strength of as-cast Mg-Zn alloys [19,20]. In addition, the formation of (α-Mg + MgZn) eutectic cell contributed to the second phase strengthening effect [19,21]. The

increase in the volume fraction of (α-Mg + MgZn) eutectic cell promoted the mechanical strength of the as-cast Mg-Zn alloys.

After the T4 treatment, the network-like structure of Zn rich phases was dissolved in the Mg matrix. Consequently, the grain size and Zn solubility in the Mg matrix increased while the volume fraction of (α-Mg + MgZn) eutectic cell decreased. The decline in the UCS and PS of the Mg-Zn alloys after T4 treatment was therefore attributed to the decrease in the grain boundary strengthening and second phase strengthening. Although the solid solution strengthening effect increased due to the higher solubility of Zn in Mg, the decrease in mechanical strength suggested that the solid solution strengthening had less influence on the mechanical strength of Mg-Zn alloys than the two other factors. The UCS values of several Mg-Zn alloys plotted as a function of the volume fraction of (α-Mg + MgZn) eutectic cell is shown in Figure 3.7. It can be seen that the UCS of Mg-Zn alloys linearly increased with the amounts of (α-Mg + MgZn) eutectic cell. The linear relationship indicated that the mechanical strength of Mg-Zn alloys was significantly influenced by the volume fraction of (α-Mg + MgZn) eutectic cell.

In this study, the Ac-1Zn alloy showed the highest SF of 41% and the SF decreased with increasing Zn content. Somekawa et al. reported that the segregation of some alloying elements as soluble atoms at the grain boundaries can promote the grain boundary sliding, thus enhancing the deformability of Mg binary alloys [22]. Here, the excellent SF of the Ac-1Zn alloy was attributed to the segregation of Zn at the grain boundaries. With increasing Zn content, the amounts of (α-Mg + MgZn) eutectic cell rapidly increased. Although the although the second phase can greatly enhance the strength through the second phase strengthening, the increase of (α-Mg + MgZn) eutectic cell possibly introduced micro-crack sources, thus reducing the plasticity of the alloys. The reduced SF of the Mg-1Zn alloy by 20.5% after the T4 treatment was attributed to the elimination of Zn-segregation while the enhanced SF of the Mg-7Zn alloy was resulted from the reduction of (α-Mg + MgZn) eutectic cell.

3.4.2. Deterioration of mechanical properties of Mg-Zn alloys due to corrosion in Hanks' solution

Figure 3.8 shows the comparison of UCS and SF retention of Mg-Zn alloys with immersion time. The UCS and SF retention were calculated by dividing the values after immersion test by the initial values. The deterioration of UCS and SF can be divided into 2

groups: the high retention group including Ac-1Zn, T4-1Zn, T4-5Zn and T4-7Zn alloys and the low retention group including Ac-5Zn and Ac-7Zn alloys.

The decrease of mechanical properties can be explained with the corrosion behavior of the Mg-Zn alloys. In the case of the Ac-1Zn, T4-1Zn, T4-5Zn and T4-7Zn alloys, the volume fraction of Zn-rich phases was either very low or the (α-Mg + MgZn) eutectic cells were discretely distributed in the microstructure. Hence, in addition the filiform corrosion spreads on the surface (Chapter 2, Fig. 2.5(a-b)) and the micro-galvanic corrosion occur only at the areas surrounding (α-Mg + MgZn) eutectic cells exposed to the surface (Chapter 2, Fig. 2.15(e-f)). Consequently, the UCS and SF of these alloys decreased slightly with immersion time.

In the case of the Ac-5Zn and Ac-7Zn alloys, the high-volume fraction of Zn-rich phases formed a network-like structure. Simultaneously with the growth of filiform corrosion on the surface, the micro-galvanic corrosion propagated along the network structure into the interior of the alloys (Chapter 2, Fig. 2.15(c-d)). The formation of large-deep holes due to the dissolution of Mg substrate was likely to cause stress concentration during the compression test, resulting in the cracks initiation and propagation. As a result, the mechanical properties of the Ac-5Zn and Ac-7Zn alloys decline rapidly with immersion time.

The biomedical implant materials should have not only high initial mechanical strength, but also remains the mechanical properties over a certain time depending on the implantation site [5,14]. Normally, the mechanical support is required for 12–24 weeks depending on the clinical conditions.

The comparison between strength integrity of the Ac-1Zn, T4-1Zn, T4-5Zn and T4-7Zn alloys and the cortical bones is shown in Figure 3.9. It can be seen that the compressive strength of the alloys after immersion in Hanks' solution for 28 days was still higher than that of the cortical bones (130-180 MPa) [2]. However, the compressive strength of the T4-5Zn and T4-7Zn alloys showed a relatively fast decrease and it was estimated that they will be lower than the strength of cortical bones in the next 1-2 weeks. On the other hand, the Ac-1Zn and T4-1Zn alloys showed a slow decline and they were highly expected to remain higher strength than the cortical bones in the next 8-12 weeks.

3.5 Conclusion

In this study, the microstructure and mechanical properties of the as-cast and T4-treated Mg-Zn binary alloys were investigated using optical microscopy, micro-Vickers hardness and compression tests. The mechanical integrity of Mg-Zn alloys was also studied by a combination of immersion tests and post-compression tests. The following conclusion were given.

1. Addition of Zn as an alloying element significantly refined the grain size of as-cast Mg-Zn alloys. With increasing Zn content, (α-Mg + MgZn) eutectic cell and Zn-segregated phase precipitated at the grain boundaries and dendrite arms, forming a network-like structure. The volume fraction of (α-Mg + MgZn) eutectic cell and Zn-segregated phase increased with increasing Zn content. The grain size of the Mg-Zn alloys increased after T4 treatment due to the dissolution of network-like structure of Zn-rich phases into Mg matrix.

2. The micro-Vickers hardness, 0.2% proof stress and ultimate compressive strength of the as-cast alloys increased significantly with increasing Zn content up to 7 wt%. The enhanced mechanical strength of the as-cast alloys was attributed to the grain boundary strengthening, solid solution strengthening and second phase strengthening. The Zn-segregation at the grain boundaries supposedly contributed to the high strain at failure of Ac-1Zn alloy while increasing amounts of (α-Mg + MgZn) eutectic cell reduced the strain due to introducing crack sources. T4 treatment dissolved (α-Mg + MgZn) eutectic cell and Zn-segregated phase into Mg matrix, thus the strength and strain of the alloys decreased.

3. The mechanical properties of Mg-Zn alloys decreased with extension of immersion time in Hanks' solution. The deterioration of mechanical properties depended on the corrosion form of Mg-Zn alloys which was dominated by the microstructure. The Ac-1Zn, T4-1Zn, T4-5Zn and T4-7Zn alloys mainly suffered from filiform corrosion showing high mechanical property retention while the Ac-5Zn and Ac-7Zn alloys suffered severe micro-galvanic corrosion exhibiting low mechanical property retention. After 28 days, the Ac-1Zn, T4-1Zn, T4-5Zn and T4-7Zn alloys still showed higher compressive strength than the cortical bones. The Ac-1Zn and T4-1Zn alloys were expected to remain high mechanical support in the next 8-12 weeks.

3.6 References

[1] F. Witte, The history of biodegradable magnesium implants: A review, Acta Biomater. 6 (2010) 1680–1692. https://doi.org/10.1016/j.actbio.2010.02.028.

[2] M.P. Staiger, A.M. Pietak, J. Huadmai, G. Dias, Magnesium and its alloys as orthopedic biomaterials: A review, Biomaterials. 27 (2006) 1728–1734. https://doi.org/10.1016/j.biomaterials.2005.10.003.

[3] M. Esmaily, J.E. Svensson, S. Fajardo, N. Birbilis, G.S. Frankel, S. Virtanen, R. Arrabal, S. Thomas, L.G. Johansson, Fundamentals and advances in magnesium alloy corrosion, Prog. Mater. Sci. 89 (2017) 92–193. https://doi.org/10.1016/j.pmatsci.2017.04.011.

[4] S. Agarwal, J. Curtin, B. Duffy, S. Jaiswal, Biodegradable magnesium alloys for orthopaedic applications: A review on corrosion, biocompatibility and surface modifications, Mater. Sci. Eng. C. 68 (2016) 948–963. https://doi.org/10.1016/j.msec.2016.06.020.

[5] Y.F. Zheng, X.N. Gu, F. Witte, Biodegradable metals, Mater. Sci. Eng. R. 77 (2014) 1–34. https://doi.org/10.3390/met8100804.

[6] M.I. Rahim, S. Ullah, P.P. Mueller, Advances and challenges of biodegradable implant materials with a focus on magnesium-alloys and bacterial infections, Metals (Basel). 8 (2018) 532. https://doi.org/10.3390/met8070532.

[7] G. Song, Control of biodegradation of biocompatable magnesium alloys, Corros. Sci. 49 (2007) 1696–1701. https://doi.org/10.1016/j.corsci.2007.01.001.

[8] X. Gu, Y. Zheng, Y. Cheng, S. Zhong, T. Xi, In vitro corrosion and biocompatibility of binary magnesium alloys, Biomaterials. 30 (2009) 484–498. https://doi.org/10.1016/j.biomaterials.2008.10.021.

[9] J. Kuhlmann, I. Bartsch, E. Willbold, S. Schuchardt, O. Holz, N. Hort, D. Höche, W.R. Heineman, F. Witte, Fast escape of hydrogen from gas cavities around corroding magnesium implants, Acta Biomater. 9 (2013) 8714–8721. https://doi.org/10.1016/j.actbio.2012.10.008.

[10] T. Kraus, S.F. Fischerauer, A.C. Hänzi, P.J. Uggowitzer, J.F. Löffler, A.M. Weinberg, Magnesium alloys for temporary implants in osteosynthesis : In vivo studies of their

degradation and interaction with bone, Acta Biomater. 8 (2012) 1230–1238. https://doi.org/10.1016/j.actbio.2011.11.008.

[11] D. Noviana, D. Paramitha, M.F. Ulum, H. Hermawan, The effect of hydrogen gas evolution of magnesium implant on the postimplantation mortality of rats, J. Orthop. Transl. 5 (2016) 9–15. https://doi.org/10.1016/j.jot.2015.08.003.

[12] C. Plaass, S. Ettinger, L. Sonnow, S. Koenneker, Y. Noll, A. Weizbauer, J. Reifenrath, L. Claassen, K. Daniilidis, C. Stukenborg-Colsman, H. Windhagen, Early results using a biodegradable magnesium screw for modified chevron osteotomies, J. Orthop. Res. 34 (2016) 2207–2214. https://doi.org/10.1002/jor.23241.

[13] D. Pham, S. Hiromoto, E. Kobayashi, Influences of Zinc Content and Solution Heat Treatment on Microstructure and Corrosion Behavior of Mg-Zn Binary Alloys, Corrosion. 77 (2021) 323–338. https://doi.org/10.5006/3672.

[14] J.W. Lee, H.S. Han, K.J. Han, J. Park, H. Jeon, M.R. Ok, H.K. Seok, J.P. Ahn, K.E. Lee, D.H. Lee, S.J. Yang, S.Y. Cho, P.R. Cha, H. Kwon, T.H. Nam, J.H. Lo Han, H.J. Rho, K.S. Lee, Y.C. Kim, D. Mantovani, Long-term clinical study and multiscale analysis of in vivo biodegradation mechanism of Mg alloy, Proc. Natl. Acad. Sci. U. S. A. 113 (2016) 716–721. https://doi.org/10.1073/pnas.1518238113.

[15] T.B. Massalski, H. Okamoto, Binary Alloys Phase Diagrams, 2000. https://doi.org/10.1007/BF02645363.

[16] S. Cai, T. Lei, N. Li, F. Feng, Effects of Zn on microstructure, mechanical properties and corrosion behavior of Mg-Zn alloys, Mater. Sci. Eng. C. 32 (2012) 2570–2577. https://doi.org/10.1016/j.msec.2012.07.042.

[17] S. Zhang, X. Zhang, C. Zhao, J. Li, Y. Song, C. Xie, H. Tao, Y. Zhang, Y. He, Y. Jiang, Y. Bian, Research on an Mg-Zn alloy as a degradable biomaterial, Acta Biomater. 6 (2010) 626–640. https://doi.org/10.1016/j.actbio.2009.06.028.

[18] E.O. Hall, Yield Point Phenomena in Metals and Alloys, Springer, 1970.

[19] C.J. Boehlert, K. Knittel, The microstructure, tensile properties, and creep behavior of Mg-Zn alloys containing 0-4.4 wt.% Zn, Mater. Sci. Eng. A. 417 (2006) 315–321. https://doi.org/10.1016/j.msea.2005.11.006.

[20] H. Somekawa, Y. Osawa, T. Mukai, Effect of solid-solution strengthening on fracture

toughness in extruded Mg-Zn alloys, Scr. Mater. 55 (2006) 593–596. https://doi.org/10.1016/j.scriptamat.2006.06.013.

[21] D. song YIN, E. lin ZHANG, S. yan ZENG, Effect of Zn on mechanical property and corrosion property of extruded Mg-Zn-Mn alloy, Trans. Nonferrous Met. Soc. China (English Ed. 18 (2008) 763–768. https://doi.org/10.1016/S1003-6326(08)60131-4.

[22] H. Somekawa, A. Singh, R. Sahara, T. Inoue, Excellent room temperature deformability in high strain rate regimes of magnesium alloy, Sci. Rep. 8 (2018) 1–9. https://doi.org/10.1038/s41598-017-19124-w.

Table 3.1 Composition and preparation condition of alloys

Table 3.1 Composition and preparation condition of alloys

Sample name	Composition (wt.%)	Preparation condition
Ac-1Zn	Mg-1%Zn	As-cast
Ac-5Zn	Mg-5%Zn	As-cast
Ac-7Zn	Mg-7%Zn	As-cast
T4-1Zn	Mg-1%Zn	Ac-1Zn + T4 heat treatment at 400 °C for 12 hours
T4-5Zn	Mg-5%Zn	Ac-5Zn + T4 heat treatment at 400 °C for 12 hours
T4-7Zn	Mg-7%Zn	Ac-7Zn + T4 heat treatment at 400 °C for 12 hours

Table 3.2 Chemical composition of Hanks' solution

Reagent	NaCl	KCl	$Na_2HPO_4.H_2O$	KH_2PO_4	$MgSO_4.7H_2O$	$NaHCO_3$	$CaCl_2$
Concentration (g/L)	8.00	0.40	0.06	0.06	0.20	0.35	0.14

Table 3. Mechanical properties of as-cast and T4-treated Mg-Zn alloys

Alloy	0.2% proof stress (PS, MPa)	Ultimate compressive strength (UCS, MPa)	Strain at failure (SF, %)
Ac-1Zn	48	355	40.5
Ac-5Zn	60	383	30.1
Ac-7Zn	109	415	23.4
T4-1Zn	46	329	32.4
T4-5Zn	50	265	23.2
T4-7Zn	65	388	28.7

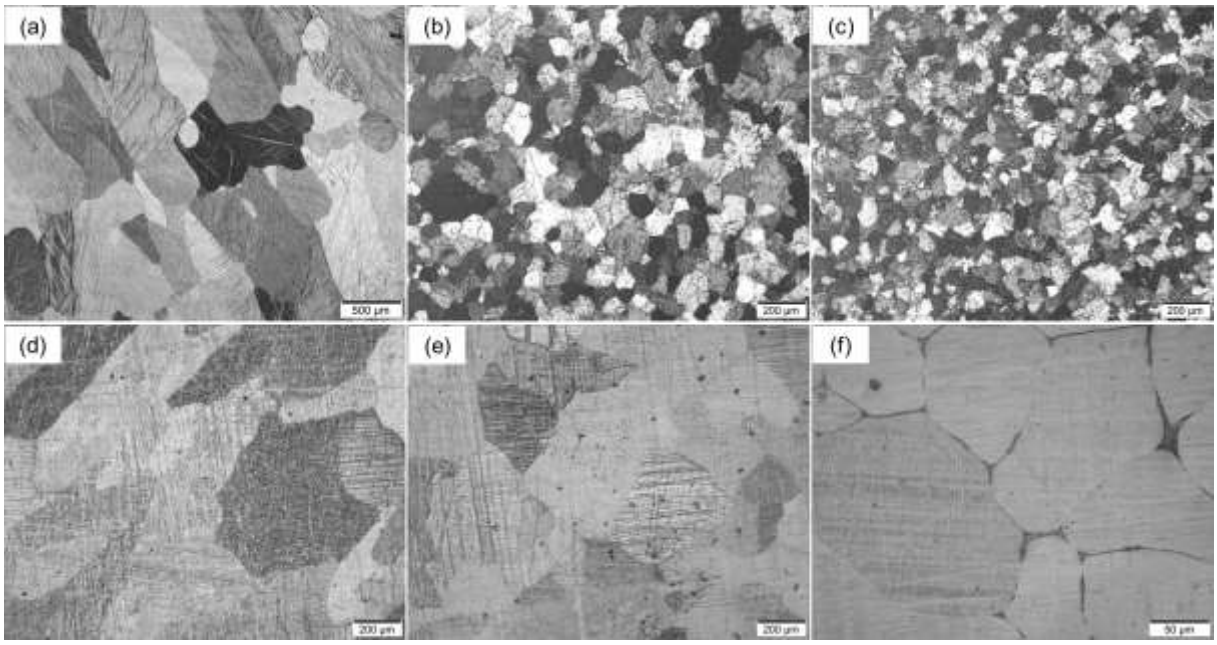

Figure 3.1 Optical micrographs of the as-cast and T4-treated Mg-Zn alloys etched with a Picral solution. (a) Ac-1Zn, (b) Ac-5Zn, (c) Ac-7Zn, (d) T4-1Zn, (e) T4-5Zn and (f) T4-7Zn

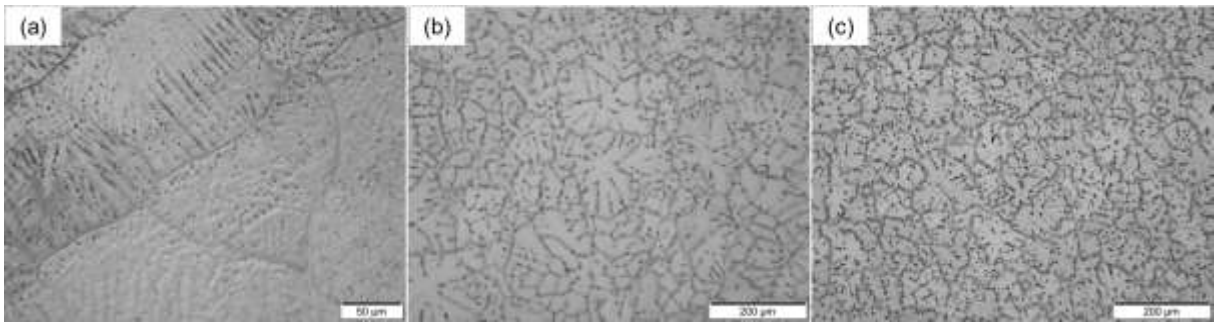

Figure 3.2 Optical micrographs of the as-cast Mg-Zn alloys etched with a Glycol acetic solution. (a) Ac-1Zn, (b) Ac-5Zn and (c) Ac-7Zn

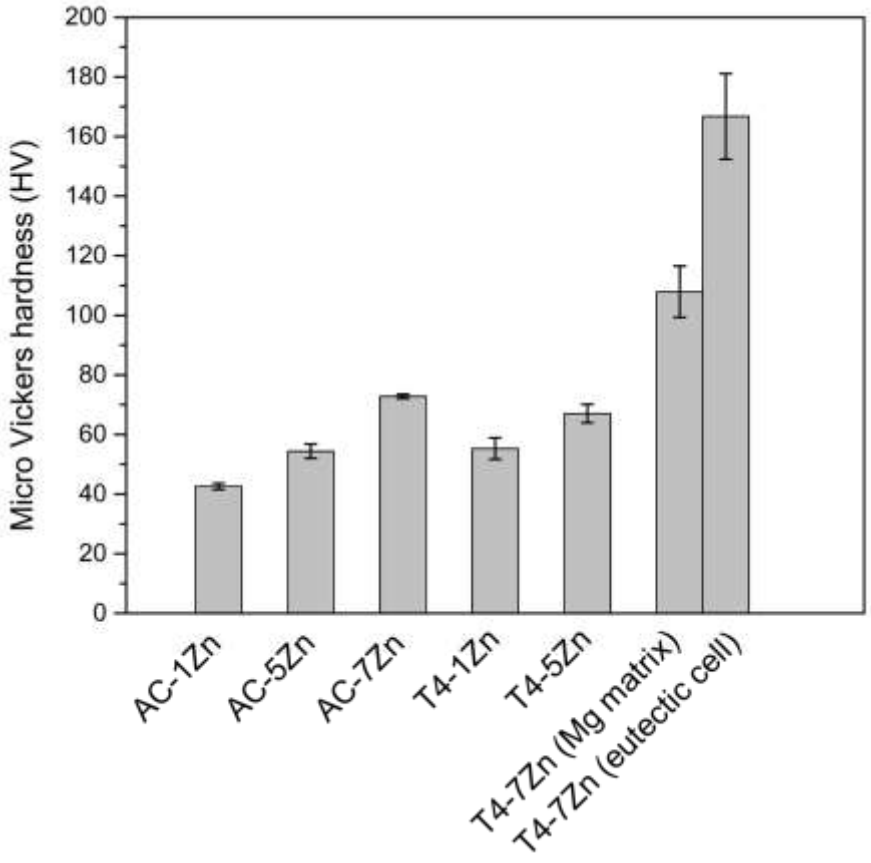

Figure 3.3 Micro Vickers hardness of Mg-Zn alloys

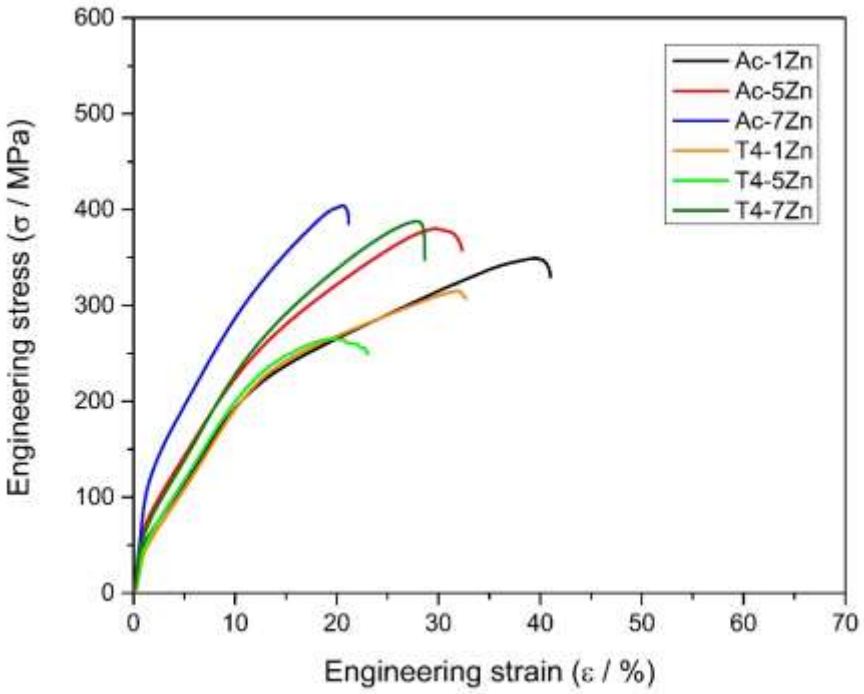

Figure 3.4 Stress-strain curves of Mg-Zn alloys

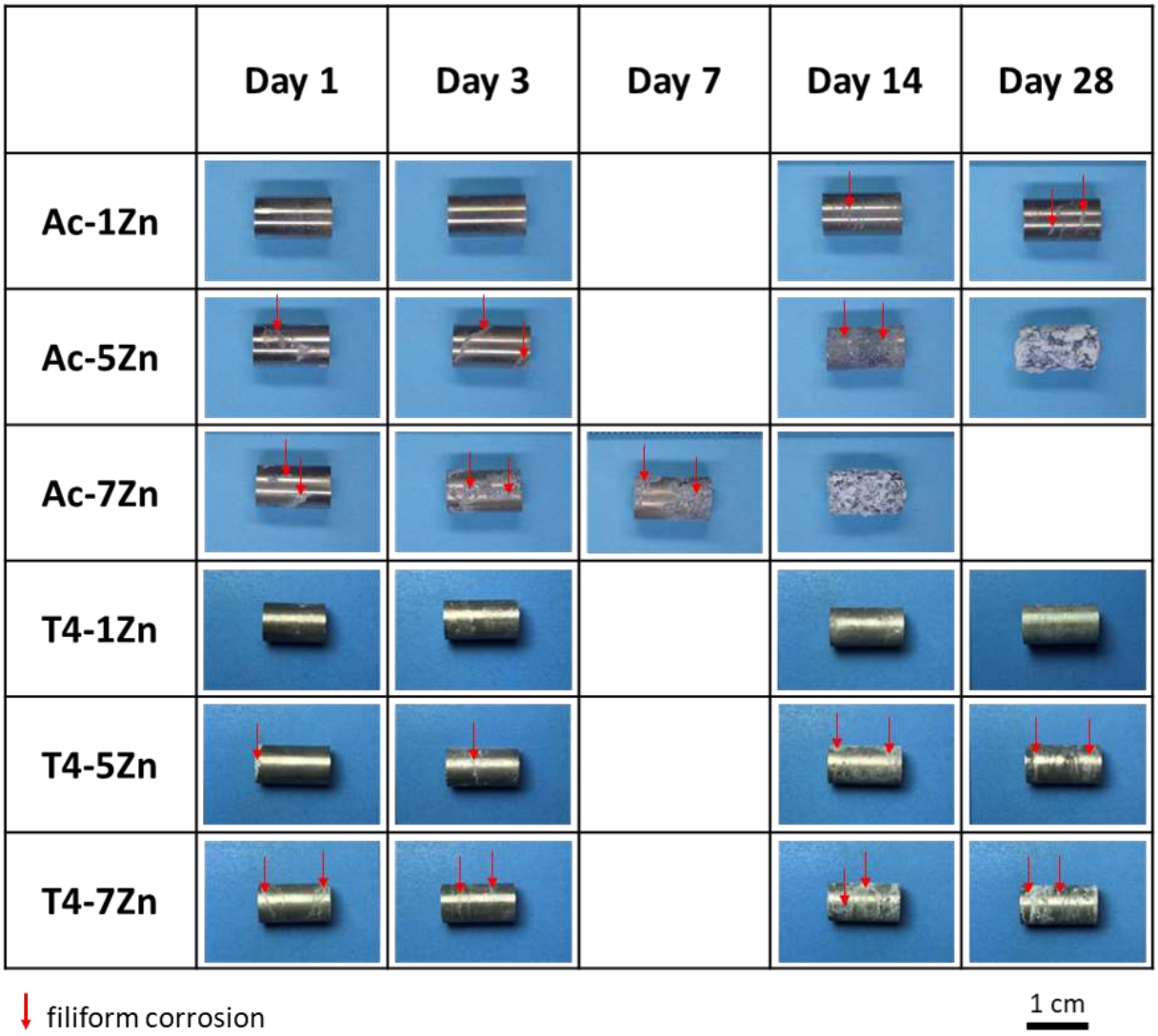

Figure 3.5 Photographic images of Mg-Zn alloys after immersion test

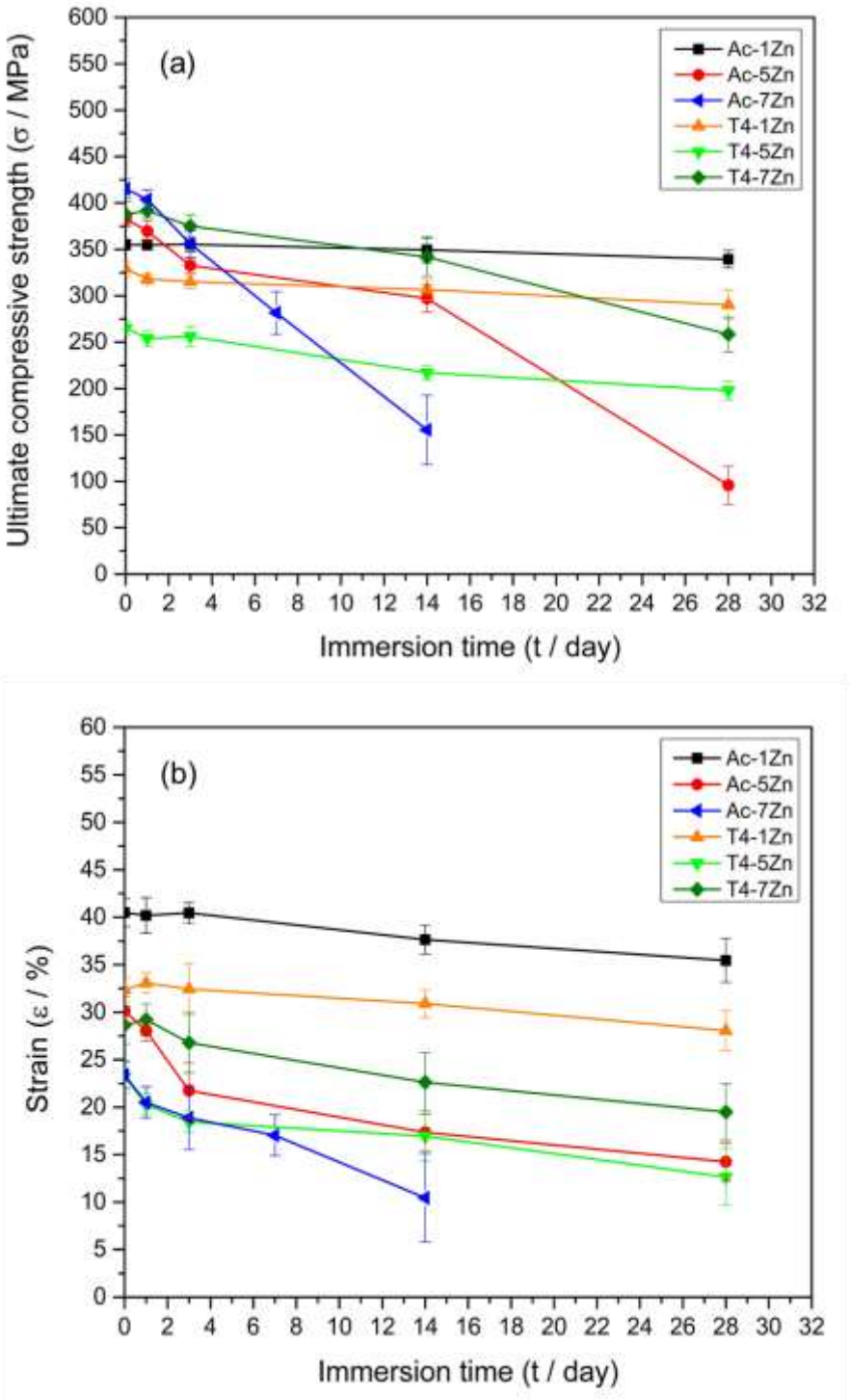

Figure 6. Changes in UCS and SF of Mg-Zn alloys with immersion time in Hanks' solution. (a) UCS and (b) SF

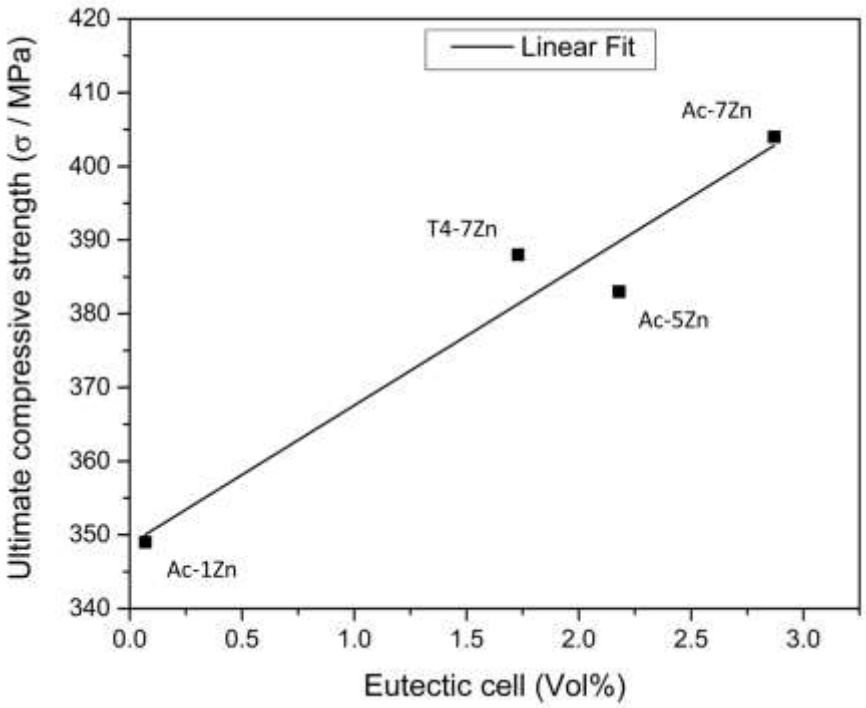

Figure 7. UCS values of Mg-Zn alloys plotted as a function of the volume fraction of (α-Mg + MgZn) eutectic cell

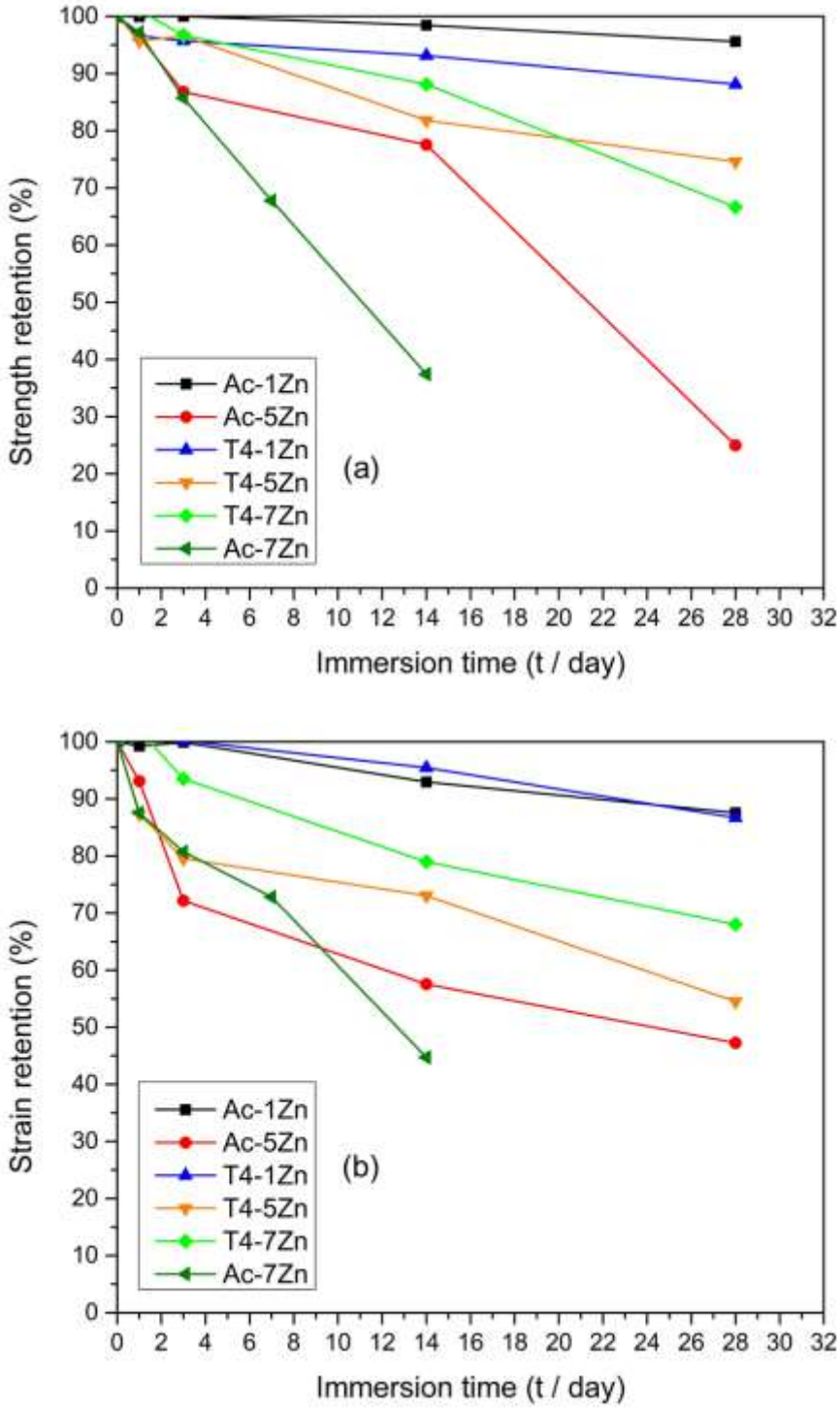

Figure 8. Comparison of UCS and SF retention of Mg-Zn alloys with immersion time. (a) Strength retention and (b) Strain retention

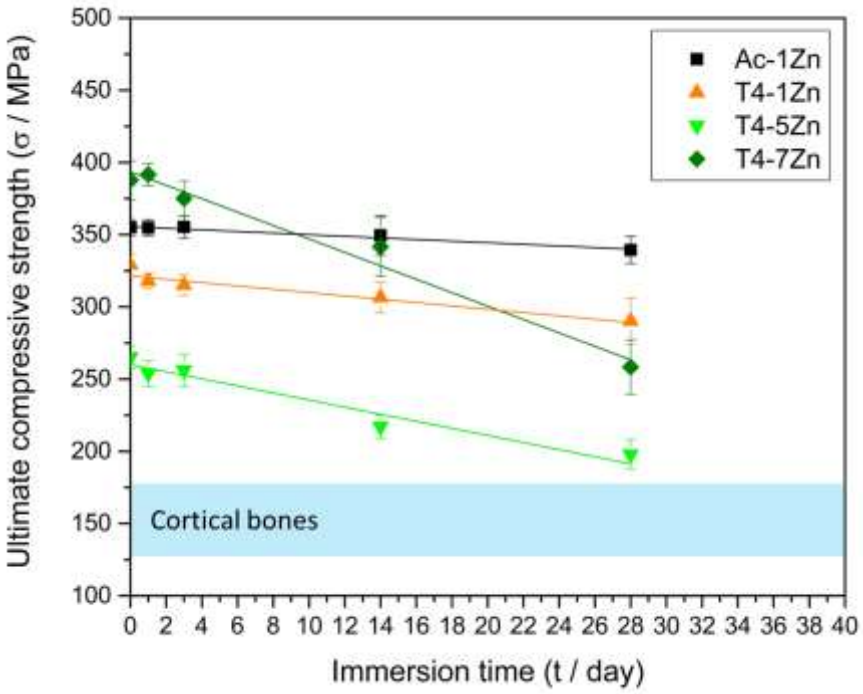

Figure 9. Comparison between strength integrity of Mg-Zn alloys and cortical bones

Chapter 4

Influence of Substrate Microstructure on Uniformity of Hydroxyapatite Coating and Corrosion Behavior of Coated Mg-Zn Alloys

4.1 Introduction

Magnesium and its alloys are being widely investigated as biodegradable implant materials due to their excellent biocompatibility and mechanical properties close to human bone [1–4]. However, the critical problem of Mg and its alloys is poor resistance to corrosion in the physiological environment, causing a rapid deterioration of mechanical properties and the release of large amounts of hydrogen gas, thus greatly limiting its practical uses for implant applications [1,5–7]. There are effective methods that can be adopted to improve corrosion resistance of magnesium alloys including elemental alloying, heat treatment and surface coating [8–12]. Alloying elements with an appropriate composition can greatly improve the corrosion resistance and mechanical properties of Mg alloys. Up to date, two primary groups of Mg-based alloys have been widely studied for biomedical applications which are magnesium-aluminum (Mg-Al) and magnesium-rare earth elements (Mg-RE) series alloys. Although Al and RE elements can moderate the corrosion rate and enhance the mechanical strength, the biocompatibility of Al and RE elements is poor or not precisely understood [13–16]. The attention is then paid to elements with a relatively high biocompatibility such as and zinc (Zn). Zn can refine the crystal grains of Mg alloys which increase both corrosion resistance and mechanical properties [17,18]. In addition, Zn is an essential trace element and the daily intake of 15 mg Zn is permissible [4]. However, increasing concentration of Zn will precipitate second phases with noble potential which enhance the galvanic corrosion between second phase and Mg matrix [19,20]. Therefore, the appropriate Zn content and heat treatment should be investigated to achieve both corrosion resistance and mechanical properties.

In the previous study, we have prepared Mg-Zn binary alloys with various Zn contents and solution heat treatment (T4 treatment) with the aims of developing magnesium alloys possessing adequate corrosion resistance and mechanical properties for implant application, and being free of harmful compositions. It is found that the addition of Zn as alloying element and the T4 solution treatment significantly improved the corrosion resistance of the magnesium alloys in Hanks' solution [21]. The initial corrosion of Mg-Zn alloys in Hanks' solution causes an increase in pH near the sample surfaces, initiating the deposition of calcium phosphate layer from Hanks' solution which is beneficial to the subsequent corrosion resistance. However, it was also found that the initial corrosion of magnesium caused rapid hydrogen (H_2) gas evolution. The H_2 gas evolution of magnesium alloys after their implantation are reported to cause inhibition of cell attachment and tissue healing [22–24]. Thus, it is suggested that the initial corrosion of magnesium alloys should be retarded to promote the bone healing.

Surface coating is an effective method to moderate the rapid corrosion of Mg in physiological environments and various coating techniques have been developed to improve the corrosion resistance of Mg alloys [11,12]. The coatings are expected to effectively protect the substrate Mg alloys in the early stage, so that the coated alloys can provide sufficient support to the healing parts. In addition, besides reducing the corrosion rate of the substrate Mg alloys, the biocompatibility of the coatings should also be considered for the biomedical implant applications [12,25]. Hydroxyapatite ($Ca_{10}(PO_4)_6(OH)_2$, HAp) is currently used as biomedical materials due to the facts that it is a major component of the human bones and has excellent biocompatibility [26,27]. HAp is practically coated on titanium-based implants to promote bone conduction for bone-implant integration [28].

There are numerous studies reporting that the HAp coatings on the substrate Mg alloys can effectively reduce the corrosion rate, especially in the early stages of implantation, as well as enhance the biocompatibility and osteoconductivity of the alloys [29–33].

There are several methods used to form HAp coating on magnesium alloys [34–36]. Among them, the chemical solution deposition process developed by Hiromoto et al. shows many advantages including its simplicity, low treating temperature, short processing time and formation of highly-crystallized HAp coatings [34]. The results demonstrated that the HAp coating prepared on pure Mg, Mg-AZ31 and Mg-WE43 alloys by chemical solution method improved significantly the corrosion resistance and the cell biocompatibility of the substrates [33,37,38]. However, these substrates either contained no second phases, or the volume fraction and particle size of second phase were negligible. Effects of the substrates containing a

relatively high amount of second phase on the formation and properties of HAp coating has not been investigated.

In this study, the HAp coatings were prepared on Mg-Zn alloys with various microstructures by the chemical solution deposition process. The morphology of the HAp coatings and the corrosion behavior of HAp-coated Mg-Zn alloys were investigated. The relationship between the microstructure of Mg-Zn alloy substrates and the corrosion protectiveness of the HAp coatings was then examined.

4.2 Experimental procedures

4.2.1 Alloys preparation

High purity Mg ingots (> 99.9 wt%) and Zn shots (> 99.99 wt%) were melted in an alumina crucible, under protection with a 95 vol% Ar + 5 vol% CH_2FCF_3 mixed gas atmosphere in an induction furnace. The molten metals were gently stirred for 10 minutes, then cast into a copper mold at a room temperature. The as-cast ingots were cylindrical-shape with the dimensions of 25 mm in diameter and 70 mm in length. The solution heat treatment (T4 treatment) was carried out in a high vacuum furnace at 400 ^oC for 12 h, subsequently quenched in water at a room temperature. The as-cast and T4-treated Mg-Zn ingots were machined to a cylindrical shape with the dimensions of 15 mm in diameter and 70 mm in length by computer numerical control (CNC) machining. Disks of 2 mm thickness were then cut from the machined ingots for further analysis and experiments.

4.2.2 Synthesis of HAp on Mg-Zn alloys

The surfaces of the Mg-Zn disks were ground using SiC paper up to 4000 grit, then ultrasonically rinsed in acetone for 5 minutes. The coating treatment solution for HAp coating was prepared by mixing the following solutions to obtain a pH of 7.8: ethylenediaminetetraacetic acid calcium disodium salt hydrate (Ca-EDTA, 0.5 mol/L), potassium dihydrogen phosphate (KH_2PO_4, 0.5 mol/L), and sodium hydroxide (NaOH, 1N). Then, the final concentration of Ca-EDTA and KH_2PO_4 of the treatment solution became ca. 0.2 mol/L. The specimens were immersed in the treatment solution at 90 ^oC for 2 h. The names, compositions and preparation conditions of the samples are listed in Table 4.1.

4.2.3 Immersion test

The HAp-coated samples were immersed in Hanks' solution with the ratio of the surface area to Hank's solution volume at 1 cm^2/50 ml. The components of Hanks' solution are shown in Table 4.2. The containers were placed in an incubator at 37 ^oC for 14 days. Three samples from each preparation condition were used for the immersion test. The concentration of Mg^{2+} ions released in Hanks' solution was quantified after 1, 3, 5, 7, 9, 11, 13 and 14 days of immersion by a colorimetric method using Xylidyl blue-I (1-azo-2-hydroxy-3- (2,4-dimethylcarboxya-nilido)naphthalene-1-(2-hydroxybenzene-5-sulfonate) [39–41]. Magnesium ions combine with Xylidyl blue-I to form a water soluble chelate which absorbs light with a wave length of 520 nm. Then, the absorbance at 520 nm was measured with a microplate Spectrophotometer (Thermo Scientific, Multiskan GO).

The amount of Mg^{2+} ions released per each day was given by equation (4.1) [41]:

$$A_i = 0.0275C_i - (0.0275 - 0.015)C_{i-1} \quad (4.1)$$

where C_i is the concentration of Mg^{2+} ions (mg/L) in the testing solution at day i and A_i is the total amount of Mg^{2+} ions (mg) at day i. The accumulated Mg^{2+} ions released per unit surface area (mg/cm^2) was calculated by equation (4.2) [41]:

$$R_i = \frac{A_i}{S_0} \quad (4.2)$$

where S_0 is the total surfaces area (cm^2) of the samples before immersion test.

After Day14, all the samples were removed from the testing solution, gently rinsed with distilled water and dried with a N_2 gas flow for further characterizations.

4.2.4 Polarization and impedance tests

The potentiodynamic polarization and electrochemical impedance spectroscopy (EIS) tests were conducted in Hanks' solution at 37 ^oC using potentiostat (Solartron, SI 1287) and impedance analyzer (Solartron, SI 1260). The surface of the samples for polarization and impedance tests was covered with a polytetrafluoroethylene (PTFE) tape and the remaining 1 cm^2 area was exposed as a working electrode to 500 ml of Hanks' solution. A saturated

Ag/AgCl electrode and a platinum plate were used as the reference and the counter electrodes, respectively. In the polarization test, the open circuit potential (OCP) was monitored for 1800 s to obtain a relatively stable OCP. After that, the potential of the samples was anodically swept from -0.1 V vs. OCP at a scanning rate of 1 mV/s. In the EIS test, the spectrum of the samples was measured after 0, 0.5, 2, 4 and 6 h of immersion at the OCP at each measurement time. The scan frequency ranged from 10^5 Hz to 10^{-2} Hz and the perturbation amplitude was 5 mV. The EIS spectra were analyzed using the ZView software.

4.2.5 Materials characterization

Phase composition of the samples was characterized using X-rays diffractometry (XRD, Bruker, D2 Phaser). The samples for the microstructure observation were ground to 4000 grit SiC paper, then successively polished with 1 μm alumina paste and etched by solution containing 60 ml ethylene glycol, 20 ml acetic acid, 1 ml nitric acid and 20 ml distilled water. The metallographic images were observed using optical microscope (Olympus BX51M). The surface and cross-section images of the samples before and after immersion test were characterized using backscattered electron microscope (BSE-SEM, HITACHI, Miniscope TM-3030Plus) and field-emission scanning electron microscope (FE-SEM, JEOL, JSM-7200F) equipped with an energy-dispersive X-ray spectrometer (EDS, JEOL, JED-2300).

4.3 Results and discussion

4.3.1 Formation of HAp coating on Mg-Zn alloy substrates

(1) Microstructure of Mg-Zn alloys

Figure 4.1 shows the optical metallographic images of as-cast and T4-treated Mg-xZn alloys. It can be seen that the microstructure of the as-cast Mg-Zn alloys consisted of α-Mg matrix and second phases mainly precipitated along the grain boundaries as shown in Fig. 1(a-c). The average grain size of as-cast alloys decreased with an increase of Zn content. The grain size of the Ac-1Zn, Ac-5Zn and Ac-7Zn alloys was ca. 198.6 ± 28.9 μm, 88.8 ± 7.9 μm, 70.3 ± 6.4 μm, respectively. After T4-treatment, the T4-7Zn alloy exhibited a grain size of 107 ± 6.6 μm and the second phase particles were randomly observed in grain boundaries and within the grains.

Figure 4.2 shows the SEM microstructure images of the Ac-1Zn, Ac-5Zn and Ac-7Zn and T4-7Zn alloys. In the Ac-1Zn, Ac-5Zn and Ac-7Zn alloys, the microstructure consisted of α-Mg matrix, (α-Mg + MgZn) eutectic cells and Zn-segregated regions as shown in Fig. 4.2(a-c). The size and volume fraction of (α-Mg + MgZn) eutectic cells increased with increasing Zn content. It was reported in our previous work that the volume fraction and the particle size of (α-Mg + MgZn) eutectic cells were ca. 0.07 vol.% and 0.52 μm, 2.18 vol.% and 1.81 μm, 2.87 vol.% and 2.18 μm for the Ac-1Zn, Ac-5Zn and Ac-7Zn alloys, respectively [21]. The T4-7Zn alloy showed α-Mg matrix with large irregular-shape and round-shape (α-Mg + MgZn) eutectic cells as shown in Fig. 4.2(d). This was because during the T4 treatment, Zn-segregated regions were completely dissolved into the matrix and (α-Mg + MgZn) eutectic cells were melted and solidified. The volume fraction and particle size of (α-Mg + MgZn) eutectic cells in the T4-7Zn alloy were ca. 1.73 vol.% and 27.76 μm, respectively [21].

(2) **Characteristics of HAp coating formed on Mg-Zn alloy substrates**

Figure 4.3 shows the XRD patterns of the Mg-Zn alloys after the coating treatment. All the coated samples showed diffraction peaks of HAp, confirming the formation of HAp on the Mg-Zn alloy substrates. The diffraction peaks of MgZn second phase were not observed in Fig. 4.3 because the volume fraction of MgZn second phase was relatively low in the substrate alloys and the surfaces of Mg-Zn alloys were covered with HAp layers. The diffraction intensity of HAp peaks was almost the same between the samples. For all the samples, the diffraction intensity of the plane $(002)_{HAp}$ was higher than that of other planes, indicating that the plane $(002)_{HAp}$ was the preferable growth direction of HAp crystals like in the HAp coatings formed on pure Mg and Mg-AZ alloy [37,42]. The XRD results revealed that HAp coatings formed on the Mg-Zn alloy substrates by chemical solution treatment possessed a similar composition and orientation.

Figure 4.4 shows the SEM surface images of the HAp-coated samples. The surface of all samples was covered with rod-like HAp crystals and flower-like agglomerates of HAp rod crystals. The HAp coatings formed on the Mg-Zn substrates showed similar surface appearance to those formed on pure Mg and Mg-AZ alloys in the previous works [37,42]. The Ac-1Zn/HAp and Ac-5Zn/HAp showed uniform coatings without apparent defects, as shown in Fig. 4(a) and (b), respectively. On the contrary, cracks were randomly observed in HAp coatings of the Ac-7Zn/HAp and T4-7Zn/HAp, as shown in Fig. 4.4(c) and (d), respectively. Interestingly, the size

of the cracks of the Ac-7Zn/HAp was relatively smaller than that of the T4-7Zn/HAp. The crack size was ca. 30 μm and 80 μm in length for the Ac-7Zn/HAp and T4-7Zn/HAp, respectively. Fig. 4.4(e) showed a high magnification image of the area with rod-like HAp crystals and flower-like agglomerates of HAp rod crystals.

Figure 4.5 shows the cross-section SEM images of the HAp-coated samples. All the HAp coatings consisted of two layers: a dense inner layer and a porous outer layer. The porous outer layer was made up of rod-like HAp crystals and the dense inner layer was composed of dome-shape HAp particles. HAp layers were able to grow on both α-Mg matrix and (α-Mg + MgZn) cells. The inner layers of the Ac-1Zn/HAp and Ac-5Zn/HAp were dense and did not show cracks or pores. The inner layer of the Ac-7Zn/HAp showed micro-cracks appeared in the areas neighboring to (α-Mg + MgZn) cells. The inner layer of the T4-7Zn/HAp exhibited large cracks and was delaminated on the (α-Mg + MgZn) cells exposed on the surface. These results indicated that the uniformity of HAp coatings was greatly influenced by the substrate microstructure with the finer and lower volume fraction of (α-Mg + MgZn) eutectic cells enhancing the uniformity of HAp coating. Tomozawa et al. reported that the corrosion protectiveness of the HAp coating prepared by the chemical solution treatment was controlled by the thickness and uniformity of the dense inner layer [43]. In the case of Mg-Zn alloys, the thickness of the dense inner layers was ca. 1.5 μm for all the alloys. The corrosion protectiveness of the HAp coatings is thus expected to depend on the defects of the coatings.

(3) Influence of substrate microstructure on HAp coating

Based on the experimental results obtained in this study (Fig. 4.1 and Fig. 4.5) and the growth mechanism of HAp coating on pure Mg suggested by Hiromoto et al. [37], the formation mechanism of HAp coatings on the Mg-Zn alloys and the influence of the substrate microstructure on the HAp coating were proposed as illustrated in Figure 4.6. Regardless of the microstructure of Mg alloys, the HAp coatings are formed as follows. Immediately after immersing the substrate Mg alloy in the coating solution, the corrosion of Mg alloy initiates as shown in the equation (3) and (4). As a result of the corrosion reactions, the pH near the alloy surface increases rapidly with H_2 gas evolution. The rapid increase of the near surface pH initiates the simultaneous precipitation of HAp nuclei and $Mg(OH)_2$ on the surface according to the equations (5) and (6) while the H_2 gas evolution prevents the deposition of HAp [43]. Because HAp has much lower solubility than $Mg(OH)_2$, the nucleation of HAp occurs more

preferentially than the formation of $Mg(OH)_2$ as shown in Fig. 4.6(a) [37]. As the coating time passes, the HAp nuclei grow and bond together to form the dense inner layer. The dense inner layer moderates the corrosion of the substrate, resulting in the growth of rod-like HAp crystals from the inner layer.

$$Mg \rightarrow Mg^{2+} + 2e^{-} \tag{4.3}$$

$$2H_2O + 2e^{-} \rightarrow 2OH^{-} + H_2 \tag{4.4}$$

$$Mg^{2+} + 2OH^{-} \rightarrow Mg(OH)_2 \tag{4.5}$$

$$10Ca^{2+} + 6PO_4^{3-} + 2OH^{-} \rightarrow Ca_{10}(PO_4)_6(OH)_2 \tag{4.6}$$

In the case of the Ac-1Zn alloy, the microstructure contains negligible amounts of Zn-rich phases. Therefore, the initial corrosion occurs apparently uniformly over the entire surfaces and HAp nuclei homogeneously deposit on the surface of the Ac-1Zn alloy. As a result, the defect-free HAp coating is formed as shown in Fig. 4.5(a) and 4.6(b).

In the case of the Ac-5Zn and Ac-7Zn alloys, the microstructure contains the Zn-rich phases of larger than a few micrometers but smaller than a few ten of micrometers. The micro-galvanic corrosion occurs between the Zn-rich phases and the α-Mg matrix. The pH-increase and H_2 gas evolution in the areas where micro-galvanic corrosion occurs thus become more intense than the surrounding areas. Tomozawa et al. reported that the H_2 gas bubbles generated during the octacalcium phosphate (OCP) coating procedure formed nanopores and cracks in the inner layer of OCP layer [43]. Because the Zn-rich phases have similar composition and the galvanic corrosion rate per unit area of the Zn-rich phase is assumed to be the same in the Mg-Zn alloys with various Zn contents, the pH increase and generation amount of H_2 gas depends on the size of Zn-rich phases.

In the Ac-5Zn alloy, the size of the Zn-rich phases is relatively small, thus the deposited HAp can cover them easily as shown in Fig. 4.5(b). The Zn-rich phases in the Ac-7Zn alloy are bigger than those in the Ac-5Zn alloy. Therefore, it takes longer time to cover up the Zn-rich phases and the large amount of H_2 gas generation causes the cracks in HAp layers as shown in

Fig. 4.5(c) and 4.6(c). The thicker HAp layer on Zn-rich phases than on α-Mg matrix indicates the intense corrosion around the Zn-rich phases, as shown in Fig. 4.5(b) and 4.5(c).

In the case of the T4-7Zn alloy, it contains the Zn-rich phases of more than a few tens of micrometers, which are the biggest among the Mg-Zn substrates. Therefore, it takes even longer time to cover up the Zn-rich phases with depositing HAp, which allows the galvanic corrosion to continue to generate a large amount of H_2 gas and $Mg(OH)_2$ around the Zn-rich phases. Because the molar volume ratio of $Mg(OH)_2$ to Mg metal is 1.78, the volume expansion occurs with the corrosion progress of α-Mg matrix [44]. As a result, the previously formed HAp layer is lifted as the substrate expands, leading to the crack formation and delamination of the HAp layer as shown in Fig. 4.5(d) and 4.6(d).

4.3.2 Corrosion behavior of HAp-coated Mg-Zn alloys

(1) Mg^{2+} ions release behavior in Hanks' solution

Figure 4.7 shows the accumulated Mg^{2+} ion release of the HAp-coated samples in Hanks' solution. The Ac-1Zn/HAp and Ac-5Zn/HAp having the HAp coating with few defects showed relatively low Mg^{2+} ion release in the initial stage and showed an abrupt increase of the ion release between Day 3 and Day 5 which was attributed to the breakdown of the HAp coating. After Day 5, the accumulated amount of Mg^{2+} ion of the Ac-1Zn/HAp became almost constant, which was attributed to the high corrosion resistance of the Ac-1Zn alloy substrate and the formation of a corrosion product layer covering the breakdown parts of HAp coating. The Mg^{2+} ion release of the Ac-5Zn alloy was accelerated after Day 3, indicating that the corrosion progression from the breakdown parts exceeded the repair of the coating defects with corrosion products due to the relatively low corrosion resistance of the Ac-5Zn alloy substrate.

The Ac-7Zn/HAp and T4-7Zn/HAp having the HAp coating with partial cracking and delamination showed the larger Mg^{2+} ion release than the Ac-1Zn/HAp and Ac-5Zn/HAp on Day 1. Although the size of cracks on Ac-7Zn/HAp was smaller than that on T4-7Zn/HAp (Fig. 4), the number of cracks was presumably larger on the Ac-7Zn/HAp due to the higher volume fraction of Zn-rich phase of the Ac-7Zn substrate alloy. Moreover, a rapid localized corrosion of substrate Mg could occur at the defects of HAp coatings, accelerating the deposition of corrosion products from Hanks' solution. The coating defects were rapidly covered up with corrosion products, and the subsequent corrosion was retarded. The localized corrosion at the large-size defects on T4-7Zn/HAp is considered to be more rapid than that on Ac-7Zn/HAp,

and the former defects are expected to be covered up earlier than the latter. As a result, the amount of released Mg^{2+} ions from Ac-7Zn/HAp and T4-7Zn/HAp happened to be the same on the first day. After Day 1, the Mg^{2+} ion release rate slowed down with the deposited corrosion products which could once cover and fill in the coating defects. However, due to the lower corrosion resistance of the Ac-7Zn alloy substrate [21], the Mg^{2+} ion release of the Ac-7Zn/HAp was accelerated while the release rate slightly decreased after Day 9. Consequently, the Ac-7Zn/HAp showed the largest Mg^{2+} ion release between all the samples on Day 14. The T4-7Zn/HAp showed the low and constant Mg^{2+} ion release rate after Day 1. It is worth mentioning that although it showed a higher Mg^{2+} ion release than the Ac-5Zn/HAp in the initial stage, the release was almost equal on Day 5 and it was just two third of the Ac-5Zn/HAp on Day 14.

Because the accumulated Mg^{2+} ion release from Day 1 to Day 14 showed almost linear behavior, the release rates of the Ac-1Zn/HAp, Ac-5Zn/HAp, Ac-7Zn/HAp and T4-7Zn/HAp were estimated as ca. 0.015, 0.093, 0.241 and 0.043 $mg \cdot cm^{-2} \cdot d^{-1}$, respectively. This indicated that the Ac-1Zn/HAp showed the highest corrosion resistance and the Ac-7Zn/HAp showed the lowest corrosion resistance between all the HAp-coated samples. The Mg^{2+} ion release rate of the HAp-coated samples and those of the uncoated Mg-Zn alloys referred from [21] were listed in Table 4.3. The corrosion resistance of the HAp-coated samples depended on the volume fraction of Zn-rich phases as with the case of the uncoated Mg-Zn alloy substrates. When the volume fraction of Zn-rich phases was small like 0.07% in the Ac-1Zn alloy, the HAp coating reduced the corrosion rate by 45%. When the volume fraction of Zn-rich phases was relatively large like 2.18% for the Ac-5Zn alloy and 2.87% for the Ac-7Zn alloy, the effect of the HAp coating on the corrosion rate of Mg-Zn alloys was small as 5% for the Ac-5Zn alloy and 15% for the Ac-7Zn alloy. Interestingly, the T4-7Zn alloy having large-size Zn-rich phases with relatively small volume fraction of 1.73% showed no apparent positive effect of the HAp coating on the corrosion rate after 14 days. It was revealed that the corrosion resistance of the HAp-coated samples also depended on the size of Zn-rich phases.

The results demonstrated that although the initial corrosion rate of the HAp-coated Mg-Zn alloys was influenced by the uniformity of HAp coating, the subsequent corrosion behavior of the HAp-coated Mg-Zn alloys in Hanks' solution were dominated by the corrosion behavior of the alloy substrates.

(2) Surface appearance after immersion test and composition of corrosion products

Figure 4.8 shows the optical surface images of the HAp-coated Mg-Zn alloys after immersion in Hanks' solution for 14 days. Only the Ac-1Zn/HAp showed almost no localized corrosion. The surfaces of the Ac-5Zn/HAp, Ac-7Zn/HAp and T4-7Zn/HAp were featured by filiform corrosion with different degrees of corrosion. The surfaces of the Ac-5Zn/HAp and T4-7Zn/HAp were partially damaged by filiform corrosion. The Ac-7Zn/HAp suffered the most severe filiform corrosion with the entire surface was covered by corrosion products. There were also some corrosion pits randomly observed on the Ac-7Zn/HAp.

Figure 4.9 shows the surface and cross-section SEM images of an average surface of the Ac-1Zn/HAp and a corroded region of the Ac-7Zn/HAp and T4-7Zn/HAp after immersion in Hanks' solution for 14 days. The Ac-1Zn/HAp was uniformly covered with corrosion products and did not show any evidence of localized corrosion, as shown in Fig. 4.9(a). The Ac-7Zn/HAp showed large pits partially filled with corrosion products, indicating that the severe localized corrosion occurred and the HAp coating at the corroded area was broken, as shown in Fig. 4.9(b). On the T4-7Zn/HAp, the corrosion pits were fully filled up with the corrosion products and the uncorroded regions showed similar appearance to the Ac-1Zn/HAp surface, as shown in Fig. 4.9(c). The micro-cracks appearing in Fig. 4.9(a) an (c) might be formed when drying the samples.

The cross-sectional images of the three samples clearly showed layers/regions with different contrasts. EDS analysis was carried out on the regions with different contrasts pointed by #1–#3, as marked in Fig. 4.9(d-f). The composition at each point is summarized in Table 4.4. The XRD patterns of the HAp-coated samples after immersion test are shown in Figure 4.10.

The EDS results indicated that in all the three samples, the points #1 and #2 mainly consisted of calcium phosphate. In addition, the XRD patterns of the samples showed no other peaks of calcium phosphate compounds than the peaks of HAp. Thus, it was indicated that the main component of the points #1 and #2 was HAp. The Ca/P ratio and the contrast of the points were different between #1 and #2; therefore, the points #1 located on the HAp layer newly deposited in Hanks' solution and the points #2 located on the original HAp coating layer. The Ca/P ratio of both the original and newly deposited HAp layers was smaller than that of the stoichiometric HAp, which was attributed to the substitution of Mg and Na atoms for the Ca atoms in the HAp structure [30,45]. The points #3 mainly consisted of Mg and O and the diffraction peaks of $Mg(OH)_2$ were observed on the XRD patterns of the Ac-7Zn/HAp and T4-

7Zn/HAp. This indicated that the points #3 points located on the $Mg(OH)_2$ layer. $Mg(OH)_2$ were significant on the Ac-7Zn/HAp and T4-7Zn/HAp due to the high degrees of corrosion on these samples.

(3) Polarization behavior

Figure 4.11 shows the polarization curves of the HAp-coated samples in Hanks' solution. The current density near the corrosion potential (E_{corr}) of the Ac-1Zn/HAp was the lowest, indicating its highest corrosion resistance between the HAp-coated samples. The anodic polarization curves of the Ac-1Zn/HAp and Ac-5Zn/HAp exhibited a wide quasi-passive region with an apparently constant current density of 5×10^{-7}A cm^{-2} with small stepwise fluctuations. The Ac-7Zn/HAp and T4-7Zn/HAp showed higher cathodic current density and the anodic current density increased steeply from the E_{corr} to show a slight constant region around -1.35 V(Ag/AgCl) followed by a steep increase over 10^{-3} A cm^{-2}. This result can be explained by the morphology of HAp coating and the effect of the substrate microstructure. Previously, Hiromoto et al. studied the corrosion behavior of HAp-coated pure Mg and AZ31 alloy in 3.5 wt.% NaCl solution [30]. It was reported that the I_{corr} of the HAp-coated pure Mg and AZ31 alloy was almost equal and did not depend on the kind of the substrate. In their study, the initial corrosion of pure Mg and AZ31 alloy in the coating solution was moderate and the volume fraction of second phase of AZ31 alloy was small. Thus, the HAp coatings possessed almost similar structure and uniformity. As a result, the HAp coatings offered high corrosion protection and had less dependency on the substrate microstructure. In the current study, it was suggested that the largely different microstructures of the four Mg-Zn alloys affected the coating morphology, then the corrosion protectiveness of HAp coatings.

The Ac-1Zn/HAp and Ac-5Zn/HAp showed the uniform HAp coatings without apparent defects as shown in Fig. 4.4(a) and (b), respectively. As a result, the Ac-1Zn/HAp and Ac-5Zn/HAp showed a low quasi-passive current density of about 5×10^{-7} A·cm^2 [46–48]. The stepwise current fluctuation indicated a small breakdown and repair of the HAp coatings. The irreversible breakdown potential (E_b) of the Ac-1Zn/HAp and Ac-5Zn/HAp was –1.23 V and –1.30 V, respectively. In the cases of the Ac-7Zn/HAp and T4-7Zn/HAp, the HAp coatings showed large cracks as shown in Fig. 4.4(c) and (d), respectively. The relatively high cathodic current density of the Ac-7Zn/HAp and T4-7Zn/HAp was attributed to the defects of the HAp coatings at which both cathodic and anodic reactions occur. On the polarization curves of the uncoated Mg-xZn alloys in Hanks' solution, the E_b values of the Ac-7Zn and T4-7Zn covered

with deposited calcium phosphate was −1.36 V(Ag/AgCl) and −1.45 V, respectively [21] which are close to the E_{corr} values of the Ac-7Zn/HAp and T4-7Zn/HAp. This fact indicates that irreversible local corrosion could occur at the coating defects on the Ac-7Zn/HAp and T4-7Zn/HAp at the E_{corr}, so that the steep increase in anodic current density was observed from the E_{corr}.

The cathodic current density depended on the Zn content and heat treatment of Mg-Zn alloy substrates in the same manner as the previous study on the uncoated Mg-Zn alloys [21]. The cathodic reaction of the uncoated Mg-Zn alloys was governed by the volume fraction of the Zn-rich phases [21]. The HAp coating reduced the cathodic current density by 10-100 times. The Ac-1Zn/HAp having a uniform HAp coating showed a 10-100 times lower cathodic current density than the other samples. Although the uncoated Ac-7Zn alloy showed similar cathodic current density to the uncoated Ac-5Zn alloy [21], the Ac-7Zn/HAp having HAp coating with defects showed higher cathodic current density than the Ac-5Zn/HAp having uniform HAp coating (Fig. 4.11). These results indicated that the Hanks' solution permeated through the defects of the HAp coatings and the magnitude of cathodic reaction depended on the uniformity of the HAp coatings which was influenced by the volume fraction and particle size of Zn-rich phases.

(4) Impedance behavior

Figure 4.12 shows the Bode and Nyquist plots of the HAp-coated samples measured at 0.5 h after immersion in Hanks' solution. The phase shift spectra in the Bode plots of all the samples showed the existence of two time constants because the phase shift spectra showed maximum peaks at around 10^3 Hz and at around 10^0-10^1 Hz. The Nyquist plot of the Ac-1Zn/HAp showed two capacitive loops and the plots of the Ac-5Zn/HAp, Ac-7Zn/HAp and T4-7Zn/HAp showed two capacitive loops and one inductive loop. Then, two types of equivalent electric circuits shown in Figure 4.13 [49,50] were assumed for the HAp-coated samples with and without an inductive loop, respectively, and curve fitting was performed. R_s represents the solution resistance. R_{ct} and CPE_{dl} represents the charge transfer resistance and the constant phase element of electric double layer, respectively. Here, the constant phase element was used instead of the capacitance due to the non-homogeneity of the system. R_c and C_c represent the resistance and capacity of the HAp coating, respectively. R_L and L represent the resistance and inductance of the inductive loop. According to King et al. and Li et al., the polarization

resistance (R_p) in the equivalent electric circuits shown in Fig. 4.13(a) and (b) was estimated using the equation (7) and (8), respectively [49,50]:

$$\frac{1}{R_p} = \frac{1}{R_{ct}+R_c} \tag{4.7}$$

$$\frac{1}{R_p} = \frac{1}{R_{ct}+R_c} + \frac{1}{R_L} \tag{4.8}$$

The fitting curves were presented in Fig. 4.12 as solid lines and the fitted values of the parameters are listed in Table 4.5. The R_p values implied the corrosion resistance of the sample. The R_p value of the Ac-1Zn/HAp was the highest, indicating the highest corrosion resistance among all the HAp-coated samples. It should be noted that the R_p value of the Ac-1Zn/HAp was 17-100 times higher that of the other samples. The Ac-1Zn/HAp showed the R_c value 12-50 times higher than other samples. The highest R_c value of the Ac-1Zn/HAp was attributed to the defect-free HAp coating. The Ac-5Zn/HAp having the defect-less HAp coating showed the second highest value. The low R_c values of the Ac-7Zn/HAp and T4-7Zn/HAp were attributed to the obvious defects of the coatings which allowed the permeation of solution to the alloy substrate. The result suggested that the uniformity of the HAp coating dominated the R_p and R_c values of the HAp-coated sample.

Figure 4.14 shows the time dependence of the R_p of the HAp-coated samples. The Ac-1Zn/HAp showed the highest and almost constant R_p value at about 2.8×10^5 $\Omega\cdot cm^2$ at all the measurement times. This result demonstrated the stable and high corrosion protectiveness of the HAp coating. The R_p of the Ac-5Zn/HAp rapidly decreased in the initial 0.5 h and then gradually decreased through 6 h of measurement period. The R_p of the Ac-7Zn/HAp rapidly decreased below 1×10^4 $\Omega\cdot cm^2$ in 0.5 h and became constant afterwards. The decrease in R_p value was attributed to the initiation of corrosion from the defects of the HAp coating. The R_p of the T4-7Zn/HAp decreased rapidly in the initial 0.5 h, then the R_p increased gradually to about 1×10^4 $\Omega\cdot cm^2$ at 6 h. The increase in R_p value was due to the deposition of corrosion products covering defects of the HAp coating.

(5) Effect of HAp coating on the corrosion of Mg-Zn alloys in Hanks' solution

The 14-day average corrosion rates of the HAp-coated Mg-Zn alloys were lower than those of the uncoated Mg-Zn alloys [21] as mentioned in Section 4.3.2.1. A clear quasi-passive region appeared on the anodic polarization curves of the Ac-1Zn/HAp and Ac-5Zn/HAp, while such a clear quasi-passive region was not observed for the uncoated Ac-1Zn and Ac-5Zn alloys [21]. The R_p values at 0.5 h EIS measurement of the uncoated Mg-Zn alloys were referred from the previous study [21] and summarized in Table 4.5. The R_p value at 0.5 h EIS measurement of the Ac-1Zn/HAp, Ac-5Zn/HAp and Ac-7Zn/HAp was 10, 7.5 and 5 times higher than that of the uncoated Ac-1Zn, Ac-5Zn and Ac-7Zn alloys, respectively. These facts revealed that the HAp coating was effective to retard the corrosion rate of Mg-Zn alloys. It was also revealed that the magnitude of the corrosion protection effect of the HAp coatings depended on the composition and microstructure of Mg-Zn alloys.

Figure 4.15 shows the schematic illustrations of the corrosion mechanism of the Ac-1Zn/HAp, Ac-7Zn/HAp and T4-7Zn/HAp in Hanks' solution. The generation frequency and size of defects in the HAp coating, i.e. uniformity of the HAp coating, depended on the microstructure of substrate Mg-Zn alloys. With an increase of the volume fraction and particle size of (α-Mg + MgZn) eutectic cells, the cracking of the HAp coating increased (Fig. 4.2 and 4.4). As the result, the corrosion protectiveness of the as-prepared HAp coatings initially depended on the microstructure of the substrate Mg-Zn alloys in Hanks' solution. In Hanks' solution, the corrosion of substrate Mg-Zn alloys induced HAp and $Mg(OH)_2$ deposition owing to pH increase (Fig. 4.9 and 4.10). The deposited HAp and $Mg(OH)_2$ can fill or cover the defects of the HAp coating. When the volume fraction of Zn-rich phases of the substrate alloy is low, the defect-free HAp coating shows high corrosion resistance for a long period of time and the deposition of HAp from the solution improves the protectiveness of the coating as shown in Fig. 4.15(a) and (b). However, when the volume fraction of Zn-rich phases of the substrate alloy is high, the corrosion progress of substrate Mg-Zn exceeds the repair of the coating defects and the HAp coating is broken down. Afterward, the corrosion rate of the HAp-coated Mg-Zn alloy is governed by the corrosion property of the substrate Mg-Zn alloys as shown in Fig. 4.15(c-f). To continue the effect of the HAp coating on the Mg-Zn alloys with large volume fraction of Zn-rich phases, further improvement of the HAp coating is necessary to reduce the coating defect.

4.4 Conclusions

The HAp coatings were formed on the Mg-Zn alloys by the simple solution treatment. The effect of the substrate microstructure on the characteristics of the HAp coatings was examined and the corrosion behavior of the HAp-coated alloys was examined by static immersion test, polarization and EIS tests in Hanks' solution. The following conclusions were given:

(1) The HAp coatings were formed on the Mg-Zn alloys with the two-layer structure. The uniformity of the HAp coatings significantly depended on the volume fraction and the particle size of (α-Mg + MgZn) eutectic cells of the substrates. The micro-galvanic corrosion at the (α-Mg + MgZn) cells generated $Mg(OH)_2$ and H_2 gas which caused cracking and slight delamination of the HAp layers. The defect-free uniform HAp coating was formed on the Ac-1Zn alloy with the lowest volume fraction of Zn-rich phases.

(2) The corrosion behavior of the HAp-coated Mg-Zn alloys was governed by the volume fraction and size of Zn-rich phases. In the initial stage of immersion, the uniformity of the HAp coating governed the corrosion rate of the alloys. The Ac-1Zn/HAp showed 2-4 times lower corrosion rate than the other coated alloys after 1 day of immersion. After the HAp coatings were irreversibly broken, the corrosion resistance of the HAp-coated alloys was dominated by the corrosion property of the substrate alloys. After 14 days, the Ac-1Zn/HAp showed 4-10 times lower corrosion rate than the other samples.

(3) The 14-day average corrosion rate of the Ac-1Zn, Ac-5Zn and Ac-7Zn alloys decreased by 45%, 5% and 15% with the HAp coatings, respectively. The R_p values at 0.5-h EIS measurement of the Ac-1Zn, Ac-5Zn and Ac-7Zn alloys increased by 10, 7.5 and 5 times with the HAp coatings, respectively. The HAp coating effect on the corrosion behavior of the T4-7Zn alloy was not significant. It was revealed that the HAp coating is effective for the Mg-Zn alloys with low volume fraction and fine particle size of Zn-rich phases to improve the corrosion resistance.

4.5 References

[1] M.P. Staiger, A.M. Pietak, J. Huadmai, G. Dias, Magnesium and its alloys as orthopedic biomaterials: A review, Biomaterials. 27 (2006) 1728–1734. https://doi.org/10.1016/j.biomaterials.2005.10.003.

[2] S. Agarwal, J. Curtin, B. Duffy, S. Jaiswal, Biodegradable magnesium alloys for orthopaedic applications: A review on corrosion, biocompatibility and surface modifications, Mater. Sci. Eng. C. 68 (2016) 948–963. https://doi.org/10.1016/j.msec.2016.06.020.

[3] F. Witte, The history of biodegradable magnesium implants: A review, Acta Biomater. 6 (2010) 1680–1692. https://doi.org/10.1016/j.actbio.2010.02.028.

[4] Y.F. Zheng, X.N. Gu, F. Witte, Biodegradable metals, Mater. Sci. Eng. R. 77 (2014) 1–34. https://doi.org/10.3390/met8100804.

[5] G. Song, A. Atrens, Understanding magnesium corrosion. A framework for improved alloy performance, Adv. Eng. Mater. 5 (2003) 837–858. https://doi.org/10.1002/adem.200310405.

[6] M.I. Rahim, S. Ullah, P.P. Mueller, Advances and challenges of biodegradable implant materials with a focus on magnesium-alloys and bacterial infections, Metals (Basel). 8 (2018) 532. https://doi.org/10.3390/met8070532.

[7] G. Song, Control of biodegradation of biocompatable magnesium alloys, Corros. Sci. 49 (2007) 1696–1701. https://doi.org/10.1016/j.corsci.2007.01.001.

[8] X. Gu, Y. Zheng, Y. Cheng, S. Zhong, T. Xi, In vitro corrosion and biocompatibility of binary magnesium alloys, Biomaterials. 30 (2009) 484–498. https://doi.org/10.1016/j.biomaterials.2008.10.021.

[9] X. Li, X. Liu, S. Wu, K.W.K. Yeung, Y. Zheng, P.K. Chu, Design of magnesium alloys with controllable degradation for biomedical implants: From bulk to surface, Acta Biomater. 45 (2016) 2–30. https://doi.org/10.1016/j.actbio.2016.09.005.

[10] F. Cao, Z. Shi, G.L. Song, M. Liu, A. Atrens, Corrosion behaviour in salt spray and in 3.5% NaCl solution saturated with Mg(OH)2 of as-cast and solution heat-treated binary Mg-X alloys: X=Mn, Sn, Ca, Zn, Al, Zr, Si, Sr, Corros. Sci. 76 (2013) 60–97. https://doi.org/10.1016/j.corsci.2013.06.030.

[11] J.E. Gray, B. Luan, Protective coatings on magnesium and its alloys - A critical review, J. Alloys Compd. 336 (2002) 88–113. https://doi.org/10.1016/S0925-8388(01)01899-0.

[12] H. Hornberger, S. Virtanen, A.R. Boccaccini, Biomedical coatings on magnesium alloys – A review, Acta Biomater. 8 (2012) 2442–2455. https://doi.org/10.1016/j.actbio.2012.04.012.

[13] F. Feyerabend, J. Fischer, J. Holtz, F. Witte, R. Willumeit, H. Drücker, C. Vogt, N. Hort, Evaluation of short-term effects of rare earth and other elements used in magnesium alloys on primary cells and cell lines, Acta Biomater. 6 (2010) 1834–1842. https://doi.org/10.1016/j.actbio.2009.09.024.

[14] S.S. Abd El-Rahman, Neuropathology of aluminum toxicity in rats (glutamate and GABA impairment), Pharmacol. Res. 47 (2003) 189–194. https://doi.org/10.1016/S1043-6618(02)00336-5.

[15] C.H. Ku, D.P. Pioletti, M. Browne, P.J. Gregson, Effect of different Ti-6Al-4V surface treatments on osteoblasts behaviour, Biomaterials. 23 (2002) 1447–1454. https://doi.org/10.1016/S0142-9612(01)00266-6.

[16] Y. Nakamura, Y. Tsumura, Y. Tonogai, T. Shibata, Y. Ito, Differences in behavior among the chlorides of seven rare earth elements administered intravenously to rats, Fundam. Appl. Toxicol. 37 (1997) 106–116. https://doi.org/10.1006/faat.1997.2322.

[17] E. Koç, M.B. Kannan, M. Ünal, E. Candan, Influence of zinc on the microstructure, mechanical properties and in vitro corrosion behavior of magnesium-zinc binary alloys, J. Alloys Compd. 648 (2015) 291–296. https://doi.org/10.1016/j.jallcom.2015.06.227.

[18] Y. Yan, H. Cao, Y. Kang, K. Yu, T. Xiao, J. Luo, Y. Deng, H. Fang, H. Xiong, Y. Dai, Effects of Zn concentration and heat treatment on the microstructure, mechanical properties and corrosion behavior of as-extruded Mg-Zn alloys produced by powder metallurgy, J. Alloys Compd. 693 (2017) 1277–1289. https://doi.org/10.1016/j.jallcom.2016.10.017.

[19] Y. Song, E.H. Han, D. Shan, C.D. Yim, B.S. You, The role of second phases in the corrosion behavior of Mg-5Zn alloy, Corros. Sci. 60 (2012) 238–245. https://doi.org/10.1016/j.corsci.2012.03.030.

[20] Y. Lu, A.R. Bradshaw, Y.L. Chiu, I.P. Jones, The role of β′ precipitates in the bio-

corrosion performance of Mg-3Zn in simulated body fluid, J. Alloys Compd. 614 (2014) 345–352. https://doi.org/10.1016/j.jallcom.2014.06.078.

[21] D. Pham, S. Hiromoto, E. Kobayashi, Influences of Zinc Content and Solution Heat Treatment on Microstructure and Corrosion Behavior of Mg-Zn Binary Alloys, Corrosion. 77 (2021) 323–338. https://doi.org/10.5006/3672.

[22] J. Kuhlmann, I. Bartsch, E. Willbold, S. Schuchardt, O. Holz, N. Hort, D. Höche, W.R. Heineman, F. Witte, Fast escape of hydrogen from gas cavities around corroding magnesium implants, Acta Biomater. 9 (2013) 8714–8721. https://doi.org/10.1016/j.actbio.2012.10.008.

[23] T. Kraus, S.F. Fischerauer, A.C. Hänzi, P.J. Uggowitzer, J.F. Löffler, A.M. Weinberg, Magnesium alloys for temporary implants in osteosynthesis : In vivo studies of their degradation and interaction with bone, Acta Biomater. 8 (2012) 1230–1238. https://doi.org/10.1016/j.actbio.2011.11.008.

[24] D. Noviana, D. Paramitha, M.F. Ulum, H. Hermawan, The effect of hydrogen gas evolution of magnesium implant on the postimplantation mortality of rats, J. Orthop. Transl. 5 (2016) 9–15. https://doi.org/10.1016/j.jot.2015.08.003.

[25] G. Wu, J.M. Ibrahim, P.K. Chu, Surface design of biodegradable magnesium alloys - A review, Surf. Coatings Technol. 233 (2013) 2–12. https://doi.org/10.1016/j.surfcoat.2012.10.009.

[26] K.J.L. Burg, S. Porter, J.F. Kellam, Biomaterial developments for bone tissue engineering, Biomaterials. 21 (2000) 2347–2359. https://doi.org/10.1016/S0142-9612(00)00102-2.

[27] H. Zhou, J. Lee, Nanoscale hydroxyapatite particles for bone tissue engineering, Acta Biomater. 7 (2011) 2769–2781. https://doi.org/10.1016/j.actbio.2011.03.019.

[28] X. Liu, P.K. Chu, C. Ding, Surface modification of titanium, titanium alloys, and related materials for biomedical applications, Mater. Sci. Eng. R Reports. 47 (2004) 49–121. https://doi.org/10.1016/j.mser.2004.11.001.

[29] N.Q. Cao, H.M. Le, K.M. Pham, N. V Nguyen, S. Hiromoto, In Vitro Corrosion and Cell Response of Hydroxyapatite Coated Mg Matrix in Situ Composites, Materials (Basel). 12 (2019) 3474.

[30] S. Hiromoto, M. Tomozawa, Hydroxyapatite coating of AZ31 magnesium alloy by a solution treatment and its corrosion behavior in NaCl solution, Surf. Coat. Technol. 205 (2011) 4711–4719. https://doi.org/10.1016/j.surfcoat.2011.04.036.

[31] H. Zhou, J. Li, J. Li, Q. Ruan, W. Jin, Z. Yu, W. Li, P.K. Chu, Calcium phosphate coating on biomedical WE43 magnesium alloy pretreated with a magnesium phosphate layer for corrosion protection, Surf. Coatings Technol. 401 (2020) 126248. https://doi.org/10.1016/j.surfcoat.2020.126248.

[32] Y. Guo, Y. Su, R. Gu, Z. Zhang, G. Li, J. Lian, L. Ren, Enhanced corrosion resistance and biocompatibility of biodegradable magnesium alloy modified by calcium phosphate / collagen coating, Surf. Coat. Technol. 401 (2020) 126318. https://doi.org/10.1016/j.surfcoat.2020.126318.

[33] S. Hiromoto, T. Yamazaki, Micromorphological effect of calcium phosphate coating on compatibility of magnesium alloy with osteoblast, Sci. Technol. Adv. Mater. 18 (2017) 96–109. https://doi.org/10.1080/14686996.2016.1266238.

[34] S. Hiromoto, A. Yamamoto, High corrosion resistance of magnesium coated with hydroxyapatite directly synthesized in an aqueous solution, Electrochim. Acta. 54 (2009) 7085–7093. https://doi.org/10.1016/j.electacta.2009.07.033.

[35] R.I.M. Asri, W.S.W. Harun, M.A. Hassan, S.A.C. Ghani, Z. Buyong, A review of hydroxyapatite-based coating techniques: Sol-gel and electrochemical depositions on biocompatible metals, J. Mech. Behav. Biomed. Mater. 57 (2016) 95–108. https://doi.org/10.1016/j.jmbbm.2015.11.031.

[36] Y.W. Song, D.Y. Shan, E.H. Han, Electrodeposition of hydroxyapatite coating on AZ91D magnesium alloy for biomaterial application, Mater. Lett. 62 (2008) 3276–3279. https://doi.org/10.1016/j.matlet.2008.02.048.

[37] M. Tomozawa, S. Hiromoto, Growth mechanism of hydroxyapatite-coatings formed on pure magnesium and corrosion behavior of the coated magnesium, Appl. Surf. Sci. 257 (2011) 8253–8257. https://doi.org/10.1016/j.apsusc.2011.04.087.

[38] S. Hiromoto, E. Nozoe, K. Hanada, T. Yoshimura, K. Shima, T. Kibe, N. Nakamura, K. Doi, In vivo degradation and bone formation behaviors of hydroxyapatite-coated Mg alloys in rat femur, Mater. Sci. Eng. C. 122 (2021). https://doi.org/10.1016/j.msec.2021.111942.

[39] H. Watanabe, H. Tanaka, Dual-wavelength spectrophotometric determination of magnesium (ii) with xylidyl blue I and nonionic surfactant, Bunseki Kagaku. 26 (1977) 635–639. https://doi.org/10.2116/bunsekikagaku.26.9_635.

[40] C.K. Mann, J.H. Yoe, Spectrophotometric determination of magnesium with sodium 1-azo-2-hydroxy-3-(2,4-dimethylcarboxanilido)-naphthalene-1′-(2-hydroxybenzene-5-sulfonate), Anal. Chem. 28 (1956) 202–205. https://doi.org/10.1021/ac60110a016.

[41] S. Hiromoto, A. Yamamoto, Control of degradation rate of bioabsorbable magnesium by anodization and steam treatment, Mater. Sci. Eng. C. 30 (2010) 1085–1093. https://doi.org/10.1016/j.msec.2010.06.001.

[42] M. Tomozawa, S. Hiromoto, Y. Harada, Microstructure of hydroxyapatite-coated magnesium prepared in aqueous solution, Surf. Coatings Technol. 204 (2010) 3243–3247. https://doi.org/10.1016/j.surfcoat.2010.03.023.

[43] M. Tomozawa, S. Hiromoto, Microstructure of hydroxyapatite- and octacalcium phosphate-coatings formed on magnesium by a hydrothermal treatment at various pH values, Acta Mater. 59 (2011) 355–363. https://doi.org/10.1016/j.actamat.2010.09.041.

[44] C. Liu, J. Liang, J. Zhou, Q. Li, L. Wang, Characterization of AZ31 magnesium alloy by duplex process combining laser surface melting and plasma electrolytic oxidation, Appl. Surf. Sci. 382 (2016) 47–55. https://doi.org/10.1016/j.apsusc.2016.04.047.

[45] H. Kuwahara, Y. Al-Abdullat, N. Mazaki, S. Tsutsumi, T. Aizawa, Preparation of Magnesium Apatite on Pure Magnesium Surface during Immersing in Hank, Mater. Trans. 42 (2001) 1317 to 1321.

[46] S. Hiromoto, M. Tomozawa, Corrosion behavior of magnesium with hydroxyapatite coatings formed by hydrothermal treatment, Mater. Trans. 51 (2010) 2080–2087. https://doi.org/10.2320/matertrans.M2010192.

[47] A. Srinivasan, K.S. Shin, N. Rajendran, Dynamic electrochemical impedance spectroscopy (DEIS) studies of AZ31 magnesium alloy in simulated body fluid solution, RSC Adv. 4 (2014) 27791–27795. https://doi.org/10.1039/c4ra02432j.

[48] L. Wang, T. Shinohara, B.P. Zhang, Influence of deaerated condition on the corrosion behavior of AZ31 magnesium alloy in dilute NaCl solutions, Mater. Trans. 50 (2009) 2563–2569. https://doi.org/10.2320/matertrans.M2009191.

[49] A.D. King, N. Birbilis, J.R. Scully, Accurate Electrochemical Measurement of Magnesium Corrosion Rates; a Combined Impedance, Mass-Loss and Hydrogen Collection Study, Electrochim. Acta. 121 (2014) 394–406. https://doi.org/10.1016/j.electacta.2013.12.124.

[50] Q. Li, W. Ye, H. Gao, L. Gao, Improving the corrosion resistance of ZEK100 magnesium alloy by combining high-pressure torsion technology with hydroxyapatite coating, Mater. Des. 181 (2019) 107933. https://doi.org/10.1016/j.matdes.2019.107933.

Table 4.1 Composition and preparation condition of the samples

Sample name	Composition (C / wt%)	Preparation condition
Ac-1Zn	Mg-1%Zn	As-cast alloy
Ac-5Zn	Mg-5%Zn	As-cast alloy
Ac-7Zn	Mg-7%Zn	As-cast alloy
T4-7Zn	Mg-7%Zn	T4-treated alloy
Ac-1Zn/HAp	Mg-1%Zn	As-cast alloy, HAp coated
Ac-5Zn/HAp	Mg-5%Zn	As-cast alloy, HAp coated
Ac-7Zn/HAp	Mg-7%Zn	As-cast alloy, HAp coated
T4-7Zn/HAp	Mg-7%Zn	T4-treated alloy, HAp coated

Table 4.2 Components of Hanks' solution

Reagent	NaCl	KCl	$Na_2HPO_4.H_2O$	KH_2PO_4	$MgSO_4.7H_2O$	$NaHCO_3$	$CaCl_2$
Concentration, g / L	8.00	0.40	0.06	0.06	0.20	0.35	0.14

Table 4.3 14-day average Mg^{2+} ion release rate of uncoated and HAp-coated Mg-Zn alloys in Hanks' solution

Samples	Ac-1Zn	Ac-5Zn	Ac-7Zn	T4-7Zn	Ac-1Zn /HAp	Ac-5Zn /HAp	Ac-7Zn /HAp	T4-7Zn /HAp
Mg^{2+} ion release rate ($mg \cdot cm^{-2} \cdot d^{-1}$)	0.028 ± 0.006	0.098 ± 0.029	0.281 ± 0.013	0.040 ± 0.015	0.015 ± 0.004	0.093 ± 0.021	0.241 ± 0.017	0.043 ± 0.005

Table 4.4 Composition at the points marked on the cross-section images of samples after immersion in Hanks' solution for 14 days

	Spot number	Concentration (C / at%)							Ca/P ratio
		C	O	Na	Mg	P	Ca	Zn	
Ac-1Zn/HAp	#1	16.19	56.51	0.89	1.67	10.54	14.20	0	1.35
	#2	3.77	51.60	1.45	8.73	15.07	19.39	0	1.29
	#3	2.85	37.40	0	46.49	7.45	5.70	0.10	—
Ac-7Zn/HAp	#1	8.93	60.25	1.63	2.94	11.56	14.70	0	1.27
	#2	8.63	57.04	0	4.45	13.36	16.27	0.25	1.21
	#3	3.59	48.19	0	32.31	7.56	7.98	0.38	—
T4-7Zn/HAp	#1	3.81	63.64	0	3.02	11.99	17.41	0.13	1.45
	#2	5.46	52.46	0	3.68	16.20	21.93	0.27	1.35
	#3	1.69	55.49	0	41.26	0.25	0.12	1.19	—

Table 4.5 Fitting results of the EIS spectra measured at 0.5 h of the HAp-coated and uncoated Mg-Zn alloys

	R_s ($\Omega \cdot cm^2$)	CPE_{dl}-T ($\mu F \cdot cm^{-2}$)	n	R_{ct} ($\Omega \cdot cm^2$)	C_c ($\mu F \cdot cm^{-2}$)	R_c ($\Omega \cdot cm^2$)	L ($\Omega \cdot s \cdot cm^2$)	R_L ($\Omega \cdot cm^2$)	R_P ($\Omega \cdot cm^2$)
Ac-1Zn /HAp	42.52	11.32	0.641	16357	1.364	265100	–	–	281457
Ac-5Zn /HAp	41.28	11.46	0.629	9015	3.834	21576	139030	35472	16426
Ac-7Zn /HAp	69.65	13.97	0.618	5828	5.540	5382	63568	8803	4931
T4-7Zn /HAp	32.87	9.209	0.683	4916	4.911	6138	26448	3456	2633
Ac-1Zn	40.15	13.33	0.715	558.4	2.066	31666	105900	10650	24700
Ac-5Zn	31.79	14.10	0.670	284.9	2.817	3687	2916	4577	2130
Ac-7Zn	58.79	13.51	0.675	249.8	1.735	2749	2205	1576	1030
T4-7Zn	53.98	38.26	0.708	485.4	1.324	3062	815.5	19672	3010

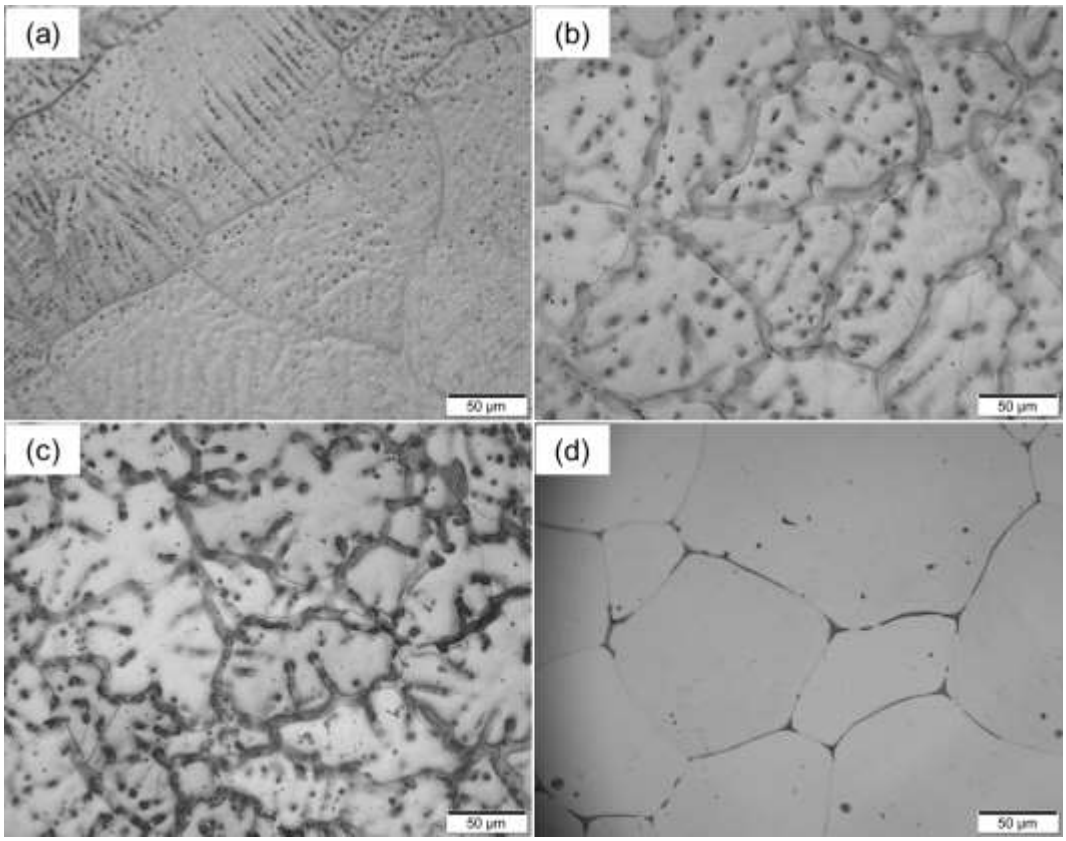

Figure 4.1 Optical metallographic images of the uncoated (a) Ac-1Zn, (b) Ac-5Zn, (c) Ac-7Zn and (d) T4-7Zn alloys

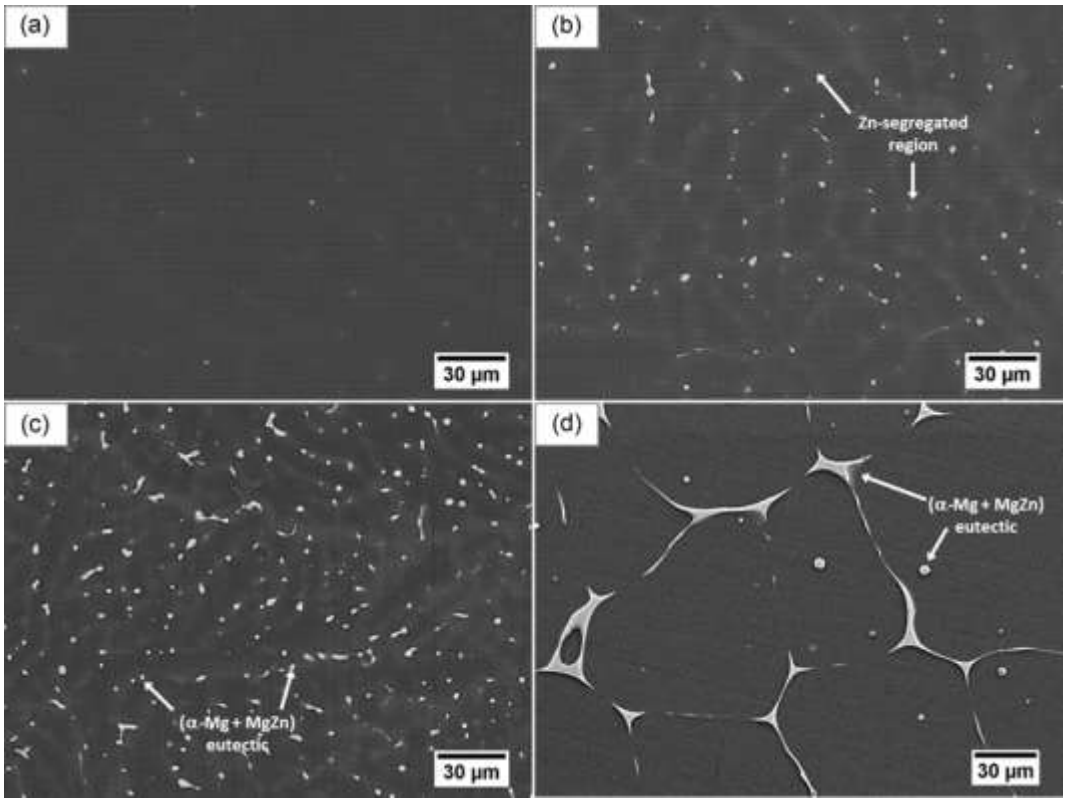

Figure 4.2 SEM microstructure images of the uncoated (a) Ac-1Zn, (b) Ac-5Zn, (c) Ac-7Zn and (d) T4-7Zn alloys

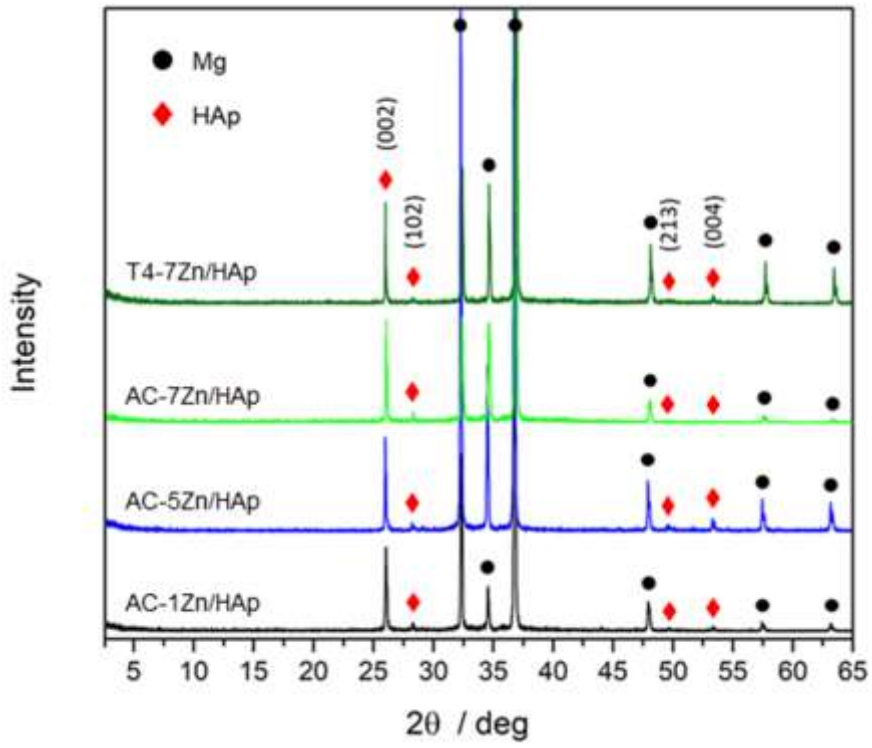

Figure 4.3 XRD patterns of the HAp-coated samples

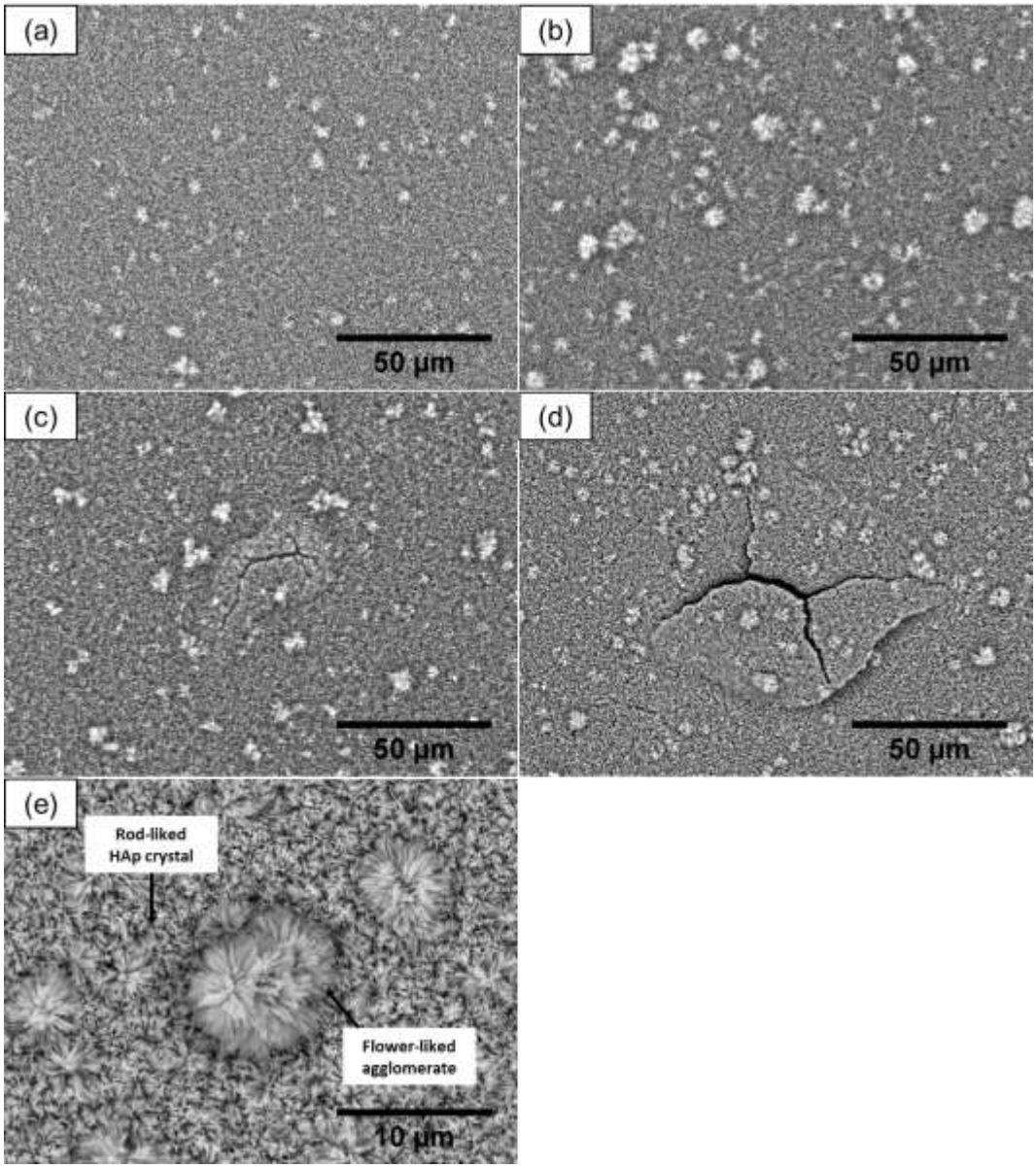

Figure 4.4 SEM surface images of the as-coated (a) Ac-1Zn/HAp, (b) Ac-5Zn/HAp, (c) Ac-7Zn/HAp, and (d) T4-7Zn/HAp and (e) magnified image of flower-like agglomerates of HAp rod crystals

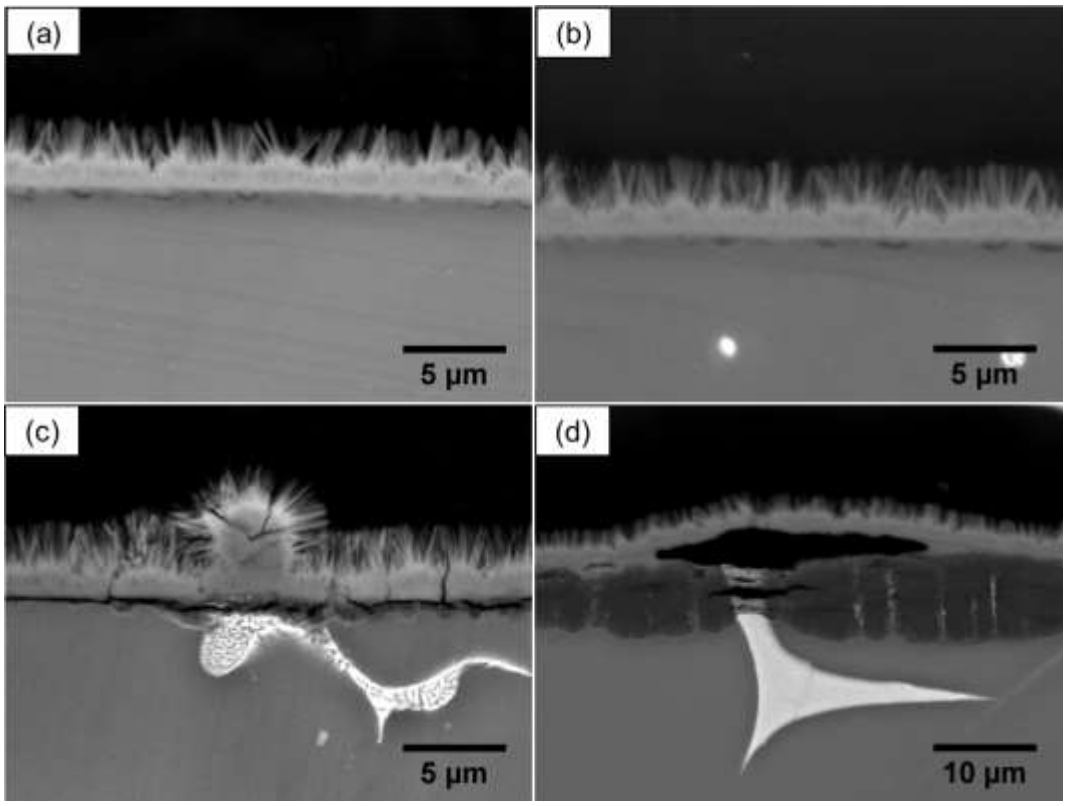

Figure 4.5 SEM cross-sectional images of the as-coated (a) Ac-1Zn/HAp, (b) Ac-5Zn/HAp, (c) Ac-7Zn/HAp and (d) T4-7Zn/HAp

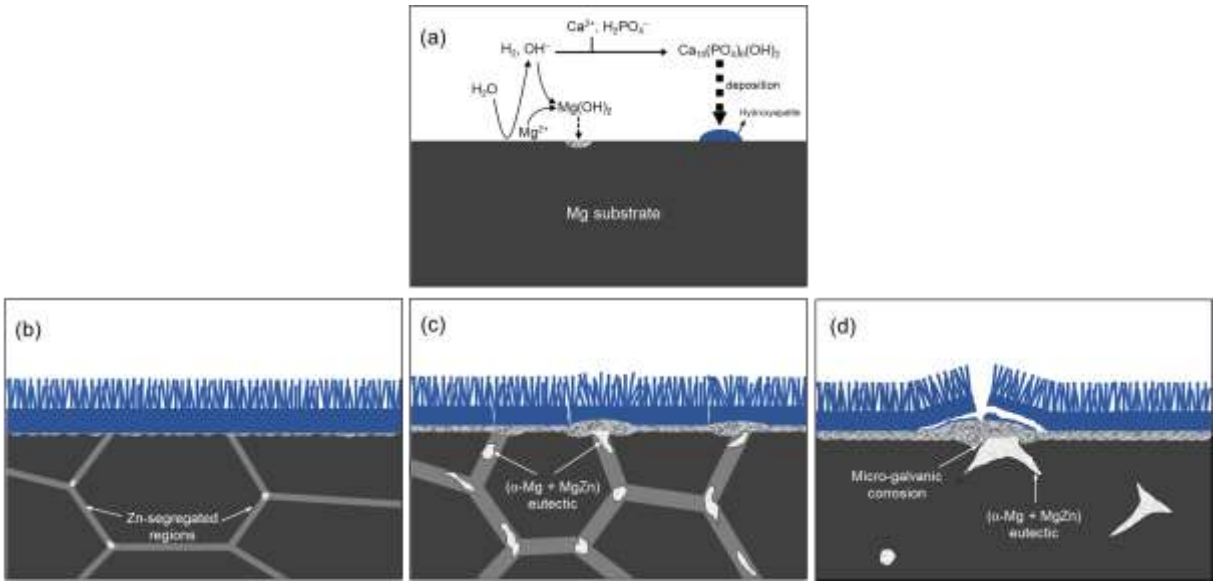

Figure 4.6 Schematic illustration of (a) the coating mechanism of HAp by chemical solution deposition treatment, and the HAp coating morphology of (b) Ac-1Zn/HAp, (c) Ac-7Zn/HAp and (d) T4-7Zn/HAp

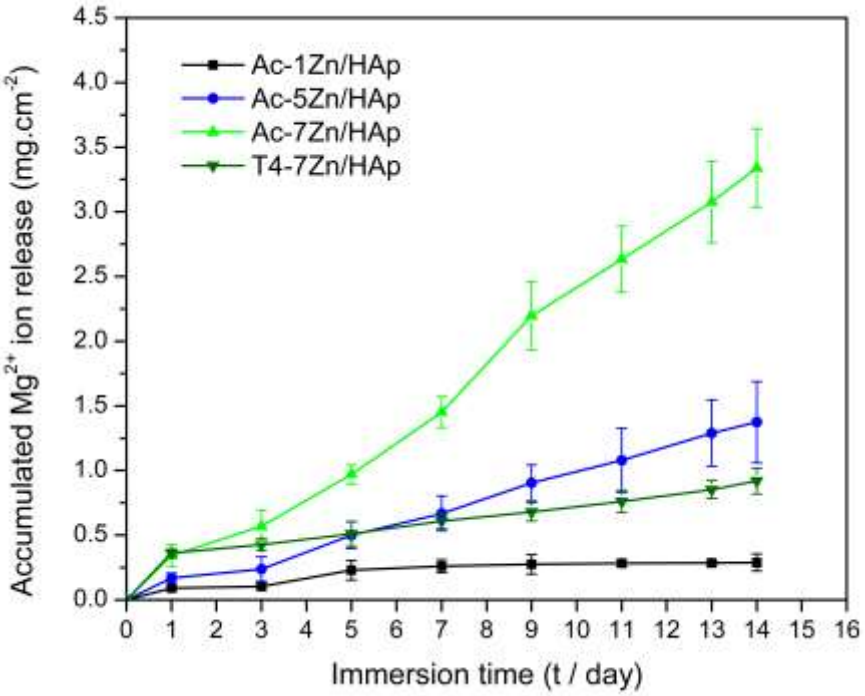

Figure 4.7 Mg^{2+} ions release of the HAp-coated samples as a function of immersion time in Hanks' solution

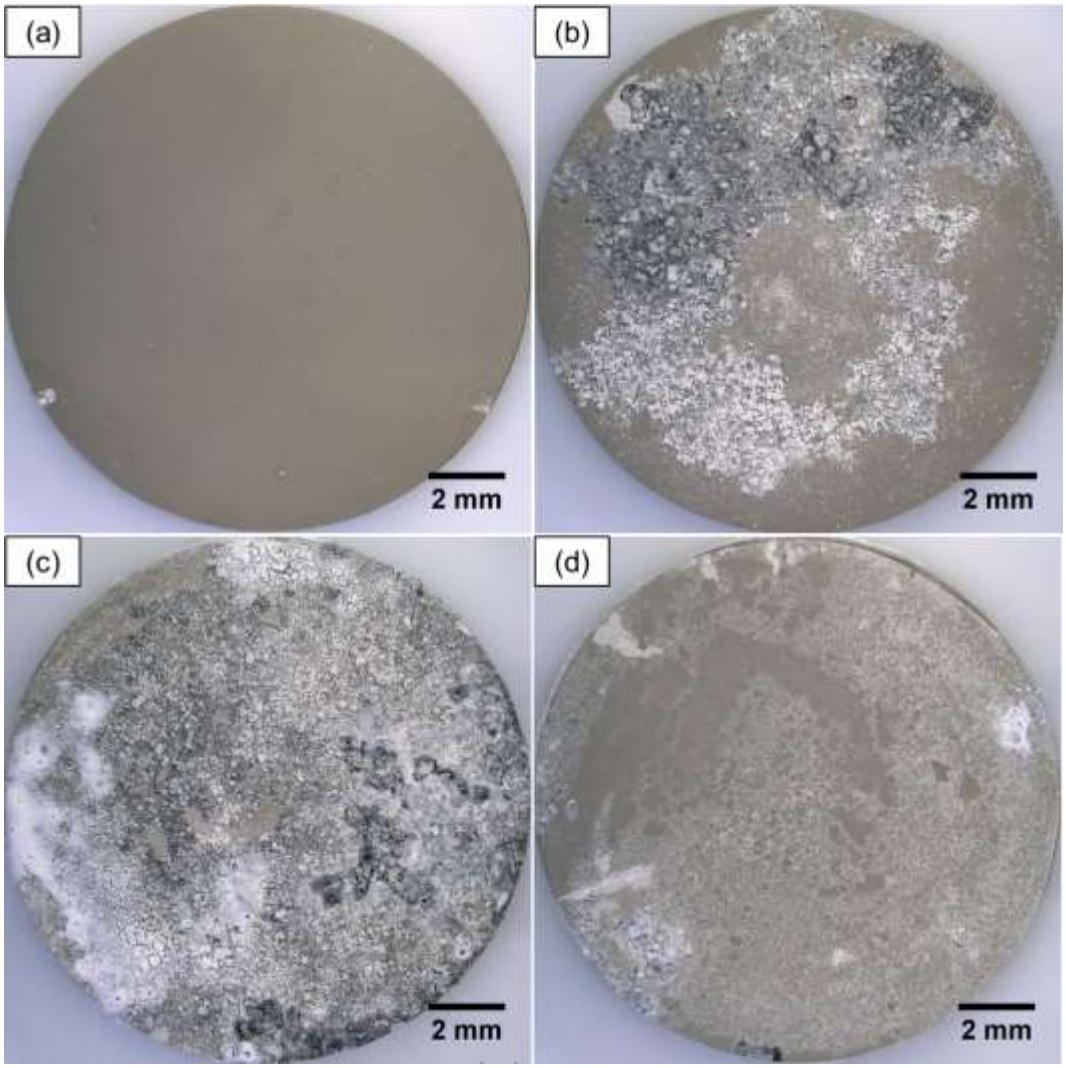

Figure 4.8 Optical surface images of (a) Ac-1Zn/HAp, (b) Ac-5Zn/HAp, (c) Ac-7Zn/HAp and (d) T4-7Zn/HAp after immersion in Hanks' solution for 14 days

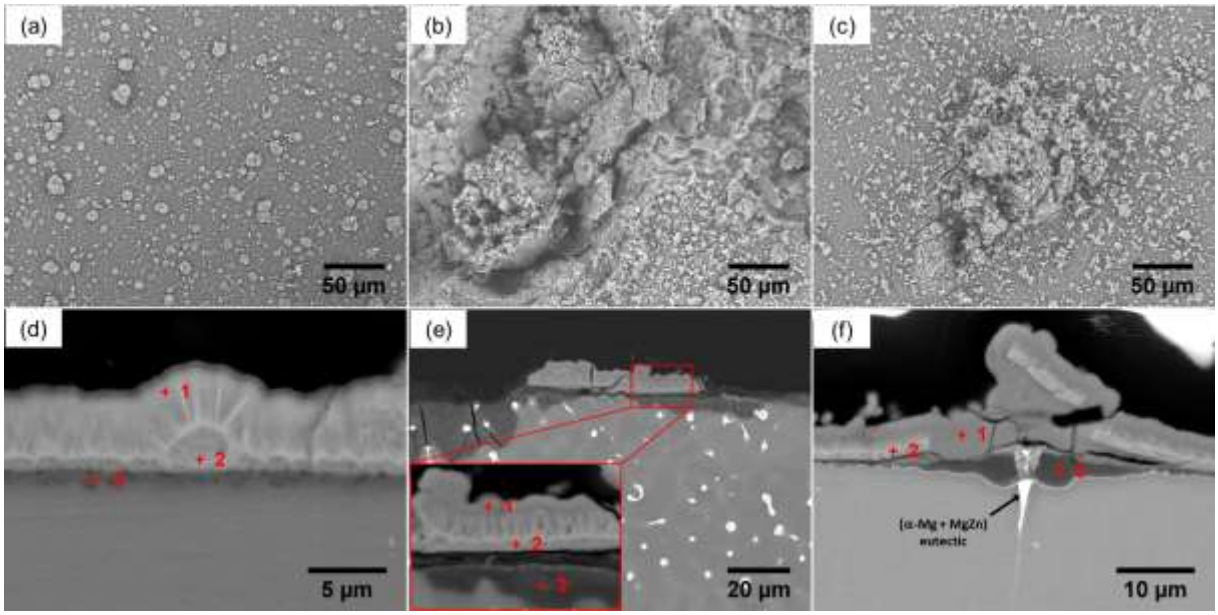

Figure 4.9 SEM images of surface and cross-section of (a, d) Ac-1Zn/HAp, (b, e) Ac-7Zn/HAp and (c, f) T4-7Zn/HAp after immersion in Hanks' solution for 14 days

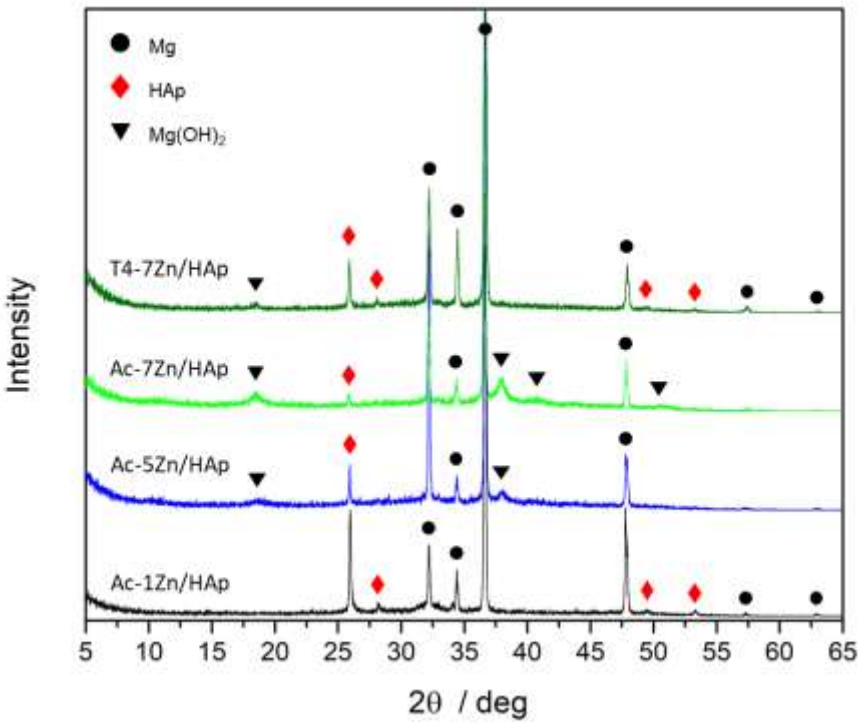

Figure 4.10 XRD patterns of HAp-coated samples after immersion in Hanks' solution for 14 days

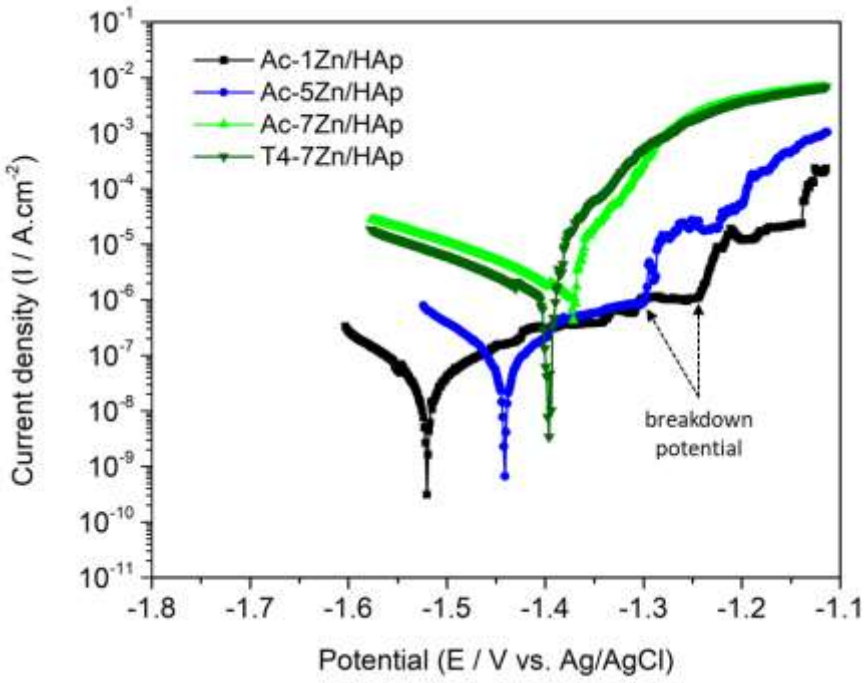

Figure 4.11 Polarization curves of HAp-coated samples in Hanks' solution

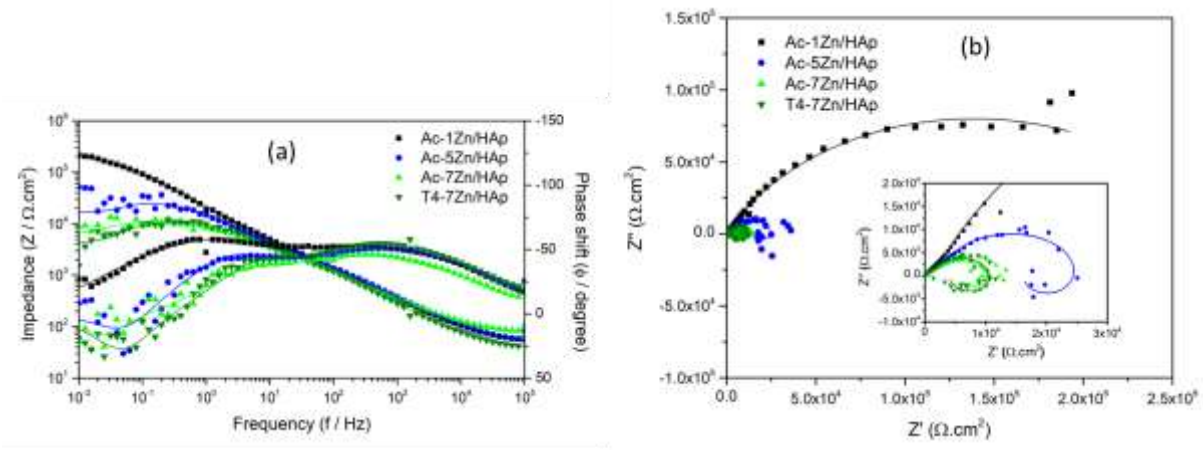

Figure 4.12 EIS plots of HAp-coated samples (a) Bode plots and (b) Nyquist plots. Scatter symbols are experimental data and solid lines are fitting data

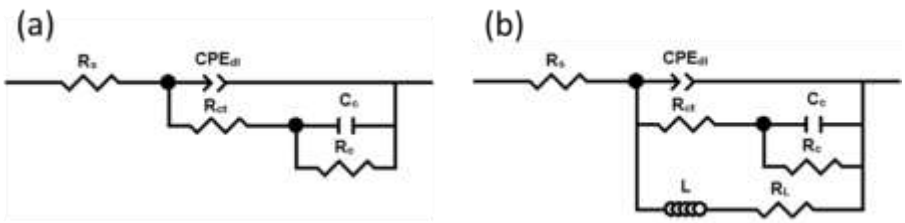

Figure 4.13 Equivalent electric circuits for (a) Ac-1Zn/HAp and (b) Ac-5Zn/HAp, Ac-7Zn/HAp and T4-7Zn/HAp

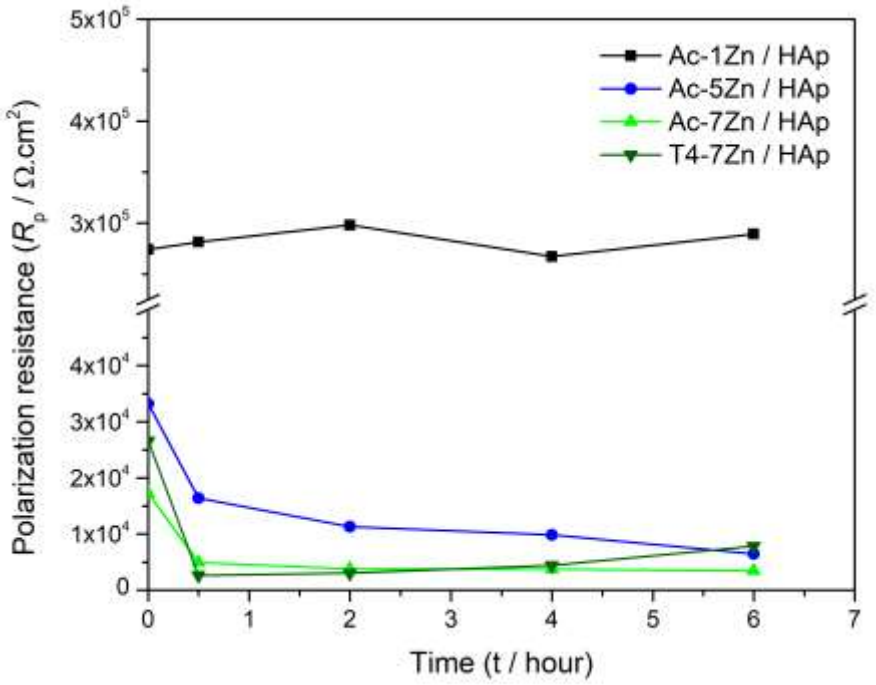

Figure 4.14 Time dependence of polarization resistance R_p of HAp-coated Mg-Zn alloys in Hanks' solution

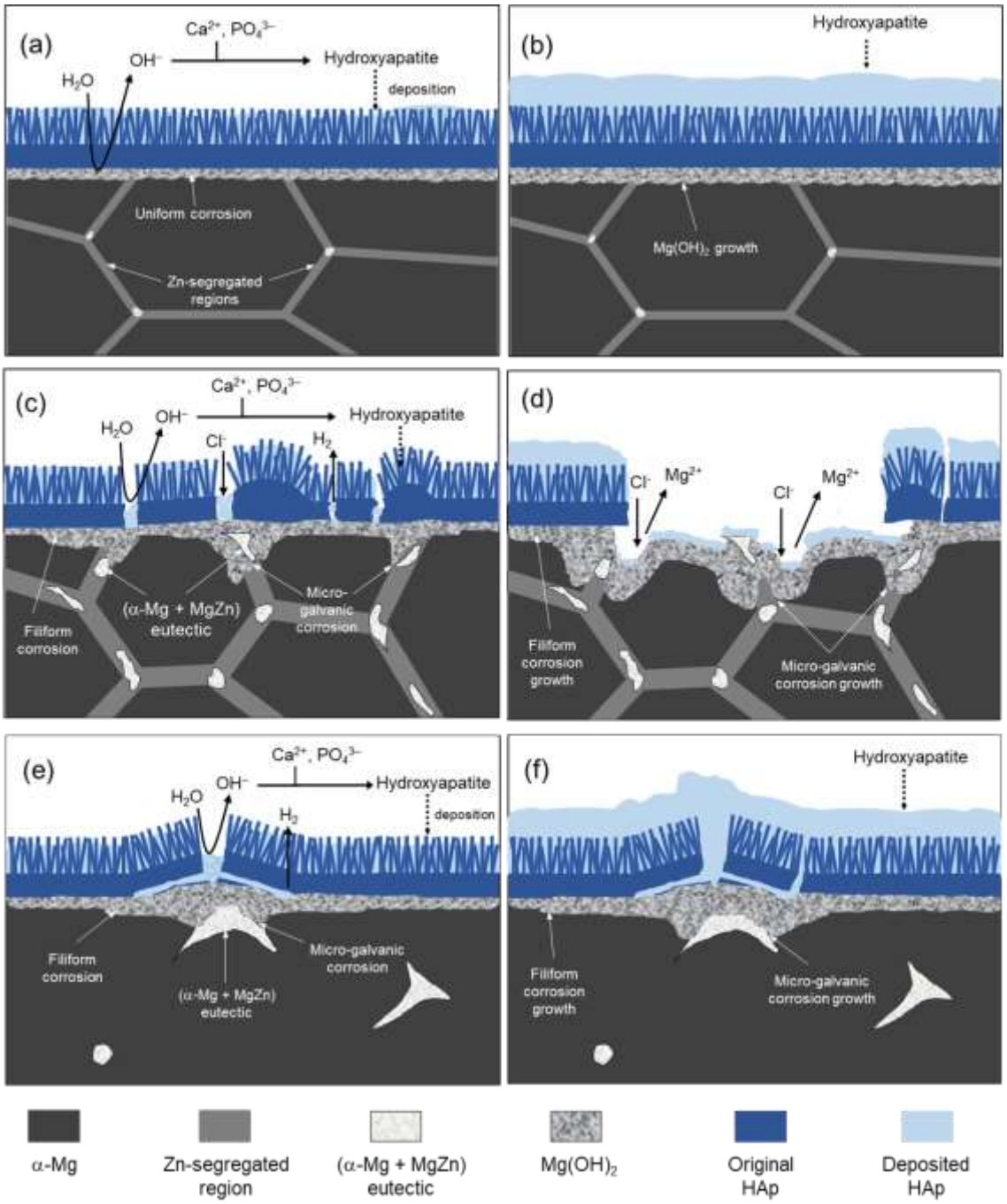

Figure 4.15 Schematic illustrations of corrosion mechanism of (a-b) Ac-1Zn/HAp, (c-d) Ac-7Zn/HAp and (e-f) T4-7Zn/HAp in Hanks' solution. Corrosion morphology (a, c, e) at the initial stage of immersion and (b, d, f) at the steady state

Chapter 5

Enhancement of corrosion resistance and in-vitro biocompatibility of Mg-Zn alloys by carbonate apatite coating

5.1 Introduction

Magnesium and its alloys are considered promising candidates for biodegradable metallic implant materials owing to their biodegradability, excellent biocompatibility and comparable Young's modulus to that of human bones [1–4]. However, the key drawback of Mg and its alloys is a rapid corrosion rate in the physiological environments including human body fluid and blood plasma, which limits their biomedical applications [5,6]. In general, the corrosion resistance of Mg and its alloys can be enhanced by modifying the microstructure by elemental alloying, heat treatment and cold working and/or by forming a surface coating to protect the alloy substrates [1,7–15].

In the previous study, we have developed Mg-Zn binary alloys for biodegradable implant materials. The Mg-Zn binary alloys are interested not only because Zn is a bioabsorbable and biocompatible element, but also because Zn can improve the mechanical strength and reduce the degradation rate of Mg [16]. The results showed that the addition of Zn up to 1 wt.% effectively improved the corrosion resistance of Mg. However, it was noticed that the rapid corrosion of Mg-Zn alloys in the early stage caused a rapid hydrogen (H_2) gas evolution, decreasing the cell attachment and tissue healing by forming a gas cavity [17–19].

In order to sufficiently improve the corrosion resistance and reduce the H_2 gas evolution in the early stage, a surface modification by hydroxyapatite (HAp) coating has been applied to the Mg-Zn alloys [20]. The HAp coating was prepared by a chemical solution deposition method developed by Hiromoto et al. [21–23]. It was revealed that the HAp coating effectively prevented the corrosion of Mg in the initial stage and reduced the corrosion rate of Mg-Zn alloys in the Hanks' solution by 45% after 14 days [20]. However, it was also revealed that the corrosion protectiveness of the HAp coating was significantly influenced by the microstructure

of the substrate alloys: with the higher volume fraction and larger particle size of second phase decreasing the corrosion protectiveness [20]. Although it is widely used to improve the biocompatibility and osteoconductivity of the conventional metallic implant materials, HAp is relatively stable in physiological environment and it is difficult to be resorbed through the osteoclastic process. In the case of the biodegradable implants, HAp could remain several years in the body after the degradation of the substrate materials, thereby potentially causing a secondary infection.

Carbonate apatite (CAp, $Ca_{10-a}(PO_4)_{6-b}(CO_3)_c(OH)_{2-d}$) is the main inorganic constituent found in the human bones rather than the stoichiometric hydroxyapatite (HAp, $Ca_{10}(PO_4)_6(CO_3)(OH)_2$) [24,25]. Because the solubility of CAp is not significantly higher than that of HAp [26] and the CAp blocks promote the differentiation of osteoblast cells and can be resorbed by osteoclast cells, CAp is considered as an excellent candidate for artificial bone materials [27]. Recently, Hiromoto et al. successfully developed CAp coatings on Mg-4Y-3rare earth (WE43) magnesium alloy substrate by modifying the previously developed HAp coating solution [28]. The newly developed CAp coatings showed equivalent corrosion protectiveness to the HAp coating on the WE43 alloy. The substitution of carbonate (CO_3^{2-}) group for phosphate (PO_4^{3-}) and/or hydroxide (OH^-) groups in the apatite structure was reported to reduce the crystallinity of apatite crystals and the crystal size [29,30]. The CAp coatings showed smaller primary particles than the HAp coating on the WE43 alloy [28], which indicated the crystal nuclei of CAp occurred more frequently than that of HAp. The dense and smooth surface structure of the CAp coatings was suggested to improve the cell adhesion of osteoblast cells compared to the porous structure surface of the HAp coating. Moreover, the CAp coatings showed degradation behavior by multinucleated osteoclast cells, which is considered to be osteoclastic resorption [28]. The frequent CAp nuclei were expected to cover the second phases of Mg-Zn alloys more effectively than HAp nuclei. These facts suggested that the CAp coating prepared by the chemical solution deposition method might be more suitable for biodegradable Mg-Zn alloys containing relatively large size second phases compared to the HAp coating.

In this study, the CAp coating was applied to the Mg-Zn alloys with different Zn contents. The composition and structure of the coating formed on the alloys were examined. The corrosion behavior of the CAp-coated Mg-Zn alloys was studied by immersion and electrochemical impedance spectroscopy (EIS) tests in Hanks' solution. The cell viability of the CAp-coated, HAp-coated and uncoated Mg-Zn alloys was investigated with mouse osteoblastic cell line MC3T3-E1 to examine the biocompatibility.

5.2 Experimental procedures

5.2.1 Materials preparation

Mg-Zn binary alloys with different Zn contents (1 wt%, 5 wt% and 7 wt%) were prepared from high purity Mg ingots (> 99.9 wt.%) and Zn shots (> 99.99 wt.%). The raw materials were melted under protection with a 95 vol.% Ar + 5 vol.% CH_2FCF_3 mixed gas atmosphere in an induction furnace. The molten metals were cast into a copper mold at a room temperature to obtain cylindrical-shape ingots with the dimensions of 25 mm in diameter and 70 mm in length. The Mg-7%Zn alloy was subjected to solution heat treatment (T4 treatment) to adjust the microstructure. The T4 treatment was carried out in a high vacuum furnace at 400 ^oC for 12 h, followed by water quenching at a room temperature. The ingots of the as-cast and T4-treated Mg-Zn alloys were then machined into cylinders with a diameter of 15 mm and finally cut into discs with thickness of 2 mm for further analysis and experiments.

5.2.2 Synthesis of CAp and HAp coatings on Mg-Zn alloys

The surfaces of the Mg-Zn discs were ground using SiC paper with grit up to #4000, then ultrasonically rinsed in acetone. The treatment solution for HAp coating was prepared with ethylenediaminetetraacetic acid calcium disodium salt hydrate ($C_{10}H_{12}CaN_2Na_2O_8$, Ca-EDTA), potassium dihydrogen phosphate (KH_2PO_4), and sodium hydroxide (NaOH). The final concentration of Ca-EDTA and KH_2PO_4 of the treatment solution was ca. 0.2 mol/L. The pH of the treatment solution was 7.8. For CAp coating, sodium bicarbonate ($NaHCO_3$) was added to the treatment solution with concentration of 1.1 mol/L. The pH of the solution for CAp coating was ca. 7.4. The as-polished Mg-Zn discs were immersed in the treatment solutions at 90 ^oC for 2 h. The samples and preparation conditions are listed in Table 5.1.

5.2.3 Immersion test

The immersion tests for the CAp-coated samples were conducted in Hanks' solution. The ratio of the Hank's solution volume to the sample surface area was 50 ml/1 cm^2. The chemical composition of the Hanks' solution is shown in Table 5.2. The samples were immersed in Hanks' solution in an incubator at 37 ^oC for 14 days. Three samples from each CAp-coated alloy were used for the immersion test. On Day 1, 3, 5, 7 and 14 of immersion tests, the concentration of Mg^{2+} ions released in Hanks' solution was quantified by a colorimetric

method using Xylidyl blue-I [31,32]. On Day 14, the samples were removed from the testing solution, gently rinsed with distilled water and dried with a N_2 gas flow.

5.2.4 Impedance tests

The electrochemical impedance spectroscopy (EIS) tests were conducted in Hanks' solution at 37 ^oC using impedance analyzer (Solartron, SI 1260). The surface of the samples for impedance tests was covered with a polytetrafluoroethylene (PTFE) tape and the remaining 1 cm^2 area was exposed as a working electrode to 500 ml of Hanks' solution. A saturated Ag/AgCl electrode and a platinum plate were used as the reference and the counter electrodes, respectively. The open circuit potential was measured for 0.5 h and subsequently the EIS was measured at the open circuit potential. The scan frequency ranged from 10^5 Hz to 10^{-2} Hz and the perturbation amplitude was 5 mV. The EIS spectra were then analyzed using the ZView software.

5.2.5 Cell viability tests

The cell culture tests were carried out for the CAp- and HAp-coated and uncoated samples using mouse osteoblastic cell line MC3T3-E1 supplied by RIKEN Cell Bank (Cell No. RBRC-RCB1126). The MC3T3-E1 cells were seeded on the sample surfaces with a density of 20,000 cells/cm^2 and cultured in medium supplemented with 10 vol.% fetal bovine serum (α-MEM + FBS) at 37 ± 0.5 ^oC under a 5% CO_2 atmosphere for 24 and 72 h. After incubation for 24 h and 72 h, the samples were retrieved from the medium, and the cells were fixed with methanol and stained with Giemsa solution for observation of cell proliferation and morphology qualitatively.

The number of living cells was counted using ImageJ software to calculate the average cell density. The cell densities were first compared using a two-way analysis of variance (ANOVA). Since the two-way ANOVA test revealed that there was an interaction between the type of alloy and the type of coating, the differences between all nine types of samples were tested using a one-way ANOVA. Significant differences between samples were then analyzed using Tukey-Kramer test as a post-hoc test.

5.2.6 Materials characterization

Crystal structure of the CAp coatings was characterized using X-rays diffractometry (XRD, Bruker, D2 Phaser) and incorporation of carbonate in apatite structure was investigated using diffuse reflectance Fourier transform infrared spectroscopy (FTIR, Shimadzu, IRTracer-100). The surface and cross-section images of the samples before and after immersion test were characterized using backscattered electron microscope (BSE-SEM, HITACHI, Miniscope TM-3000) and field-emission scanning electron microscope (FE-SEM, JEOL, JSM-7200F) equipped with energy-dispersive X-ray spectrometer (EDS, JEOL, JED-2300).

5.3 Results

5.3.1 CAp coatings on Mg-Zn alloy substrates

Figure 5.1 shows the XRD patterns of the Mg-Zn alloys treated for CAp coating and the pattern of the Ac-1Zn alloy treated for HAp coating. On all the XRD patterns, the diffraction peaks of apatite (Ap) structure were observed along with the peaks of Mg matrix. Among all the peaks of apatite structure, the peaks of $(002)_{Ap}$ showed the highest diffraction intensity, and they are separately shown in Fig. 5.1(b). The peak position of the $(002)_{Ap}$ plane of the samples treated for CAp coating was at a lower angle than that of the sample treated for HAp coating. The peak position shift to the lower angle is attributed to the substitution of the phosphate (PO_4^{3-}) group by a carbonate (CO_3^{2-}) group in the apatite structure [29,30]. These results indicated that CAp was formed on the Mg-Zn alloys. Generally, the $(002)_{Ap}$ peak position shifts to the lower angle with an increase of carbonate substitution ratio. Here, there was no difference in the $(002)_{Ap}$ peak positions between the CAp-coated samples. Moreover, the intensity and full width at half maximum (FWHM) of $(002)_{Ap}$ peaks showed no significant difference between the CAp-coated samples. These results demonstrated that the CAp coatings with similar carbonate substitution ratio and crystallinity were formed on the Mg-Zn alloys with different Zn contents.

Figure 5.2 shows the FTIR spectra of the CAp coatings on the Mg-Zn alloys and the HAp coating on the Mg-1Zn alloy. The FTIR spectra of the CAp and HAp coatings showed the absorption bands of PO_4^{3-} group at 1150 cm^{-1}, 1000 cm^{-1}, 950 cm^{-1}, 600 cm^{-1} and 550 cm^{-1}, and those of CO_3^{2-} groups at 1455 cm^{-1}, 1410 cm^{-1} and 870 cm^{-1} [33]. The absorption bands observed at 3400 cm^{-1} and 1650 cm^{-1} were derived from the absorbed water. The FTIR spectrum of the

HAp coating showed a slight absorption band at 3560 cm^{-1} which is a specific band from OH^- group of HAp [34]. It can be seen that the absorption intensity of CO_3^{2-} bands of the CAp coatings was obviously higher than that of the HAp coating. In addition, the CAp coatings showed the smaller absorption intensity of PO_4^{3-} bands at 600 cm^{-1} and 550 cm^{-1} than the HAp coating. The results demonstrated that the CO_3^{2-} group was incorporated and substituted the PO_4^{3-} group in the apatite structure with the addition of $NaHCO_3$ into the coating solution.

Figure 5.3 shows the microstructure of the Mg-Zn substrate alloys and the surface and cross-section SEM images of the CAp-coated Mg-Zn alloys. The microstructure of the Ac-1, 5, 7Zn alloys consisted of α-Mg matrix, Zn-segregated regions and (α-Mg + MgZn) eutectic cells, as shown in Fig. 5.3(a-c). The Zn-segregated regions associated with (α-Mg + MgZn) eutectic cells and formed a network-like structure [16]. In the T4-7Zn alloy, the microstructure showed large (α-Mg + MgZn) eutectic cells discretely distributed in α-Mg matrix, as shown in Fig 3(d). The large (α-Mg + MgZn) cells were formed by the melting and solidifying of (α-Mg + MgZn) cells during the T4 heat treatment. The Zn-segregated regions were not observed in the T4-7Zn alloy because they were completely dissolved into α-Mg matrix. The volume fraction and the particle size of (α-Mg + MgZn) eutectic cells of the Ac-1Zn, Ac-5Zn, Ac-7Zn and T4-7Zn alloys were ca. 0.07 vol% and 0.52 μm, 2.18 vol% and 1.81 μm, 2.87 vol% and 2.18 μm, 1.73 vol% and 27.76 μm, respectively [16].

The surfaces of all the CAp-coated samples were uniformly covered with the cauliflower-like CAp particles. The cross-sectional images showed that the cauliflower-like particles formed a dense and continuous layer with a thickness of about 1.1-1.3 μm. The CAp coating grew on α-Mg matrix and (α-Mg + MgZn) eutectic cell with similar uniformity and thickness. The reason why the CAp coating was formed on the relatively large sized (α-Mg + MgZn) eutectic regions as well as on the matrix is a subject for further investigation.

5.3.2 Corrosion behavior of CAp-coated Mg-Zn alloys

(1) Static immersion tests

Figure 5.4 shows the accumulated Mg^{2+} ion release of the CAp-coated Mg-Zn alloys for 14 days immersion in Hanks' solution. The CAp-coated samples showed relatively low and almost the same Mg^{2+} ion release for 3 days immersion regardless of the Zn content of the substrate alloys. In the case of the Ac-1Zn/CAp, the Mg^{2+} ion release rate was slowed down after Day 1 and became almost constant for 14 days. The Ac-7Zn/CAp and the Ac-5Zn/CAp

and T4-7Zn/CAp showed an abrupt increase of the Mg^{2+} ion release rate at around Day 5 and Day 7, respectively. Eventually, the Mg^{2+} ion release of the CAp-coated samples on Day 14 depended on the Zn content of the substrate alloys and the Ac-1Zn/CAp showed the lowest Mg^{2+} ion release between all the samples.

Figure 5.5 shows the surface and cross-section SEM images the CAp-coated samples after immersion in Hanks' solution for 14 days. The surfaces of the CAp-coated samples were fully covered with the deposited corrosion products as shown in Fig. 5.5(a-c). The Ac-1Zn/CAp and T4-7Zn/CAp showed corrosion products with dense structure while the Ac-7Zn/CAp showed corrosion products with porous structure. The cross-section images showed 2-3 layers with different contrast formed on the alloy substrates. EDS analysis was performed to analyze the chemical composition of each layer marked by points 1-3 as shown in Fig. 5.5(d-f) and the composition at each point is listed in Table 5.3. The compositions of points 1 and 2 on the Ac-1Zn/CAp and Ac-7Zn/CAp, and the compositions of points 1, 2 and 3 on the T4-7Zn/CAp were mainly Ca, P and O. This indicated that the layers indicated by these points consisted of calcium phosphate. Comparing with the cross-section images of the samples before immersion tests shown in Fig. 5.3(i-l), it was indicated that the points 1 were on the original CAp coating layers and the points 2 and 3 were on the calcium phosphate layer deposited from Hanks' solution during the immersion tests. The different contrast between the calcium phosphate layers was attributed to the difference in the Ca/P ratio [35]. The Ca/P ratio of the original CAp coating layer was slightly higher than 1.67 of the stoichiometric Ca/P ratio of HAp, which was due to the substitution of the PO_4^{3-} group by a CO_3^{2-} group in the apatite structure. The composition of the point 3 on the Ac-7Zn/CAp was mainly Mg and O with the O/Mg ratio of about 1.9, indicating that the point 3 was on $Mg(OH)_2$. The formation of $Mg(OH)_2$ layer on the Ac-7Zn/CAp demonstrated the corrosion of this sample was severe.

(2) Impedance behavior

Figure 5.6 shows the Bode and Nyquist plots of the CAp-coated samples measured at 0.5 h of immersion in Hanks' solution. On all the Bode plots, the phase shift spectra showed two peaks at around 10^4 and 10^0-10^{-1} Hz, indicating the existence of two time constants. All the Nyquist plots showed one capacitive loop at high frequency and one at medium frequency. Based on these facts and the previous work [20,36,37], an equivalent electric circuit was assumed for the CAp-coated samples and shown in Figure 5.7. The EIS spectra of CAp-coated samples measured at 0.5 h of immersion were fitted using the proposed equivalent electric circuit. In the equivalent circuit, R_s represents the solution resistance. R_{ct} and CPE_{dl} represent

the charge transfer resistance and the constant phase element of electric double layer, respectively. Because the system is non-homogeneous, the constant phase element was used instead of the capacitance. R_c and CPE_c represent the resistance and capacity of the CAp coating, respectively. The polarization resistance (R_p) was calculated using equation (5.1) [36,37]:

$$\frac{1}{R_p} = \frac{1}{R_{ct}+R_c} \tag{5.1}$$

The fitting curves are then shown in Fig. 5.6 as solid lines and the fitted values for equivalent circuit components are listed in Table 4. The EIS result also indicated that the R_p values of the CAp-coated samples depended on the Zn content and T4 treatment and that the Ac-1Zn/CAp exhibited the highest corrosion resistance among all the CAp-coated samples.

5.3.3 Cell viability on Mg-Zn alloys with different surface conditions

Figure 5.8 shows the optical surface images of the uncoated and HAp- and CAp-coated Ac-1Zn, Ac-5Zn and T4-7Zn samples with Giemsa-stained MC3T3-E1 cells cultured for 24 h and 72 h.

On all the samples, the living cells were observed in the non-corroded regions while no cell survived in the corroded regions. On the HAp- and CAp-coated Ac-1Zn alloys, no apparent corrosion was observed after 24 h and 72 h of culture (Fig. 5.8(b), (c)), while localized corrosion occurred on the uncoated Ac-1Zn between 24 h and 72 h. On the uncoated Ac-5Zn, some localized corroded areas with white corrosion product were randomly observed after 24 h (Fig. 5.8(d-1)). After 72 h, the surface of the uncoated Ac-5Zn were entirely corroded and no living cells remained (Fig. 5.8(d-2)). With the HAp and CAp coatings, the Ac-5Zn alloy did not show localized corrosion for 72 h (Fig. 5.8(e), (f)). In the case of the T4-7Zn alloy, the surfaces of the T4-7Zn/Uncoated and T4-7Zn/HAp were partially corroded after 24 h and fully corroded after 72 h (Fig. 5.8(g), (h)). The T4-7Zn/CAp did not show obvious corrosion for 72 h (Fig. 5.8(i)).

In order to quantitatively compare the cell densities between samples, the number of living cells was counted in five regions illustrated in Figure 5.9 and the means ± standard deviation of cell densities is shown in Figure 5.10. The higher cell density on the HAp- and CAp-coated samples than that of the uncoated sample was statistically significant after 24 h for

Ac-5Zn and T4-7Zn alloys. The cell density on the HAp- and CAp-coated Ac-1Zn alloys was slightly higher than that on the uncoated alloy. The cell density of the CAp-coated samples was statistically higher than that of the HAp-coated samples after 72 h. All the CAp-coated alloys showed comparable cell densities after 72 h. These results indicated that the CAp and HAp coatings enhanced the cell viability on the Mg-Zn alloys and the CAp coating improved the cell viability more effectively than the HAp coating.

5.4 Discussion

5.4.1 Formation of CAp coatings on Mg-Zn alloys

The uniform B-type CAp coatings were formed on the Mg-Zn alloys with various Zn contents by the addition of $NaHCO_3$ to the previously developed HAp coating solution. The incorporation of CO_3^{2-} and the substitution of the phosphate group with a carbonate group of the apatite structure; i.e., the formation of the B-type CAp coatings was confirmed by the position shift of the $(002)_{Ap}$ diffraction peak to the lower angle (Fig. 5.1) and the clear appearance of CO_3^{2-} absorption bands, especially the band at 1410 cm^{-1}, on the FTIR spectra (Fig. 5.2) [34,38]. The similar $(002)_{Ap}$ peak position intimated that the substitution ratio of carbonate to phosphate groups did not depend on the Zn content of Mg-Zn alloys. The FWHM of $(002)_{Ap}$ peak of the CAp coatings was larger than that of the HAp coating, indicating the low crystalline CAp.

The morphological characteristics of the CAp coatings did not depend on the composition of the substrate Mg alloy as the similar cauliflower morphology was observed on WE43 alloy [22]. It is important to note that the CAp coatings did not show cracks or pores on the (α-Mg + MgZn) eutectic cells with a size of ca. 30 μm though the HAp coatings showed cracks and pores on the large size eutectic cells of Mg-Zn alloys [20]. In addition, the cracks and pores reduced the corrosion protectiveness of the HAp coatings. The results in this study demonstrated that the CAp coatings formed on the Mg-Zn alloys was less affected by the microstructure of the substrate, enhancing the uniformity and corrosion protectiveness of the coating compared to the HAp coating.

5.4.2 Effect of CAp coating on corrosion of Mg-Zn alloys

The CAp coatings effectively retarded the corrosion of the Mg-Zn alloys in the initial stage of immersion in Hanks' solution (Fig. 5.4). The Mg^{2+} ion release of the coated samples was similar for the first 3 days, indicating that the initial corrosion protectiveness of the CAp coatings did not apparently depend on the Zn content and microstructure of the substrate alloys. On the other hand, the order of the R_p value obtained at 0.5 h of immersion was consistent with the order of the amount of Mg^{2+} ion release at 14 days (Table 5.4 and Fig. 5.4). This fact indicated that there were originally the small differences in the corrosion protectiveness of the CAp coatings between Mg-Zn alloys, and these differences increased with time.

It was reported that the deposition of corrosion products from Hanks' solution enhanced the corrosion protectiveness of the HAp coatings [20,35]. The deposition of calcium phosphate was observed also on the CAp-coated surfaces (Fig. 5.5). Here, the Ac-1Zn/CAp showed a low and almost constant Mg^{2+} ion release rate after Day 1, which was attributed to the defect-free coating due to the negligibly small volume fraction (0.07 vol%) of second phase in Mg-1Zn alloy and to the deposited calcium phosphate layer covering the CAp coating in addition to the relatively high corrosion resistance of the Ac-1Zn alloy substrate [16]. On the other hand, the increase in the Mg^{2+} ion release rate after 3-5 days for the Ac-5Zn/CAp, Ac-7Zn/CAp and T4-7Zn/CAp was resulted from the breakdown of the CAp coating. The breakdown of the HAp coating on the Ac-7Zn/HAp and the Ac-5Zn/HAp and T4-7Zn/HAp appeared to occur at around Day 1, Day 3 and Day 11, respectively [20], indicating that the CAp coatings showed higher breakdown resistance than the HAp coatings. The Mg^{2+} ion release of the CAp-coated samples was strongly influenced by the substrate alloys after the CAp coating was breakdown, which was the same phenomenon as for the HAp-coated Mg-Zn alloys [20]. These facts revealed that the long-term corrosion resistance of the CAp-coated samples depended on the Zn content and microstructure of Mg-Zn alloys.

The average Mg^{2+} ion release rates and the R_p value of the CAp-coated samples were compared with those of the uncoated and HAp-coated samples referred from [16,20] as shown in Figure 5.11 and 5.12, respectively. The average Mg^{2+} ion release rates of the CAp-coated samples were estimated from Day 1 or Day 3 to Day 14 because the ion release curves showed almost linear increasing. The R_p of the uncoated and CAp- and HAp-coated samples were obtained at 0.5 h of immersion in Hanks' solution. Then, the R_p and Mg^{2+} ion release rate

roughly reflects the corrosion protectiveness of the coatings before and after the coating breakdown, respectively.

The Mg^{2+} ion release rates of the CAp-coated samples were about one half of those the uncoated samples, and the R_p values of the CAp-coated samples were 10-90 times higher than those of the uncoated samples. These facts demonstrated that the CAp-coating effectively improved the corrosion resistance of Mg-Zn alloys.

The Mg^{2+} ion release rates of the Ac-1Zn/CAp, Ac-5Zn/CAp, Ac-7Zn/CAp and T4-7Zn/CAp was ca. 25%, 40%, 30% and 45% lower than those of the Ac-1Zn/HAp, Ac-5Zn/HAp, Ac-7Zn/HAp and T4-7Zn/HAp, respectively (Fig. 5.11). In addition, the CAp-coated samples showed 10-70 times higher R_p value than the HAp-coated samples, except for the Ac-1Zn/CAp (Fig. 5.12). It was revealed that the CAp coatings showed significantly higher corrosion protectiveness than the HAp coatings for the Mg-Zn alloys. Tomozawa et al. reported that the thickness and uniformity of the inner dense layer controlled the protectiveness of the HAp coating [39]. In this study, the CAp coatings showed the uniform layers without cracks and pores on the (α-Mg + MgZn) eutectic regions as shown in Fig. 5.3. On the contrary, the HAp coating layers exhibited microcracks and pores around α-Mg matrix and (α-Mg + MgZn) eutectic cells [20]. The higher corrosion protectiveness of the CAp coating was thus attributed to its uniform and defects-free structure. In the case of the Ac-1Zn alloy, the Ac-1Zn/CAp and Ac-1Zn/HAp showed defects-free coatings and the CAp coating was slightly thinner than the inner layer of the HAp coating (1.2 μm vs. 1.5 μm, respectively). Thereby, the R_p value of the Ac-1Zn/CAp was slightly smaller that of the Ac-1Zn/HAp.

As mentioned above, the effect of the CAp coating depended on the Zn content and microstructure of the substrate Mg-Zn alloys especially after the breakdown of the coating layers. As reported previously, the corrosion resistance of the uncoated Mg-Zn binary alloys was governed by the volume fraction of Zn-rich phases [16]. When the volume fraction of Zn-rich phases was small like in the Mg-1Zn alloy (0.07 vol%), the ion release rate was reduced by 60% by the CAp coating (Fig. 5.11). In the case of Ac-5Zn, Ac-7Zn and T4-7Zn alloys with relatively large volume fraction of Zn-rich phases (2.18, 2.87 and 1.73 vol%, respectively), the CAp coating reduced the ion release rates by 40-45%.

The R_p values of the CAp- and HAp-coated and uncoated alloys plotted as a function of the volume fraction of Zn-rich phases are shown in Figure 5.13. The R_p values linearly decreased with an increase of volume fraction of Zn-rich phases for the uncoated and CAp-

coated alloys. Both CAp and HAp coatings showed very high R_p values on the Mg-1Zn alloy (0.07 vol%). However, the R_p value of the HAp-coated alloys decreased drastically with 1.73% of Zn-rich phase. The effect of the appearance of Zn-rich second phases on the R_p value for the HAp-coated alloys was more pronounced than for the uncoated alloys. This fact suggested that the defects in HAp coating due to the second phases governed the initial corrosion protectiveness. The linear relationship between R_p values and volume fraction of Zn-rich phases for the CAp-coated alloys suggested that the Zn-rich second phase caused defects in the CAp coatings which should have been much smaller than those in the HAp coatings. It is thus suggested that the CAp coating is a more suitable coating for Mg-Zn alloys containing large volume fraction of Zn-rich phases than the HAp coating.

The results demonstrated that the CAp coatings effectively prevented the corrosion of Mg in the initial stage and reduced the corrosion rate of the Mg-Zn alloys in the subsequent stages of immersion.

5.4.3 Effect of CAp coating on in-vitro biocompatibility of Mg-Zn alloys

It was revealed that the samples with the CAp coating showed the highest cell viability between samples with the same alloy substrate, and the samples with the HAp coating showed much higher cell viability than the uncoated samples, as shown in Fig. 5.10.

After 24 h of culture (Fig. 5.10(a)), there was a significant difference in cell densities between uncoated and coated samples; whereas the Ac-1Zn substrate samples showed a little difference between uncoated and coated samples. The cell density and the corrosion resistance of the Ac-1Zn alloy were higher than those of the other Mg-Zn alloys with larger Zn content. The relatively high corrosion resistance of the Ac-1Zn alloy is thus responsible for the relatively high cell viability on the Ac-1Zn samples regardless of the coatings after 24 h of culture.

The improvement of the cell viability on the HAp- and CAp-coated Ac-5Zn and T4-7Zn samples was also attributed to the improvement of corrosion resistance by the coatings. This is because the cell viability on Mg alloys generally depends on two factors: release rate of H_2 gas evolution and increase of pH near sample's surface. Many studies reported that a high rate of H_2 gas release in the initial rapid corrosion of Mg prevent the adhesion of living cells to the sample's surface and the rapid increase of pH near the sample reduced the cell proliferation [17–19,40,41]. In the case of the HAp- and CAp-coated samples, the coatings retarded the initial corrosion of the Ac-5Zn and T4-7Zn alloys for longer than 24 h (Fig. 5.4). Consequently, the

release rate of H_2 gas and the increase of pH near the surface were greatly reduced, which implied the enhancement of cell viability.

It is worth mentioning that Ac-5Zn showed no significant difference between HAp- and CAp-coated samples, whereas T4-7Zn showed a significant difference between HAp- and CAp-coated samples. The difference in the effect on cell viability between HAp and CAp coatings was attributed to the presence or absence of defects in the coating. The HAp coating on the T4-7Zn had large cracking defects and its initial corrosion rate was higher that of the other samples [20]. The CAp coating on the T4-7Zn had much less defects than the HAp coating (Fig. 5.3(h), (l)).

After 72 h of culture, the effect of the coatings on the improvement of the cell viability on the Mg-Zn alloys became further significant. No living cells remained on the Ac-5Zn/Uncoated, T4-7Zn/Uncoated and T4-7Zn/HAp due to the severe corrosion after 72 h as shown in Fig. 5.8(d-2), (g-2), (h-2)). The cell density of the Ac-1Zn/Uncoated was significantly lower than that of the HAp- and CAp-coated samples. The result demonstrated that the coatings greatly enhanced the cell viability of Ac-1Zn alloy after 72 h of culture although the coatings did not show a clear effect after 24 h of culture.

The cell densities of the CAp-coated samples were significantly higher than those of the HAp-coated samples after 72 h. The main reason for the higher cell density on the CAp-coated surfaces was the significantly higher corrosion resistance than the HAp-coated surfaces shown in Fig. 5.11 and 5.12. Another reason was the difference in surface morphology of the coatings. Hiromoto et al. reported that the micromorphology of the coatings affected the adhesion and proliferation of the living cells [42]. In the case of the HAp coating, the rod-like crystal structure in the outer layer limited the areas where the focal contacts were formed, which led to the decrease of cell proliferation. The surface of the CAp coating was relatively flat, as can be seen in Fig. 5.3, which did not limit the area for the formation of focal contacts. Thus, it was considered that the adhesion of MC3T3-E1 cells was easier on the CAp coatings, resulting in the higher cell viability on the CAp-coated samples.

5.5 Conclusions

The CAp coatings were formed on the as-cast and T4-treated Mg-1, 5, 7Zn binary alloys by the chemical solution deposition method. The effect of CAp coating on the corrosion behavior and biocompatibility was examined by the immersion and impedance tests in Hanks' solution and the cell culture test of osteoblastic cells, respectively. The following were found:

(1) The structure of the CAp coatings was dense and uniform and did not apparently depend on the microstructure of the substrate, i.e., volume fraction and size of Zn-rich second phase. The CAp coating uniformly covered the second phase with a size of ca. 30 μm.

(2) The CAp coating retarded the Mg^{2+} ion release rate of the alloys to a similar extent in the initial 3-5 days of immersion, and reduced the polarization resistance (R_p) of each alloy by 10-90 times at 0.5 h immersion in Hanks' solution.

(3) After the CAp coatings were partly broken, the influence of the corrosion resistance of the substrate alloy became apparent and the corrosion resistance decreased with an increase of the volume fraction of Zn-rich phase. Nevertheless, the average Mg^{2+} ion release rate of the Mg-Zn alloys was reduced by 40-60% with the CAp coating compared to the uncoated alloys.

(4) The CAp coating increased the R_p at 0.5 h by 1-70 times and decreased the average Mg^{2+} ion release rate by 25-45% over the HAp coating for Ac-5Zn, Ac-7Zn and T4-7Zn alloys.

(5) The CAp coating effectively improved the viability of MC3T3-E1 cells on the Mg-Zn alloys in comparison with the uncoated and HAp-coated alloys. The cell densities on the CAp-coated alloys cultured for 72 h were comparable regardless of the Zn content and microstructure of the alloys.

Consequently, the uniform and defect-free CAp coatings are able to reduce the corrosion rate and improve the biocompatibility of Mg-Zn alloys more effectively than the HAp coatings with defects due to the second phase of the substrate alloy. These facts suggested that the CAp coating can be a superior candidate for biodegradable Mg alloys as a bioabsorbable coating.

5.6 References

[1] M.P. Staiger, A.M. Pietak, J. Huadmai, G. Dias, Magnesium and its alloys as orthopedic biomaterials: A review, Biomaterials. 27 (2006) 1728–1734. https://doi.org/10.1016/j.biomaterials.2005.10.003.

[2] R. Zeng, W. Dietzel, F. Witte, N. Hort, C. Blawert, Progress and challenge for magnesium alloys as biomaterials, Adv. Eng. Mater. 10 (2008) 3–14. https://doi.org/10.1002/adem.200800035.

[3] F. Witte, The history of biodegradable magnesium implants: A review, Acta Biomater. 6 (2010) 1680–1692. https://doi.org/10.1016/j.actbio.2010.02.028.

[4] D. Zhao, F. Witte, F. Lu, J. Wang, J. Li, L. Qin, Current status on clinical applications of magnesium-based orthopaedic implants: A review from clinical translational perspective, Biomaterials. 112 (2017) 287–302. https://doi.org/10.1016/j.biomaterials.2016.10.017.

[5] G. Song, A. Atrens, Understanding magnesium corrosion. A framework for improved alloy performance, Adv. Eng. Mater. 5 (2003) 837–858. https://doi.org/10.1002/adem.200310405.

[6] G. Song, Control of biodegradation of biocompatable magnesium alloys, Corros. Sci. 49 (2007) 1696–1701. https://doi.org/10.1016/j.corsci.2007.01.001.

[7] S. Agarwal, J. Curtin, B. Duffy, S. Jaiswal, Biodegradable magnesium alloys for orthopaedic applications: A review on corrosion, biocompatibility and surface modifications, Mater. Sci. Eng. C. 68 (2016) 948–963. https://doi.org/10.1016/j.msec.2016.06.020.

[8] M. Esmaily, J.E. Svensson, S. Fajardo, N. Birbilis, G.S. Frankel, S. Virtanen, R. Arrabal, S. Thomas, L.G. Johansson, Fundamentals and advances in magnesium alloy corrosion, Prog. Mater. Sci. 89 (2017) 92–193. https://doi.org/10.1016/j.pmatsci.2017.04.011.

[9] X. Li, X. Liu, S. Wu, K.W.K. Yeung, Y. Zheng, P.K. Chu, Design of magnesium alloys with controllable degradation for biomedical implants: From bulk to surface, Acta Biomater. 45 (2016) 2–30. https://doi.org/10.1016/j.actbio.2016.09.005.

[10] L.C. Trincə, M. Fântânariu, C. Solcan, A.E. Trofin, L. Burtan, D.M. Acatrinei, S. Stanciu, B. Istrate, C. Munteanu, In vivo degradation behavior and biological activity

of some new Mg-Ca alloys with concentration's gradient of Si for bone grafts, Appl. Surf. Sci. 352 (2015) 140–150. https://doi.org/10.1016/j.apsusc.2015.03.136.

[11] N.Q. Cao, D.N. Pham, N. Kai, H. V. Dinh, S. Hiromoto, E. Kobayashi, In vitro corrosion properties of mg matrix in situ composites fabricated by spark plasma sintering, Metals (Basel). 7 (2017). https://doi.org/10.3390/met7090358.

[12] I. Nakahata, Y. Tsutsumi, E. Kobayashi, Mechanical properties and corrosion resistance of magnesium–hydroxyapatite composites fabricated by spark plasma sintering, Metals (Basel). 10 (2020) 1–13. https://doi.org/10.3390/met10101314.

[13] P. Makkar, H.J. Kang, A.R. Padalhin, O. Faruq, B.T. Lee, In-vitro and in-vivo evaluation of strontium doped calcium phosphate coatings on biodegradable magnesium alloy for bone applications, Appl. Surf. Sci. 510 (2020) 145333. https://doi.org/10.1016/j.apsusc.2020.145333.

[14] J. Kuang, Z. Ba, Z. Li, Z. Wang, J. Qiu, The study on corrosion resistance of superhydrophobic coatings on magnesium, Appl. Surf. Sci. 501 (2020) 144137. https://doi.org/10.1016/j.apsusc.2019.144137.

[15] J. Cao, R. Lian, X. Jiang, Magnesium and fluoride doped hydroxyapatite coatings grown by pulsed laser deposition for promoting titanium implant cytocompatibility, Appl. Surf. Sci. 515 (2020) 146069. https://doi.org/10.1016/j.apsusc.2020.146069.

[16] D. Pham, S. Hiromoto, E. Kobayashi, Influences of Zinc Content and Solution Heat Treatment on Microstructure and Corrosion Behavior of Mg-Zn Binary Alloys, Corrosion. 77 (2021) 323–338. https://doi.org/10.5006/3672.

[17] J. Kuhlmann, I. Bartsch, E. Willbold, S. Schuchardt, O. Holz, N. Hort, D. Höche, W.R. Heineman, F. Witte, Fast escape of hydrogen from gas cavities around corroding magnesium implants, Acta Biomater. 9 (2013) 8714–8721. https://doi.org/10.1016/j.actbio.2012.10.008.

[18] D. Noviana, D. Paramitha, M.F. Ulum, H. Hermawan, The effect of hydrogen gas evolution of magnesium implant on the postimplantation mortality of rats, J. Orthop. Transl. 5 (2016) 9–15. https://doi.org/10.1016/j.jot.2015.08.003.

[19] C. Plaass, S. Ettinger, L. Sonnow, S. Koenneker, Y. Noll, A. Weizbauer, J. Reifenrath, L. Claassen, K. Daniilidis, C. Stukenborg-Colsman, H. Windhagen, Early results using

a biodegradable magnesium screw for modified chevron osteotomies, J. Orthop. Res. 34 (2016) 2207–2214. https://doi.org/10.1002/jor.23241.

[20] D.N. Pham, S. Hiromoto, O. Minho, E. Kobayashi, Influence of substrate microstructure on hydroxyapatite coating and corrosion behavior of coated Mg-Zn alloys, Surf. Coat. Technol. 111 (2021).

[21] S. Hiromoto, M. Tomozawa, Hydroxyapatite coating of AZ31 magnesium alloy by a solution treatment and its corrosion behavior in NaCl solution, Surf. Coat. Technol. 205 (2011) 4711–4719. https://doi.org/10.1016/j.surfcoat.2011.04.036.

[22] M. Tomozawa, S. Hiromoto, Y. Harada, Microstructure of hydroxyapatite-coated magnesium prepared in aqueous solution, Surf. Coatings Technol. 204 (2010) 3243–3247. https://doi.org/10.1016/j.surfcoat.2010.03.023.

[23] M. Tomozawa, S. Hiromoto, Growth mechanism of hydroxyapatite-coatings formed on pure magnesium and corrosion behavior of the coated magnesium, Appl. Surf. Sci. 257 (2011) 8253–8257. https://doi.org/10.1016/j.apsusc.2011.04.087.

[24] Y. Doi, T. Shibutani, Y. Moriwaki, T. Kajimoto, Y. Iwayama, Sintered carbonate apatites as bioresorbable bone substitutes, J. Biomed. Mater. Res. 39 (1998) 603–610. https://doi.org/10.1002/(SICI)1097-4636(19980315)39:4<603::AID-JBM15>3.0.CO;2-7.

[25] K. Ishikawa, Bone substitute fabrication based on dissolution-precipitation reactions, Materials (Basel). 3 (2010) 1138–1155. https://doi.org/10.3390/ma3021138.

[26] K. Ishikawa, Carbonate apatite bone replacement: Learn from the bone, J. Ceram. Soc. Japan. 127 (2019) 595–601. https://doi.org/10.2109/jcersj2.19042.

[27] H. Nagai, M. Kobayashi-Fujioka, K. Fujisawa, G. Ohe, N. Takamaru, K. Hara, D. Uchida, T. Tamatani, K. Ishikawa, Y. Miyamoto, Effects of low crystalline carbonate apatite on proliferation and osteoblastic differentiation of human bone marrow cells, J. Mater. Sci. Mater. Med. 26 (2015). https://doi.org/10.1007/s10856-015-5431-5.

[28] S. Hiromoto, S. Itoh, N. Noda, T. Yamazaki, T. Akashi, Osteoclast and osteoblast responsive carbonate apatite coatings for biodegradable magnesium alloys, Sci. Technol. Adv. Mater. 21 (2020) 346–358. https://doi.org/10.1080/14686996.2020.1761237.

[29] R. Zapanta-LeGeros, Effect of carbonate on the lattice parameters of apatite, Nature.

006 (1965) 403–404.

[30] I. Cacciotti, Multisubstituted hydroxyapatite powders and coatings: The influence of the codoping on the hydroxyapatite performances, Int. J. Appl. Ceram. Technol. 16 (2019) 1864–1884. https://doi.org/10.1111/ijac.13229.

[31] C.K. Mann, J.H. Yoe, Spectrophotometric determination of magnesium with sodium 1-azo-2-hydroxy-3-(2,4-dimethylcarboxanilido)-naphthalene-1′-(2-hydroxybenzene-5-sulfonate), Anal. Chem. 28 (1956) 202–205. https://doi.org/10.1021/ac60110a016.

[32] H. Watanabe, H. Tanaka, Dual-wavelength spectrophotometric determination of magnesium (ii) with xylidyl blue I and nonionic surfactant, Bunseki Kagaku. 26 (1977) 635–639. https://doi.org/10.2116/bunsekikagaku.26.9_635.

[33] Y. Suetsugu, Carbonate group in apatite structure, J. Soc. Inorg. Mater. Japan. 3 (1996) 48–54. https://doi.org/10.11451/mukimate1994.3.48.

[34] C. Rey, O. Marsan, C. Sarda, C. Christophe, D. David, G. Stéphanie, Characterization of Calcium Phosphates Using Vibrational Spectroscopies, in: Advances in Calcium Phosphate Biomaterials, 2014. http://link.springer.com/10.1007/978-3-642-53980-0.

[35] S. Hiromoto, M. Tomozawa, Corrosion behavior of magnesium with hydroxyapatite coatings formed by hydrothermal treatment, Mater. Trans. 51 (2010) 2080–2087. https://doi.org/10.2320/matertrans.M2010192.

[36] A.D. King, N. Birbilis, J.R. Scully, Accurate Electrochemical Measurement of Magnesium Corrosion Rates; a Combined Impedance, Mass-Loss and Hydrogen Collection Study, Electrochim. Acta. 121 (2014) 394–406. https://doi.org/10.1016/j.electacta.2013.12.124.

[37] Q. Li, W. Ye, H. Gao, L. Gao, Improving the corrosion resistance of ZEK100 magnesium alloy by combining high-pressure torsion technology with hydroxyapatite coating, Mater. Des. 181 (2019) 107933. https://doi.org/10.1016/j.matdes.2019.107933.

[38] Y. Suetsugu, I. Shimoya, J. Tanaka, Configuration of carbonate ions in apatite structure determined by polarized infrared spectroscopy, J. Am. Ceram. Soc. 81 (1998) 746–748. https://doi.org/10.1111/j.1151-2916.1998.tb02403.x.

[39] M. Tomozawa, S. Hiromoto, Microstructure of hydroxyapatite- and octacalcium phosphate-coatings formed on magnesium by a hydrothermal treatment at various pH

values, Acta Mater. 59 (2011) 355–363. https://doi.org/10.1016/j.actamat.2010.09.041.

[40] H.K. Kim, H.S. Han, K.S. Lee, D.H. Lee, J.W. Lee, H. Jeon, S.Y. Cho, H.J. Roh, Y.C. Kim, H.K. Seok, Comprehensive study on the roles of released ions from biodegradable Mg–5 wt% Ca–1 wt% Zn alloy in bone regeneration, J. Tissue Eng. Regen. Med. 11 (2017) 2710–2724. https://doi.org/10.1002/term.2166.

[41] Z.G. Huan, M.A. Leeflang, J. Zhou, L.E. Fratila-Apachitei, J. Duszczyk, In vitro degradation behavior and cytocompatibility of Mg-Zn-Zr alloys, J. Mater. Sci. Mater. Med. 21 (2010) 2623–2635. https://doi.org/10.1007/s10856-010-4111-8.

[42] S. Hiromoto, T. Yamazaki, Micromorphological effect of calcium phosphate coating on compatibility of magnesium alloy with osteoblast, Sci. Technol. Adv. Mater. 18 (2017) 96–109. https://doi.org/10.1080/14686996.2016.1266238.

Table 5.1 Samples and preparation conditions

Sample	Substrate alloy	Surface condition	pH of coating solution as prepared
Ac-1Zn/Uncoated	As-cast Mg-1%Zn	As-polished	-
Ac-5Zn/Uncoated	As-cast Mg-5%Zn	As-polished	-
Ac-7Zn/Uncoated	As-cast Mg-7%Zn	As-polished	-
T4-7Zn/Uncoated	T4-treated Mg-7%Zn	As-polished	-
Ac-1Zn/HAp	As-cast Mg-1%Zn	HAp coated	7.8
Ac-5Zn/HAp	As-cast Mg-5%Zn	HAp coated	7.8
Ac-7Zn/HAp	As-cast Mg-7%Zn	HAp coated	7.8
T4-7Zn/HAp	T4-treated Mg-7%Zn	HAp coated	7.8
Ac-1Zn/CAp	As-cast Mg-1%Zn	CAp-coated	7.4
Ac-5Zn/CAp	As-cast Mg-5%Zn	CAp-coated	7.4
Ac-7Zn/CAp	As-cast Mg-7%Zn	CAp-coated	7.4
T4-7Zn/CAp	T4-treated Mg-7%Zn	CAp-coated	7.4

Table 5.2 Components of Hanks' solution

Reagent	NaCl	KCl	$Na_2HPO_4.H_2O$	KH_2PO_4	$MgSO_4.7H_2O$	$NaHCO_3$	$CaCl_2$
Concentration, g / L	8.00	0.40	0.06	0.06	0.20	0.35	0.14

Table 5.3 Composition at the points marked on the cross-section images of Mg-1Zn and Mg-7Zn alloys after immersion in Hanks' solution for 14 days

Sample	Point number	Concentration, C / at. %						Ca/P ratio
		C	O	Mg	P	Ca	Zn	
Ac-1Zn /CAp	#1	3.6	44.3	7.6	16.1	28.3	0.2	1.76
	#2	13.7	49.7	2.1	15.3	19.3	0.04	1.26
Ac-7Zn /CAp	#1	3.1	28.0	3.8	24.3	40.3	0.6	1.66
	#2	2.4	38.7	3.2	23.8	31.8	0.1	1.34
	#3	42.0	37.2	19.5	0.7	0.4	0.2	0.62
T4-7Zn /CAp	#1	2.6	47.8	4.2	16.4	28.7	0.2	1.75
	#2	4.1	48.5	3.6	19.3	24.3	0.3	1.26
	#3	6.8	56.3	3.4	15.3	17.9	0.2	1.17

Table 5.4 Fitting results of the EIS spectra of CAp-coated Mg-Zn alloys

	R_s ($\Omega \cdot cm^2$)	CPE_{dl} ($\mu F \cdot cm^{-2}$)	n	R_{ct} ($\Omega \cdot cm^2$)	CPE_c ($\mu F \cdot cm^{-2}$)	n	R_c ($\Omega \cdot cm^2$)	R_P ($\Omega \cdot cm^2$)
Ac-1Zn/CAp	26.84	0.89	0.70	19357	6.88	0.77	2.12E5	2.31E5
Ac-5Zn/CAp	17.88	2.86	0.62	13059	3.91	0.87	1.62E5	1.75E5
Ac-7Zn/CAp	14.14	0.79	0.71	12598	7.83	0.66	8.38E4	9.64E4
T4-7Zn/CAp	34.14	1.22	0.68	17780	5.90	0.811	1.70E5	1.88E5

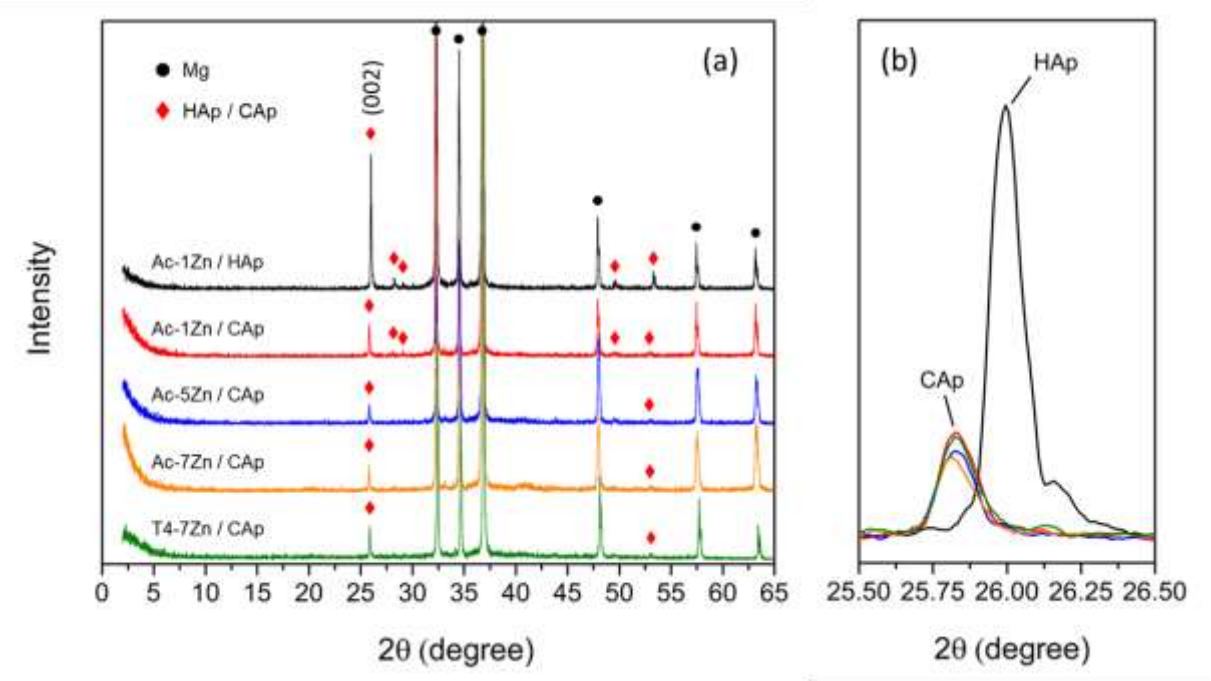

Figure 5.1 XRD patterns of the CAp- and HAp-coated Mg-Zn alloys: (a) wide range and (b) narrow range for the $(002)_{Ap}$ plane

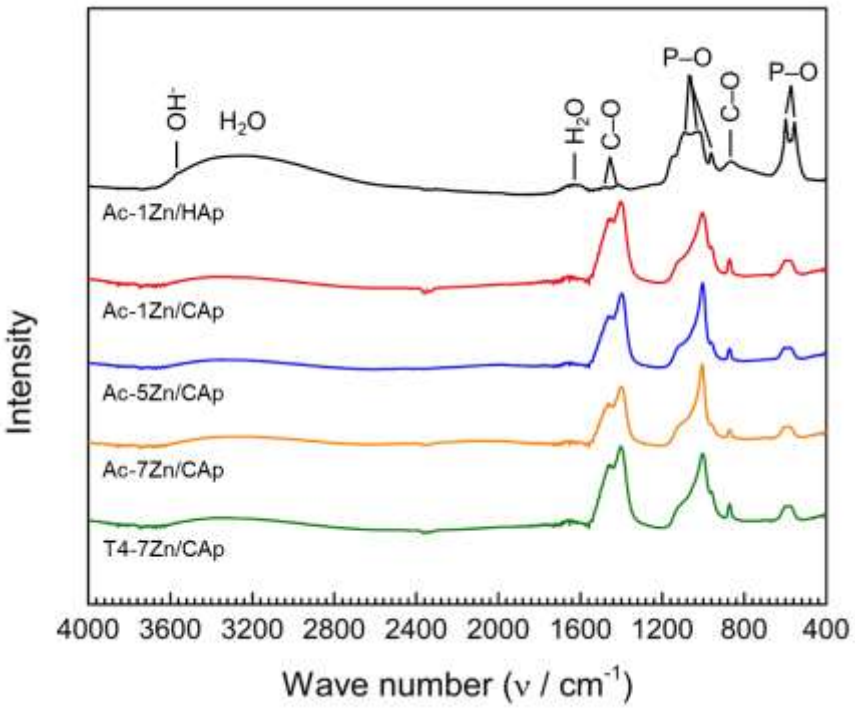

Figure 5.2 FT-IR spectra of the CAp- and HAp-coated Mg-Zn alloys

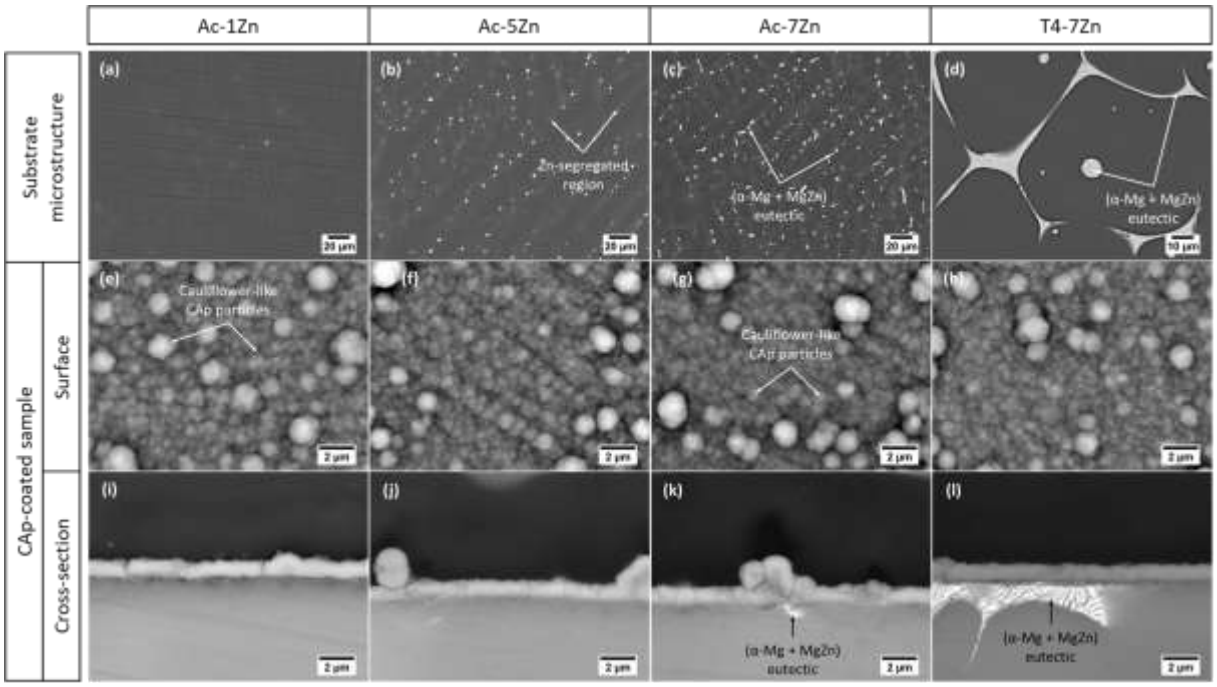

Figure 5.3 (a)-(h) Surface SEM images of (a)-(d) uncoated and (e)-(h) CAp-coated Ac-1Zn, Ac-5Zn, Ac-7Zn and T4-7Zn alloys, respectively. (i)-(l) Cross-sectional SEM images of CAp-coated Ac-1Zn, Ac-5Zn, Ac-7Zn and T4-7Zn alloys, respectively

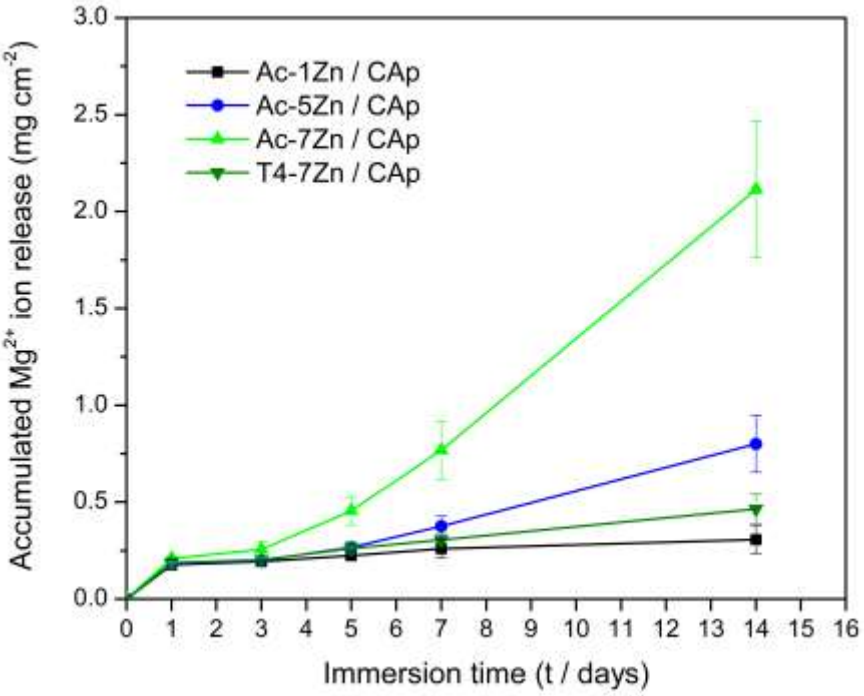

Figure 5.4 Accumulated Mg^{2+} ions release of CAp-coated Mg-Zn alloys as a function of immersion time in Hanks' solution

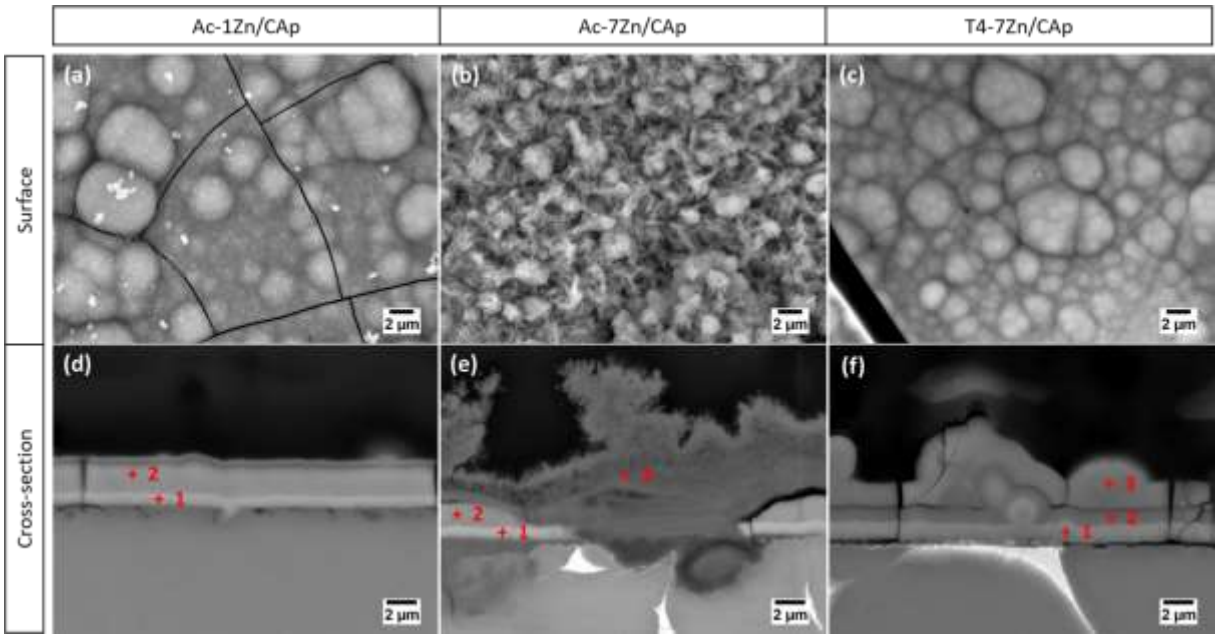

Figure 5.5 (a)-(c) Surface and (d)-(f) cross-sectional SEM images of Mg-1Zn and Mg-7Zn alloys after 14-day immersion test. (a) and (d) Ac-1Zn/CAp, (b) and (e) Ac-7Zn/CAp and (c) and (f) T4-7Zn/CAp

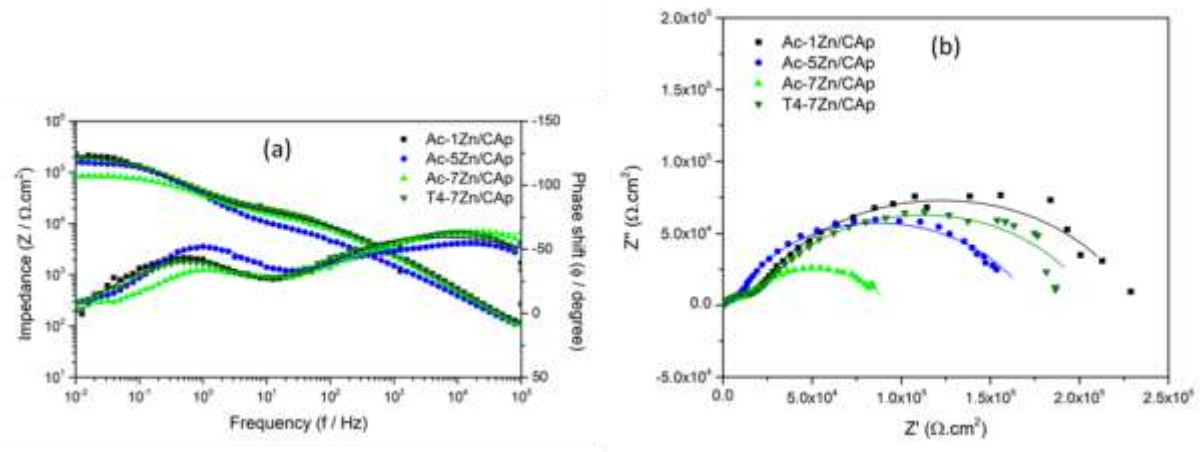

Figure 5.6 EIS plots of CAp-coated Mg-Zn alloys. (a) Bode plots and (b) Nyquist plots. Scatter symbols are experimental data and solid lines are fitting data

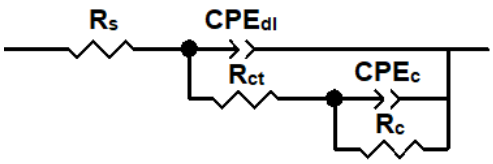

Figure 5.7 Equivalent electric circuits for fitting EIS spectra of CAp-coated Mg-Zn alloys

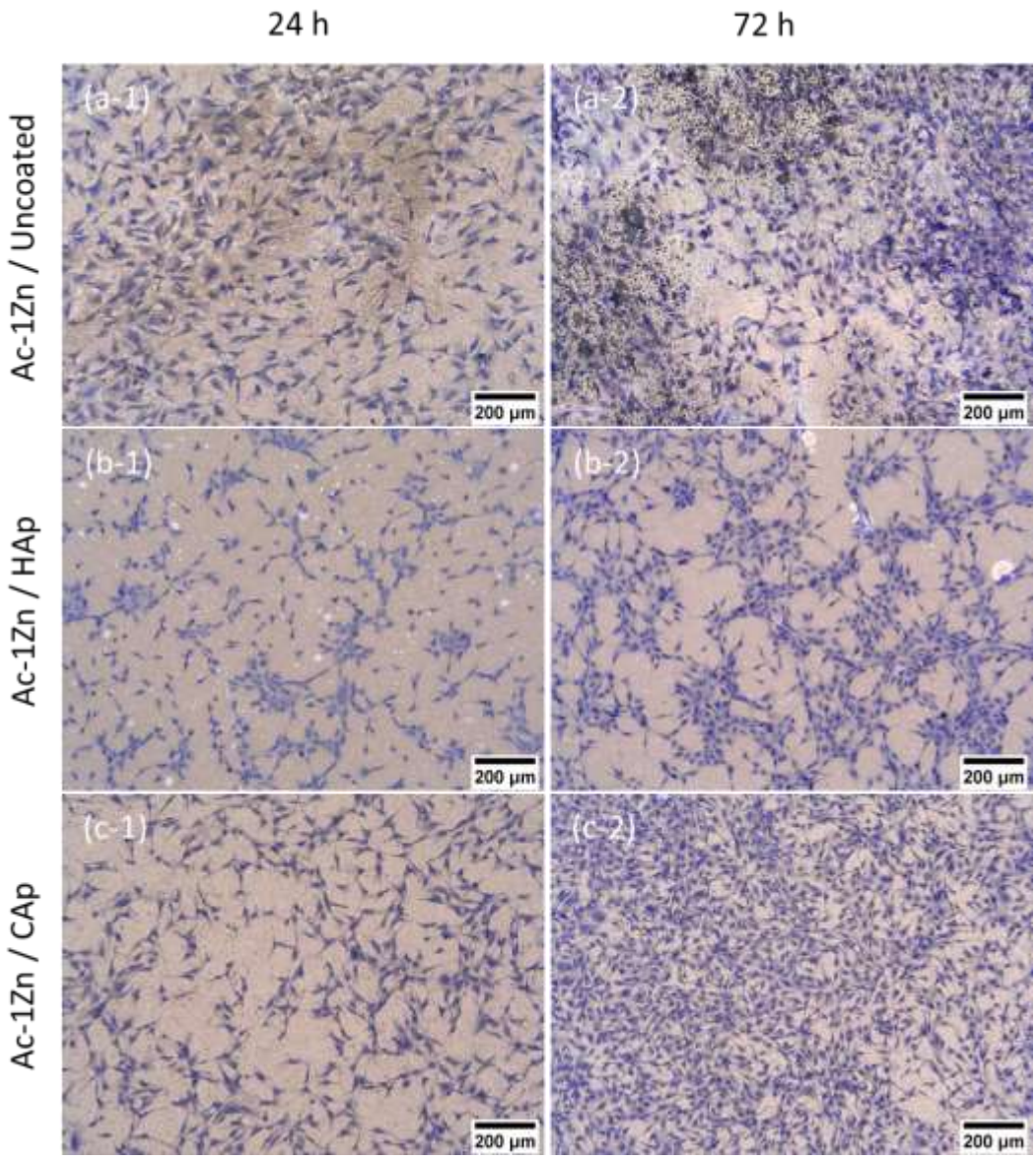

Figure 5.8 Surface images of (a-1) and (a-2) Ac-1Zn/Uncoated, (b-1) and (b-2) Ac-1Zn/HAp, (c-1) and (c-2) Ac-1Zn/CAp, (d-1) and (d-2) Ac-5Zn/Uncoated, (e-1) and (e-2) Ac-5Zn/HAp, (f-1) and (f-2) Ac-5Zn/CAp, (g-1) and (g-2) T4-7Zn/Uncoated, (h-1) and (h-2) T4-7Zn/HAp and (i-1) and (i-2) T4-7Zn/CAp with Giemsa-stained MC3T3-E1 cells cultured for 24 h and 72 h

(Figure 5.8 continue in next page)

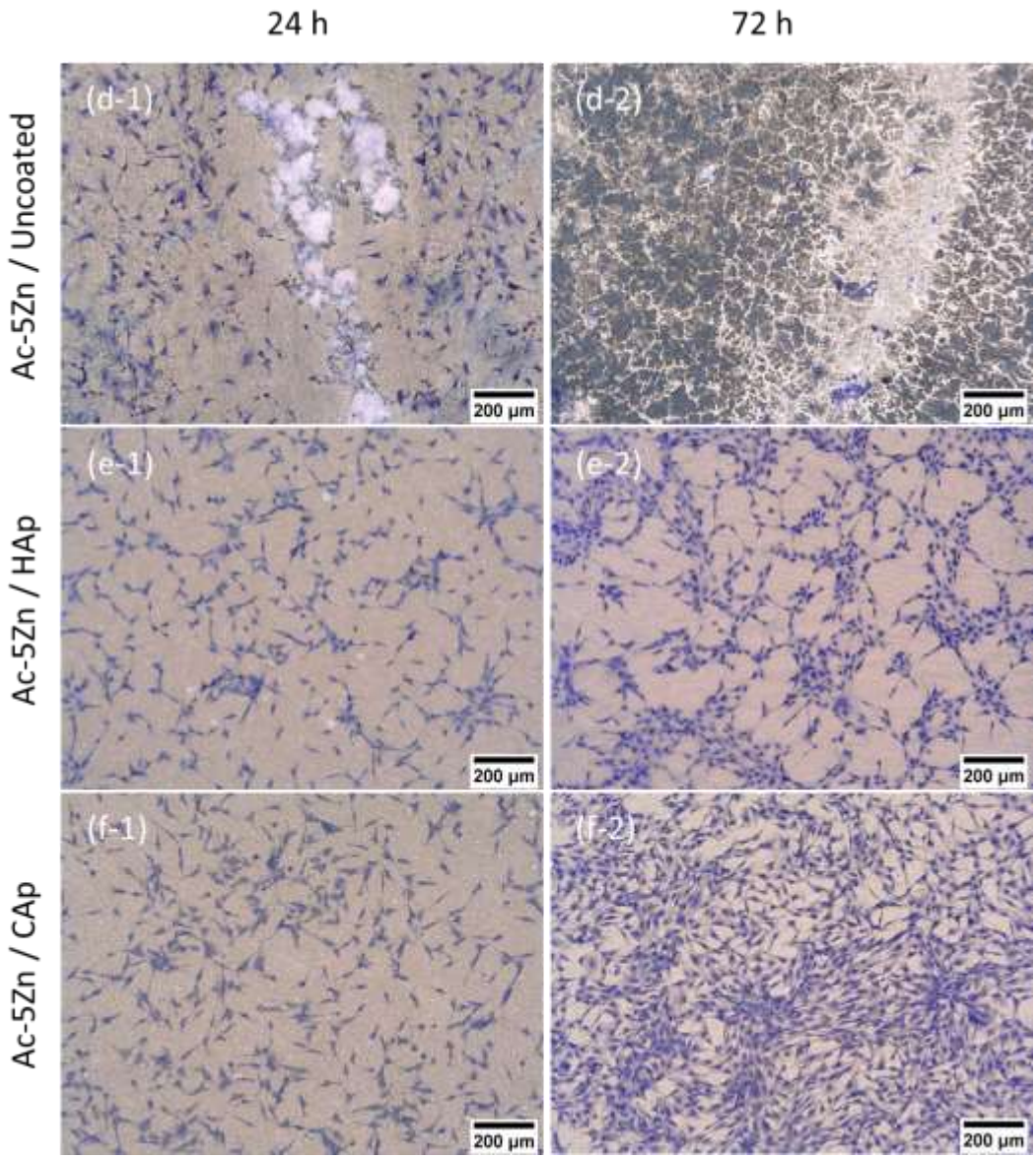

Figure 5.8 Surface images of (a-1) and (a-2) Ac-1Zn/Uncoated, (b-1) and (b-2) Ac-1Zn/HAp, (c-1) and (c-2) Ac-1Zn/CAp, (d-1) and (d-2) Ac-5Zn/Uncoated, (e-1) and (e-2) Ac-5Zn/HAp, (f-1) and (f-2) Ac-5Zn/CAp, (g-1) and (g-2) T4-7Zn/Uncoated, (h-1) and (h-2) T4-7Zn/HAp and (i-1) and (i-2) T4-7Zn/CAp with Giemsa-stained MC3T3-E1 cells cultured for 24 h and 72 h

(Figure 5.8 continue in next page)

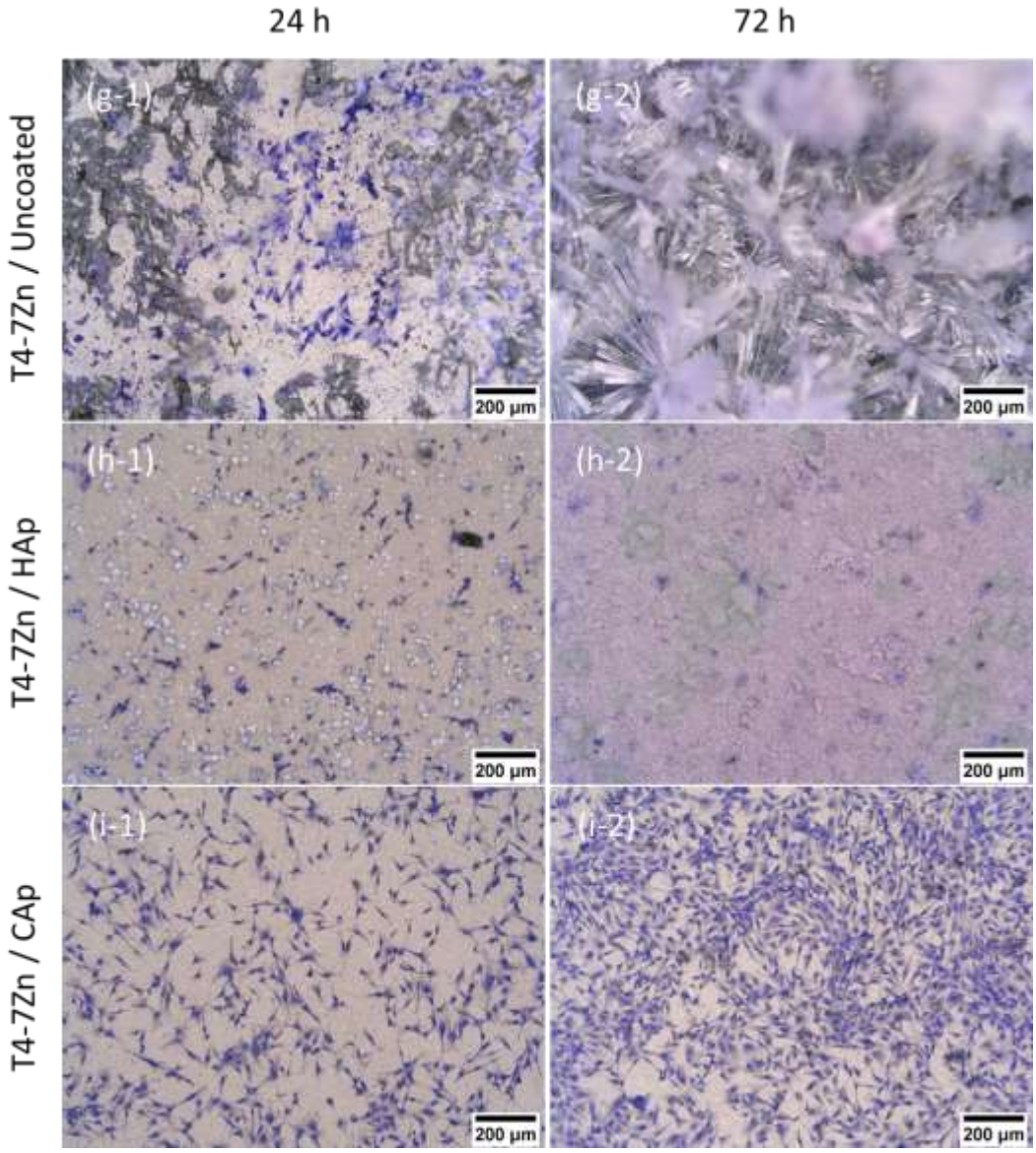

Figure 5.8 Surface images of (a-1) and (a-2) Ac-1Zn/Uncoated, (b-1) and (b-2) Ac-1Zn/HAp, (c-1) and (c-2) Ac-1Zn/CAp, (d-1) and (d-2) Ac-5Zn/Uncoated, (e-1) and (e-2) Ac-5Zn/HAp, (f-1) and (f-2) Ac-5Zn/CAp, (g-1) and (g-2) T4-7Zn/Uncoated, (h-1) and (h-2) T4-7Zn/HAp and (i-1) and (i-2) T4-7Zn/CAp with Giemsa-stained MC3T3-E1 cells cultured for 24 h and 72 h

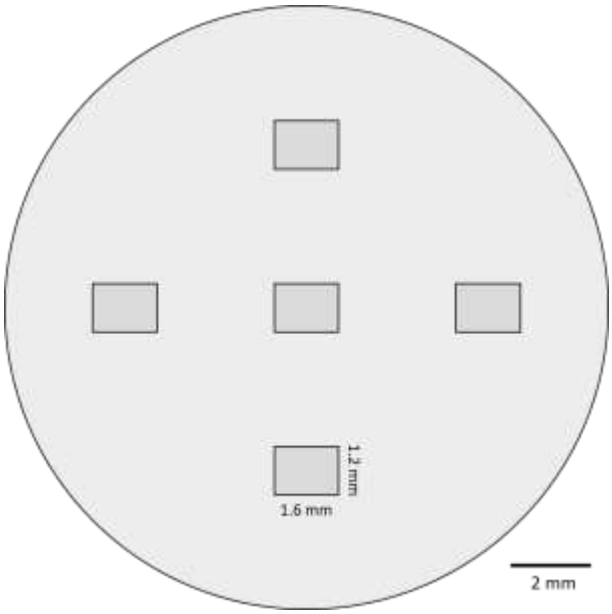

Figure 5.9 Illustration of regions used for counting living cells

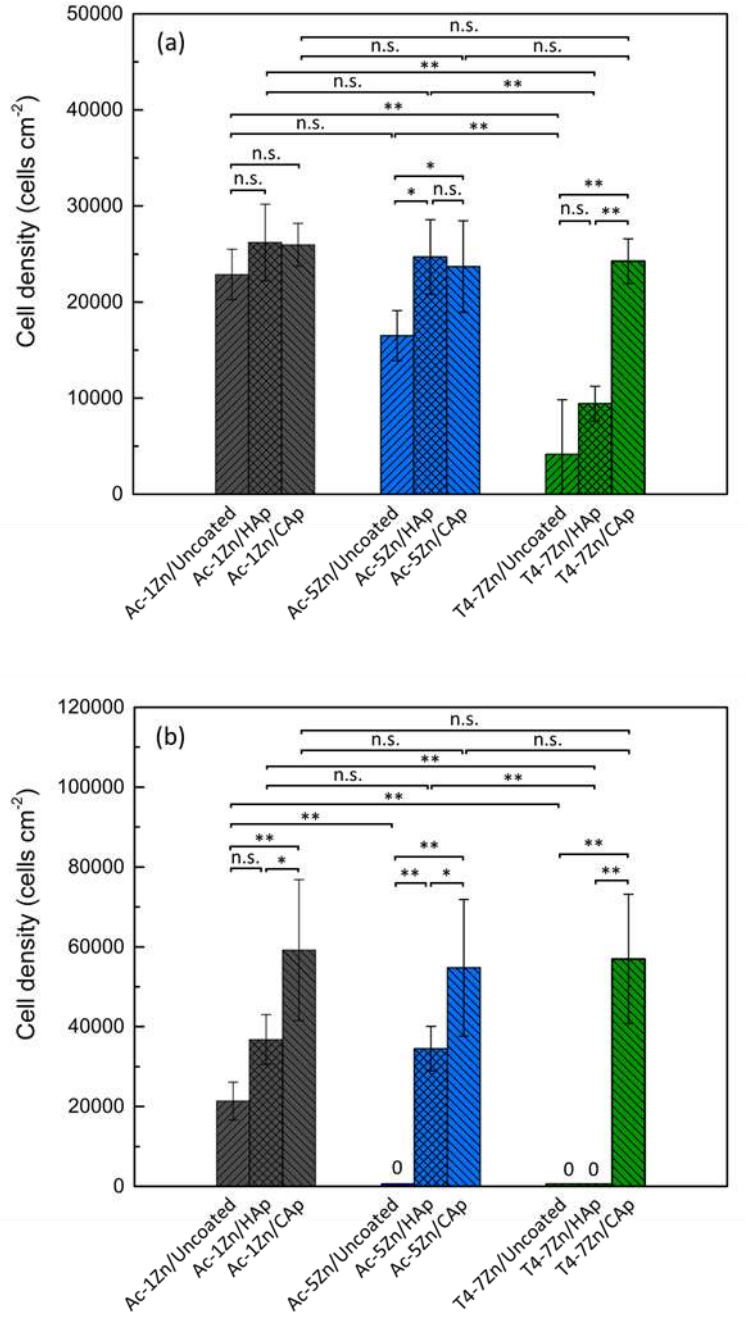

Figure 5.10 Cell density on uncoated, HAp-coated and CAp-coated Mg-1Zn and Mg-7Zn alloys after (a) 24 h and (b) 72 h of culture. n.s.: not significant, *: $p < 0.05$ and **: $p < 0.01$

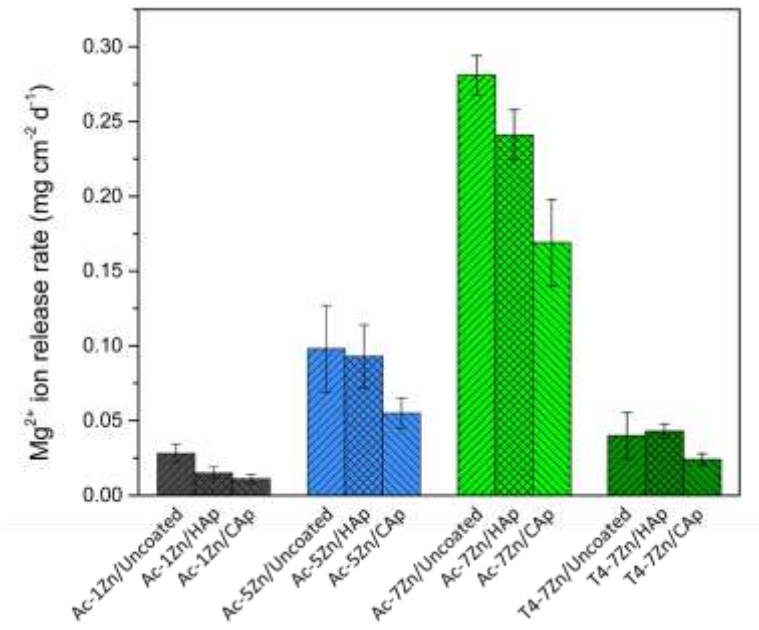

Figure 5.11 Average Mg^{2+} ion release rate of uncoated, HAp-coated and CAp-coated Mg-Zn alloys in Hanks' solution. Results of uncoated and HAp-coated Mg-Zn alloys are referred from previous studies [16,20]

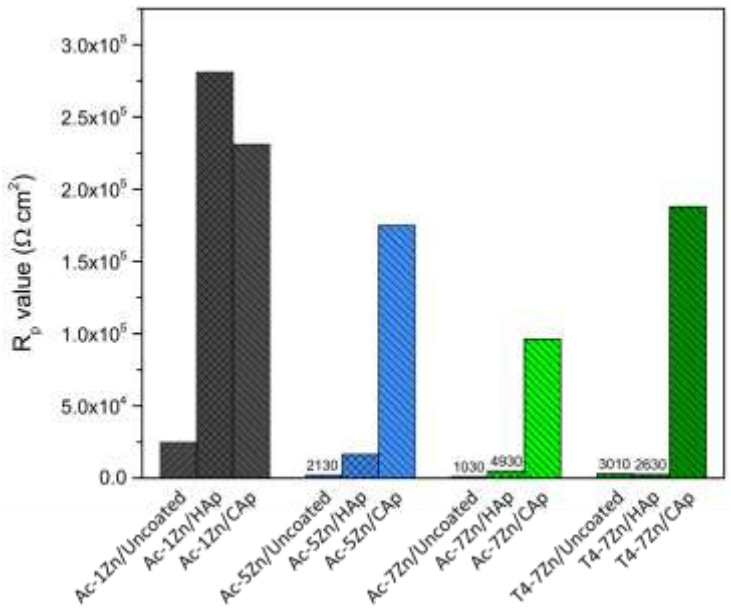

Figure 5.12 R_p values of uncoated, HAp-coated and CAp-coated Mg-Zn alloys. Results of uncoated and HAp-coated Mg-Zn alloys are referred from previous studies [16,20]

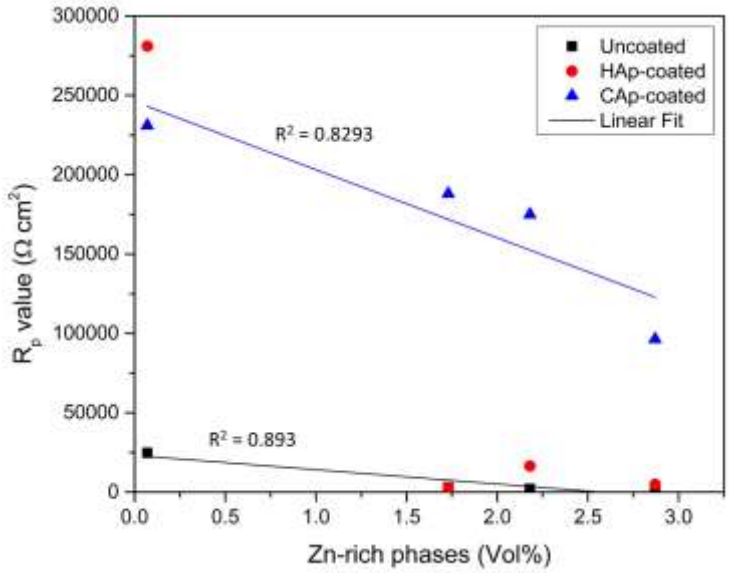

Figure 5.13 Relation of polarization resistance (R_p) of uncoated and HAp- and CAp-coated alloys with volume fraction of Zn-rich phases

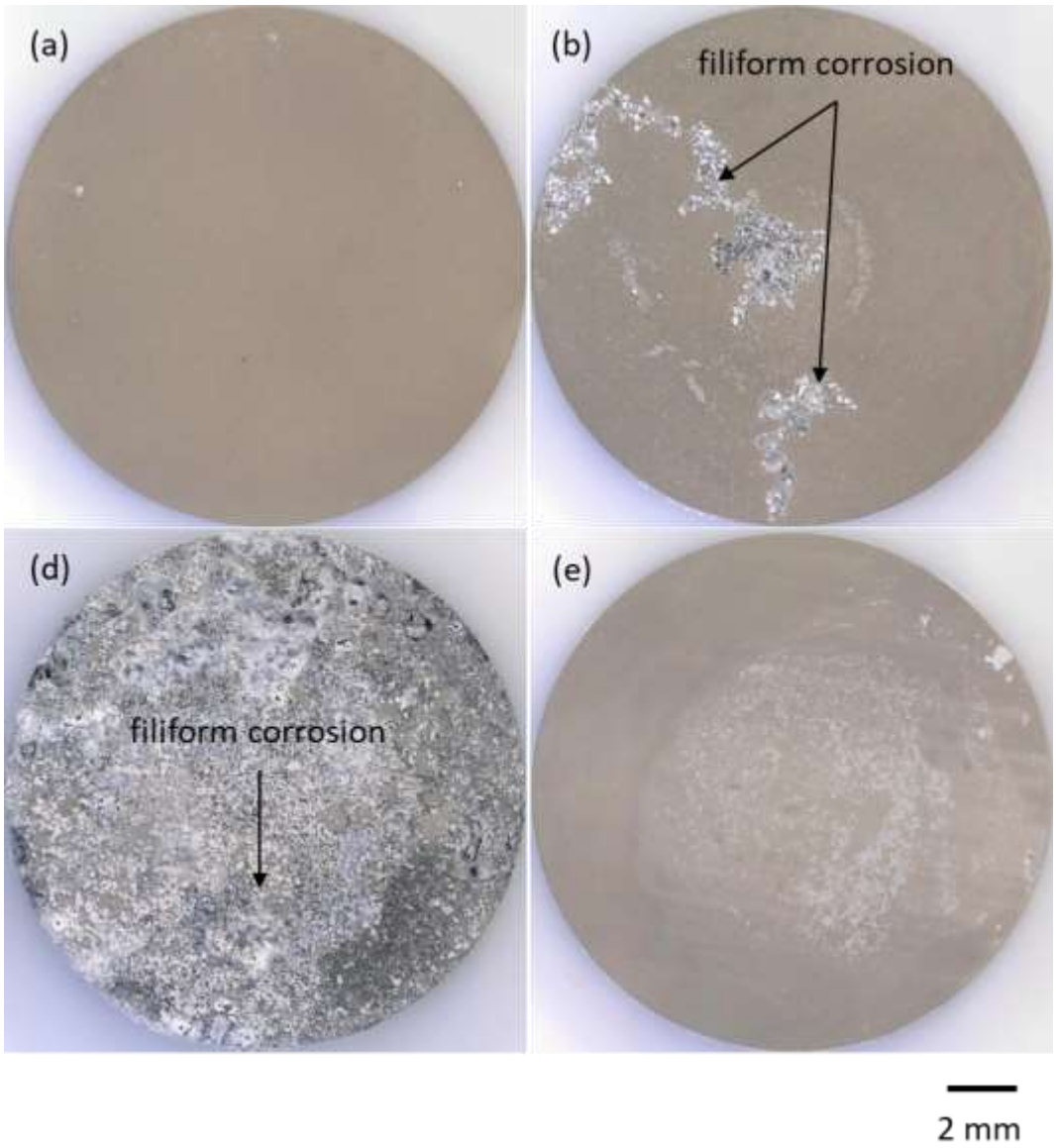

Figure 5.14 Optical surface images of (a) Ac-1Zn/CAp, (b) Ac-5Zn/CAp, (c) Ac-7Zn/CAp and (d) T4-7Zn/CAp after immersion in Hanks' solution for 14 days

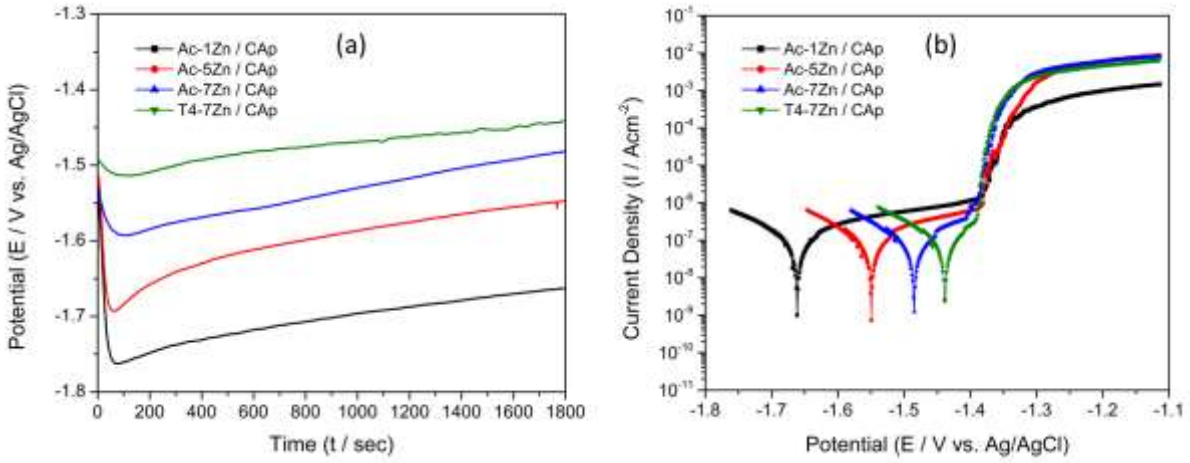

Figure 5.15 (a) Open circuit potential (OCP) and (b) potentiodynamic polarization curves of CAp-coated Mg-Zn alloys. All measurements were conducted in Hanks' solution at 37 ^{o}C

Chapter 6

General conclusions

This Ph.D. thesis focuses on developing magnesium-zinc (Mg-Zn) binary alloys for biodegradable orthopedic implant applications through microstructure control and surface coatings. The outlines of each chapter of the present thesis are briefly summarized as follows.

In chapter 1: The background of metallic biomaterials, current development and remained problems of Mg alloys for biodegradable orthopedic implants are introduced. The goals, purposes and methodology of the thesis are also established in this chapter.

In chapter 2: The influences of Zn content and solution heat treatment (T4 treatment) on the corrosion behavior of Mg-xZn alloys (x=1, 3, 5 and 7 wt%) are investigated. Results of the corrosion tests reveal that the volume fraction of Zn-rich phases influences the corrosion behavior of Mg-Zn alloys more dominantly than the Zn concentration. The Zn-rich phases including (α-Mg + MgZn) eutectic cell and Zn-segregated phase are formed along the grain boundaries in the as-cast Mg-Zn alloys and almost disappears by T4 heat treatment. As a result, the corrosion resistance of the T4-treated Mg-Zn alloys become higher than that of the as-cast Mg-Zn alloys with the same Zn content. In addition, it is found that the deposition of calcium phosphate from Hanks' solution contributes to improve the corrosion resistance of Mg-Zn alloys. Although the corrosion behavior of Mg-Zn binary alloys has been investigated in some previous studies, the optimal Zn content for corrosion resistance still remains in disagreement. Thus, these findings contribute to a deeper understanding of the corrosion factors of Mg-Zn binary alloys and are expected to resolve the current controversy.

In chapter 3: The influences of Zn content and solution heat treatment (T4 treatment) on mechanical properties and mechanical integrity of Mg-Zn alloys in Hanks' solution are studied. The addition of Zn significantly refined the grain size of as-cast Mg-Zn alloys. With increasing Zn content, (α-Mg + MgZn) eutectic cell and Zn-segregated phase precipitated at the grain

boundaries and dendrite arms, forming a network-like structure. The volume fraction of (α-Mg + MgZn) eutectic cell and Zn-segregated phase increased with increasing Zn content. The grain size of the Mg-Zn alloys increased after T4 treatment due to the dissolution of network-like structure of Zn-rich phases into Mg matrix. The hardness and strength of as-cast Mg-Zn alloys increase with increasing Zn content while the strain at failure decreases as Zn content increase. The T4 treatment reduces the strength and strain at failure, but increase the hardness of the Mg-Zn alloys. The mechanical properties of Mg-Zn alloys decrease with extension of immersion time in Hanks' solution. The deterioration of mechanical properties shows a dependence on the corrosion form of Mg-Zn alloys which is dominated by the microstructure of the alloys. Ultimately, the as-cast and T4-treated Mg-1Zn alloys show the highest mechanical properties retention after 28 days immersion test in Hanks' solution and are expected to provide high mechanical support in the next more 8-12 weeks.

In chapter 4: The hydroxyapatite (HAp) coatings are formed using a simple and cost-effective chemical solution deposition method. The influences of substrate microstructure on uniformity of HAp coating formed on Mg-Zn alloys and the corrosion behavior of the HAp-coated alloys are examined. The microstructure observations reveal that the particle size and volume fraction of Zn-rich phases significantly influences the uniformity of HAp coatings formed on Mg-Zn alloys by a chemical solution deposition method. The severe micro-galvanic corrosion between Zn-rich phases and α-Mg causes cracks in the HAp coating. As a result, the finer particle size and lower volume fraction of Zn-rich phases enhances the uniformity of coating. It is found that the initial corrosion resistance of HAp-coated Mg-Zn alloys is governed by the uniformity of HAp coating, and once the HAp coating irreversibly broken, it is dominated by the corrosion resistance of the substrate alloys. Although the structure and corrosion behavior of HAp coatings has been investigated on a number of Mg substrates including pure Mg, AZ31 and WE43 alloys, these substrates either contains no second phases, or the volume fraction and particle size of second phase are negligible. Thus, this study elucidates the effect of the substrate microstructure on the morphology and corrosion protectiveness of HAp coating. Moreover, it is suggested that the HAp-coated Mg-Zn alloys with low volume fraction of Zn-rich phases are promising candidates for biodegradable implant materials.

In chapter 5: The B-type carbonate apatite (CAp) coatings are developed by modifying the previously developed HAp coating solution in Chapter 4. The CAp coatings are formed on the Mg-Zn alloys to improve the corrosion resistance and *in vitro* biocompatibility. The microstructure and the corrosion protectiveness of the CAp coatings are compared to those of

the HAp coatings. Microstructure observation indicates that the CAp coatings grow uniformly on the Mg-Zn substrate alloys containing Zn-rich second phase with various particle sizes while the HAp coatings show defects on the large size second phase. Corrosion tests results demonstrates that the CAp coatings not only effectively retard the initial corrosion of Mg-Zn alloys in Hanks' solution, but also remains corrosion protectiveness even after the CAp coatings are partly broken. The corrosion protectiveness of the CAp coating is generally higher than that of the HAp coatings. The osteoblast viability on the Mg-Zn alloys is improved by the CAp coatings more effectively than the HAp coatings, which is attributed mainly to the higher corrosion protectiveness. It is demonstrated that owing to the defect-free uniform structure, the CAp coatings improve the corrosion resistance and biocompatibility of Mg-Zn alloys more effectively than the HAp coatings. Ultimately, the B-type CAp coating uniformly formed on the Mg-Zn alloys in this study is a promising corrosion-control coating which will promote the practical use of the alloys.

In chapter 6: The general conclusions obtained in each chapter are summarized.

Acknowledgement

This thesis is successfully completed with great support and inspiration from many people.

First of all, I would like to express my sincerest gratitude to my supervisor Associate Professor Equo Kobayashi for his countless dedicated support, great advice, and guidance throughout my studies at the Tokyo Institute of Technology since I was a one-year YSEP exchange student. His insightful advice and encouraged suggestions always give me answers and bring new ideas to my scientific research. Besides, he is always ready to help and share with me sincere advice and difficulties in life. During my 6 years as his student, I have learned and grown up a lot. For me personally, Equo-sensei is more than an academic supervisor.

I would like to thank the members of my thesis committee, Professor Masato Sone, Professor Eiji Tada, Professor Ji Shi, and Associate Professor Toshiyuki Ikoma. Their valuable advice and suggestions helped me to complete this thesis with the highest quality.

I would like to express my sincere thanks to Doctor Sachiko Hiromoto for kindly accepting me as visiting researcher in her laboratory at National Institute for Materials Science. I have learned a lot of knowledge and profession from her guidance and advice through the experimental work and publishing papers. I also acknowledge her kind and thoughtful help with my job application.

I am also grateful to all the members of Equo Kobayashi Laboratory for their kindness and help. I hope our friendship will last forever.

Finally, I would like to express my deepest gratitude to my beloved family. To my parents and parents-in-law, my brother and sister for their unconditional and limitless love, support, and listening. To my soulmate and my wife – Hai Thanh “Mít chèo”, who has always been my side and with me through everything, I would like to share all my achievements with you.